STAR FORMATION IN THE GALACTIC CONTEXT

STAR FORMATION IN THE GALACTIC CONTEXT:

A QUANTITATIVE STUDY

By

Samantha Marie Benincasa, B.Sc., M.Sc.

A Thesis

Submitted to the School of Graduate Studies

in Partial Fulfillment of the Requirements

for the Degree of

Doctor of Philosophy

McMaster University

DOCTOR OF PHILOSOPHY (2018) McMaster University
(Physics and Astronomy) Hamilton, Ontario

TITLE: Star formation in the galactic context: a quantitative study

AUTHOR: Samantha Marie Benincasa, B.Sc., M.Sc. (McMaster University)

SUPERVISORS: Dr. James Wadsley and Dr. Hugh Couchman

NUMBER OF PAGES: xvii, 191

Abstract

The processes that impact star formation operate not only on molecular cloud scales, but on the scales of full galaxies. This implies that the full galactic environment is crucial to the study of star formation. As observations and empirical relations on this scale become increasingly more detailed, simulations lag behind, still unable to explain the origins behind the Kennicutt-Schmidt relation, for example. We investigate star formation in the full galactic context through a series of isolated galaxy simulations. We favour purposefully controlled setups so that we can perform a systematic study of the drivers of star formation and the theoretical underpinning behind the formation of bound structures that lead to star formation.

We demonstrate the key role of pressure in regulating the star formation rate. We extend this to galaxies that include far-ultraviolet (FUV) heating implemented using radiative transfer. These simulations, the first of their kind, show that FUV heating is not sufficient to regulate star formation. Generally, we find that the scale height is a key driver in maintaining vertical hydrostatic balance. Simulated galaxies that do not resolve the scale height will be unable to explain fundamental relationships, becoming increasingly similar to semi-analytic models where all important relationships are imposed.

We develop a new method to study the formation of bound structure: we seed turbulent perturbations of known wavelength and velocity in quiet galaxy disks. The linear theory is a good approximation for the early phases of structure growth, which has a finite window to occur; the shear timescale. We find that clumps can form not just through central condensation but through rotation-driven fission and the fragmentation of tidal tails, a novel result. We find that these bound clouds, the direct progenitors of star clusters, do not exceed $\sim 10^9$ $M_\odot$ in galaxies of gas mass up to $\sim 5 \times 10^{10}$ $M_\odot$.

For Mom and Dad

Co-Authorship

Chapters 2, 3 and 4 of this thesis contain original scientific research written by myself, Samantha Marie Benincasa. Chapter 2 has been published as a peer-reviewed journal article in the Monthly notices of the Royal Astronomical Society (MNRAS). The reference to this work is:
Benincasa, S. M., Wadsley, J, Couchman, H. M. P. & Keller, B. W., 2016, MNRAS, Volume 462, Issue 3, pp. 3053-3068
My co-supervisors, Dr. James Wadsley and Dr. Hugh Couchman, are the second and third authors. Dr. James Wadsley developed the mathematical model presented in the Appendix. Dr. Ben Keller is the fourth author and he implemented the feedback used in the study.

At the time of submission, the work presented in Chapter 3 has been submitted for publication in MNRAS. The author list is as follows:
Benincasa, S. M., Wadsley, J, Couchman, H. M. P., Pettitt, A. R. & Tasker, E. J.
My co-supervisors, Dr. James Wadsley and Dr. Hugh Couchman, are the second and third authors. Dr. Alex Pettit and Dr. Elizabeth Tasker participated in the development of the study. Dr. James Wadsley developed the initial conditions and perturbation spectrum for the simulations.

The research presented in Chapter 4 is in preparation to be submitted to MNRAS. The author list is as follows:
Benincasa, S. M., Wadsley, J, Couchman, H. M. P., Pettitt, A. R., Grond, J., Keller, B. W. & Woods, R. M. My co-supervisors, Dr. James Wadsley and Dr. Hugh Couchman, are the second and third authors. Dr. James Wadsley ran the simulations. Dr. Alex Pettit ran calibration tests for the study. Jasper Grond and Dr. Rory Woods implemented the radiative transfer used in the study. Dr. Ben Keller implemented the superbubble feedback used in the study.

All previously published material has been reformatted to conform to the required thesis style. I grant an irrevocable, non-exclusive license to McMaster University and the National Library of Canada to reproduce this material as part of this thesis.

Acknowledgements

Firstly, I would like to thank my supervisors, Dr. James Wadsley and Dr. Hugh Couchman. For being a constant source of guidance, support and encouragement. For having a seemingly never-ending reserve of patience. For telling me you knew that I could when I thought that I couldn't.

Thank you to Dr. Elizabeth Tasker for being a sounding board, a role model and a friend. You always supported me, without question, and that has made all the difference in the world.

Over the past 6 years I have spent the most time with my officemates, past, present and honourary, and they deserve so many thanks. For listening to me to me, tolerating our office being turned into a GWIPA storage space and stopping me from banging my head against the wall. For so many breakfasts that the staff at Pancake House have named us using our orders (eggs & bacon over-easy, rye toast). A particular shoutout to Ben Keller, Corey Howard and Matt Alessi, for repeatedly talking me down off the ledge. And to Matt for pointing out how much I sigh, I had no idea!

Thank you to Rory Woods. For checking in on my and for knowing exactly when I needed you to appear to go for a beer, unprovoked. I will actually come over for a baking day; December, be there!

Thank you to the McMaster LunchTable (Rachel Ward, Aaron-Maxwell, Tara Parkin, Kaz Sliwa, Max Schrim, Mikhail Klassen and Angus Mok) for lighting up my phone every Tuesday, then Monday, then Tuesday again. You have all been a constant source of support, advice and friendship. Thank you especially to Rachel and Tara, for baking afternoons, secret brunches, and for just understanding. And Rachel, thank you for so much glitter!

Thank you to Dr. Alex Pettit. For providing pointed wisdom countless times, in real time, working with a 12 hour time difference.

Thank you to Gwen Eadie-Springford and Gandhali Joshi, who are always ready with support and encouragement. Thank you also to GWIPA (especially Sara, Tara and Carmen), for distracting me with craft nights and so many cookies.

Thank you to Tina, Rose, Mara, Cheryl and Hope. You are all so amazing! I'm going to miss wandering into the office to talk to you all.

Lastly, thank you to my family for always being there for me, no matter what. A big, big thank you to my sister Kathryn, for supporting me, always, and making me buttons!

“For if we are uncritical we shall always find what we want...”

The Poverty of Historicism

KARL POPPER (1902-1994)

Table of Contents

List of Figures

List of Tables

List of Acronyms

ALMA	Atacama Large Millimeter Array
CANDELS	Cosmic Assembly Near-infrared Deep Extragalactic Legacy Survey
CDM	Cold Dark Matter
CMB	Cosmic Microwave Background
FUV	Far Ultra-Violet
GALEX	Galaxy Evolution Explorer
IC	Initial Condition
GMC	Giant Molecular Cloud
ISM	Interstellar Medium
ISRF	Interstellar Radiation Field
KS	Kennicutt-Schmidt
PAWS	PdBI Arcsecond Whirlpool Survey
PHANGS	Physics at High Angular Resolution in Nearby Galaxies
SFR	Star Formation Rate
SHMR	Stellar-to-Halo Mass Relation
THINGS	The HI Nearby Galaxies Survey
VDI	Violent Disk Instability

Chapter 1

Introduction

The focus of this thesis is galaxies as well as the stars and gas within them. At this time, we understand the detailed information about the initial conditions in the Universe that are imprinted in the Cosmic Microwave Background (CMB). However, our ability to take those initial conditions and evolve them into present-day galaxy analogues is, at this time, quite limited. Although this evolution involves physics that we understand in principle, the final products, spiral galaxies, are not simple to predict. Thus, in some respects, it is better motivated to start with the known properties of galaxies, particularly if the goal is to understand the physical processes that operate in galaxies today. In this thesis, we do not take this ab initio approach and instead focus on the processes within galaxies themselves. Even though it is not our focus, it is important to begin by establishing the context in which these galaxies formed.

1.1 Galaxy formation in the cosmological context

Of all that constitutes the Universe, only 31% is actual matter. Luminous, or baryonic matter, the type that we can study most easily with telescopes, constitutes only 5% of the Universe (Planck Collaboration, 2015). The currently accepted best cosmological model is cold dark matter with a cosmological constant (Λ CDM, Blumenthal et al., 1984).

CDM is the currently accepted model because it provides the best fits to our observational inferences about the Universe. CDM is successful at explaining both the cosmic microwave background and the large-scale structure of the cosmos. However, it is not without its failings. These problems largely manifest themselves in the complex non-linear stages of object formation which are commonly studied with numerical simulations. One well-known short-coming is dubbed the missing satellite problem: there are more dark matter satellites predicted in numerical simulations than we observe for local group galaxies (Klypin et al., 1999; Moore et al., 1999). Recent work has suggested this problem may be a product of missing baryon physics in these earlier simulations (Brooks & Zolotov, 2014; Garrison-Kimmel et al., 2018). A newer challenge for CDM is the planar distribution of satellite galaxies: the planes of satellite galaxies problem (Müller et al., 2018). As a result, we cannot fully rule out other models for dark matter, such as warm or self-interacting dark matter.

In the very early universe, the distribution of matter was close to homogeneous. There were minute departures from this homogeneity in the form of quantum fluctuations. As a result of inflation, these microscopic fluctuations expanded to macroscopic scales (Guth, 1981; Linde, 1982). As time passed, these fluctuations grew. Once the time of recombination was reached, these fluctuations could finally be observed imprinted on the CMB.

The CMB holds so much important information about the structure in our Universe. Almost our entire cosmological model can be described by a handful of parameters and the well-tested assumption that the initial fluctuations are Gaussian random. These fluctuations imprint a spectrum and we measure them as temperature anisotropies on the CMB. These small fluctuations, only 1 part in 10^5, are the seeds of the formation of structure as we see it today.

Structure forms in regions that are overdense compared to the background, and voids form in regions that are underdense. A quantity of importance when considering the growth of these fluctuations is the overdensity, $\delta(x)$, which describes the deviation of a region from the average density,

$$\delta(x) = \frac{\rho_m(x) - \bar{\rho}_m(x)}{\bar{\rho}_m(x)}, \tag{1.1}$$

where $\rho_m(x)$ is the density, and $\bar{\rho}_m(x)$ is the average density. While $|\delta(x)| \ll 1$, these perturbations can be treated as linear and their behaviour can be predicted analytically.

The Universe is in a constant phase of expansion. As these fluctuations develop they are trapped in the large-scale Hubble flow. They participate in expansion and this prevents them from fully collapsing under their own self-gravity. As these overdensities approach $\delta(x) \sim 1$, they are able to detach from the Hubble flow. At this point their evolution becomes more complex, and can no longer be modelled simply analytically. This is where more complex theories or N-body simulations can be of assistance.

The distribution of progenitor halos can be well described by combining the spectrum of initial fluctuations and the predictions of CDM. Given the initial spectrum, which we can discern from the CMB, it is possible to predict the fraction of mass contained in bound objects of a given mass (Press & Schechter, 1974). Halos accrete baryons from the larger cosmic web. These baryons fall into the deep potential wells created by the first dark matter halos. As gas falls in it is shock heated to the virial temperature of the halo. The temperature and density of the gas decide the fate of the halo. In order to form the first galaxies, gas must be able to condense to higher densities than the overall background halo.

Whereas dark matter is collisionless, baryons are not and they can radiatively cool. In order to determine if gas can condense efficiently once it has virialized, there are two timescales of interest to be compared: the dynamical time, $t_{\rm dyn}$, and the cooling time, t_Λ. The dynamical time describes how long it would take gas to collapse under its own self-gravity. The cooling time describes how long it would take gas to radiate its energy away.

By considering these two timescales, we can estimate an upper limit for the mass of a protogalaxy (Rees & Ostriker, 1977). If $t_\Lambda > t_{\rm dyn}$, the gas cannot cool efficiently and no further collapse will occur: the gas will remain virialized in the halo. Only when $t_\Lambda < t_{\rm dyn}$, can the gas cool efficiently and condense. At the time of the formation of the first galaxies, this leads to possible masses between 10^5-10^{10} $M_\odot$. CDM requires that structure formation is hierarchical: the smallest scales will become unstable and collapse first, such that the typical masses of protogalaxies are actually between 10^5-10^6 $M_\odot$. These smaller structures will, over time, build up larger and larger structures via merging.

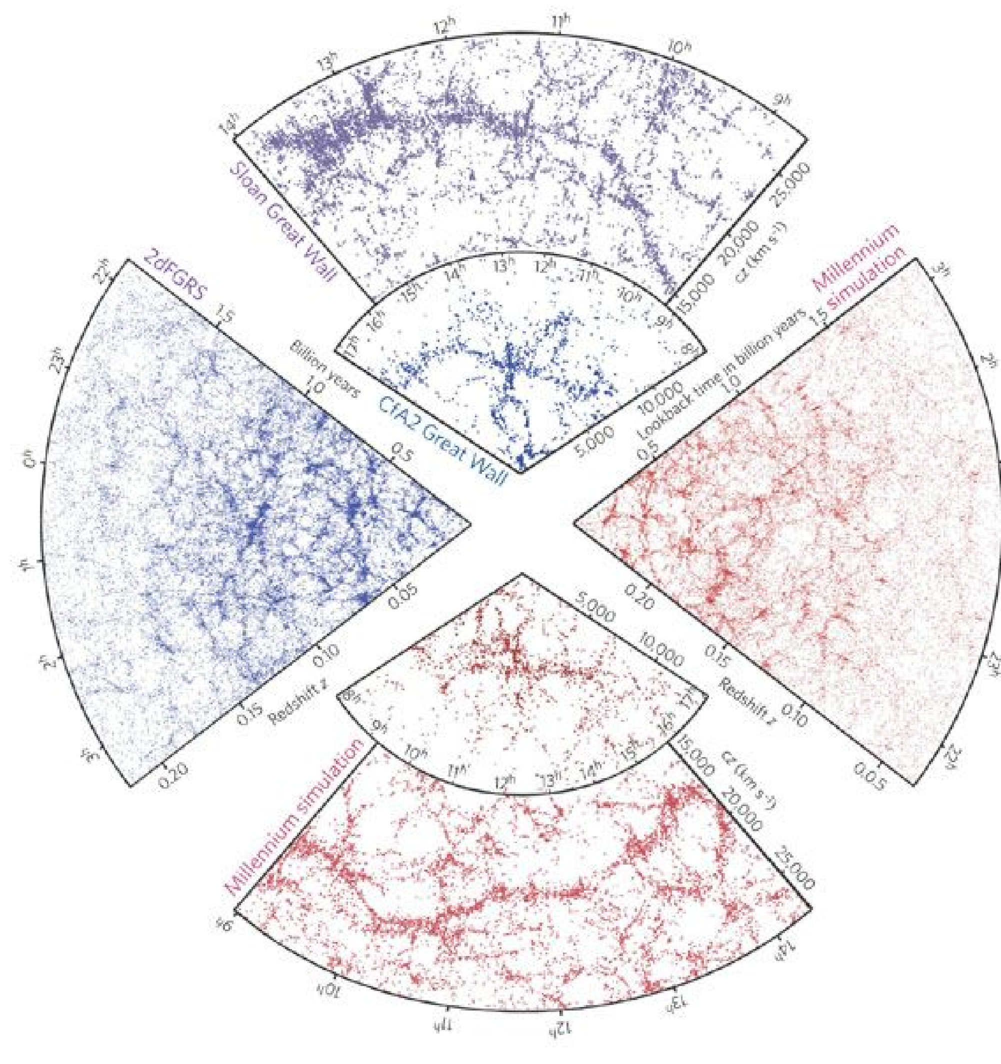

Figure 1.1: Comparison of observed and simulated galaxy distributions
A sample of the observed galaxy distribution in the spectroscopic surveys SDSS and CfA2 (bue), compared to the galaxy distribution in the Millennium simulation (red). The simulated galaxy distribution is produced using semi-analytic modelling to go from the dark matter only distribution of Millennium, to the mock catalogue shown.
Image Credit: Springel et al. (2006), © SpringerNature, reproduced with permission.

1.1.1 Studying the structure of dark matter and baryons in numerical simulations

The processes that take us from the first dark matter halos to the galaxies of today are numerous. Numerical simulations provide a viable avenue to study the formation of structure, as it becomes more non-linear and more complex. However, simulating the Universe on a computer comes with many challenges.

To start with, the initial spectrum of density fluctuations must be set to create the initial conditions. There are dependences on resolution or the size of the chosen volume that must be considered. Resolution can be particularly problematic, as this problem spans both size- and time-scales that vary by orders of magnitude. A common approach is to start first with only dark matter. N-body simulations are inexpensive when compared to those that also include baryons. Large volumes can be simulated first with dark matter and then regions of interest can be re-simulated with baryons at higher resolution in “zoom-in” simulations.

Dark matter only simulations are useful in and of themselves. They provide us with a way to test cosmological models and to study the detailed structure of dark matter, which can be difficult observationally. Many important implications of CDM have been gleaned from N-body work. For instance, halos share a near-universal density distribution, the most popular descrtiption of which is the NFW profile (Navarro et al., 1996). At this point we understand well the way that dark matter assembles itself into structure.

Figure 1.1 shows results from the Millennium simulations (DM only) combined with semi-analytic modelling to predict galaxy properties; shown in red on the right and bottom (Springel et al., 2006). These results are compared to the actual observed distributions of galaxies; shown in blue on the left and top. The top-most image shows a portion of the Sloan Digital Sky Survey (York et al., 2000), while the slice beneath it shows the Great Wall surrounding the Coma cluster as identified in the Centre for Astrophysics galaxy redshift survey (Geller et. al, 1989). The lefthand image shows galaxies in the 2 degree field galaxy redshift survey (Colless et al., 2001). The simulated and observed distributions bear a striking resemblance.

This figure demonstrates that, just as excellent progress was made studying the structure of dark matter in simulations, we are starting to make progress in understanding how baryons are distributed in dark matter halos. Semi-analytic models are useful for translating dark matter only structure to galactic properties. However, these models are often highly tuneable: our empirical knowledge of galaxies is, at this time, better than our ability to simulate ab initio.

The assembly of baryons into galaxies is also studied in numerical simulations. Due to the resolution available in these cases, subgrid methods must be developed to represent star formation and energetic feedback processes. The added costs of these gas physics makes these types of simulations more computationally expensive than their dark matter only counterparts. While it is possible to simulate a full cosmological volume with both dark matter and baryon physics, a more common approach is the zoom-in, as discussed previously.

As mentioned previously, baryons fall into the potential wells created by these dark matter halos by condensing and cooling (Fall & Efstathiou, 1980). This implies that there should be correlations between star formation or stellar content and the corresponding dark matter halo properties. It is not trivial to explore these relations, as the luminous and dark properties of galaxies must be linked together. The relation in question is the stellar-to-halo mass relation (SMHR) and it constrains the efficiency of star formation in dark matter halos of different masses. Recently, these connections have been studied using abundance matching techniques.

These types of techniques effectively assume that the galaxies with the highest stellar masses live in the most massive dark matter halos (Conroy & Wechsler, 2009; Behroozi et al., 2010; Moster et al., 2013). A more accurate technique involves the use of weak lensing measurements to constrain this relation. Using the CFHTlens survey, Hudson et al. (2015) have constrained the SHMR up to redshift $2 \sim 3$.

There is a large body of numerical work that focuses on the cosmological context of galaxy formation. Large box simulations study the formation of structure, the development of the star formation rate and star formation efficiency. These types of simulations often use the SHMR and the cosmic star formation history as benchmarks. That is to say, the regulation of star formation is of high interest. The SMHR shows that the efficiency of star formation peaks for dark matter halos of mass $\sim 10^{12}$ $M_{\odot}$, and quickly decreases at both higher and lower masses. We know that this physics is controlled by supernovae for small halo masses and likely AGN at high halo masses (Keller et al., 2016, and references therein).

1.1.2 The characteristics of galaxies at high redshift

Galaxies can be roughly categorized into two different types; spiral and elliptical. Elliptical galaxies have consumed a large portion of their star-forming fuel and thus have low star formation rates. Further, they are triaxial and mainly supported by the random motions of their stars. Spiral galaxies are the focus of this thesis. These galaxies are actively forming stars and have flattened disks that are supported by rotation.

Our home is in the Milky Way galaxy, a spiral galaxy at redshift 0. A galaxy is composed of a collection of dark matter, stars and gas which in the Milky Way are 8.7×10^{11} $M_{\odot}$ (Eadie et al., 2017), 5×10^{10} $M_{\odot}$ (McMillan, 2011) and 5×10^{9}

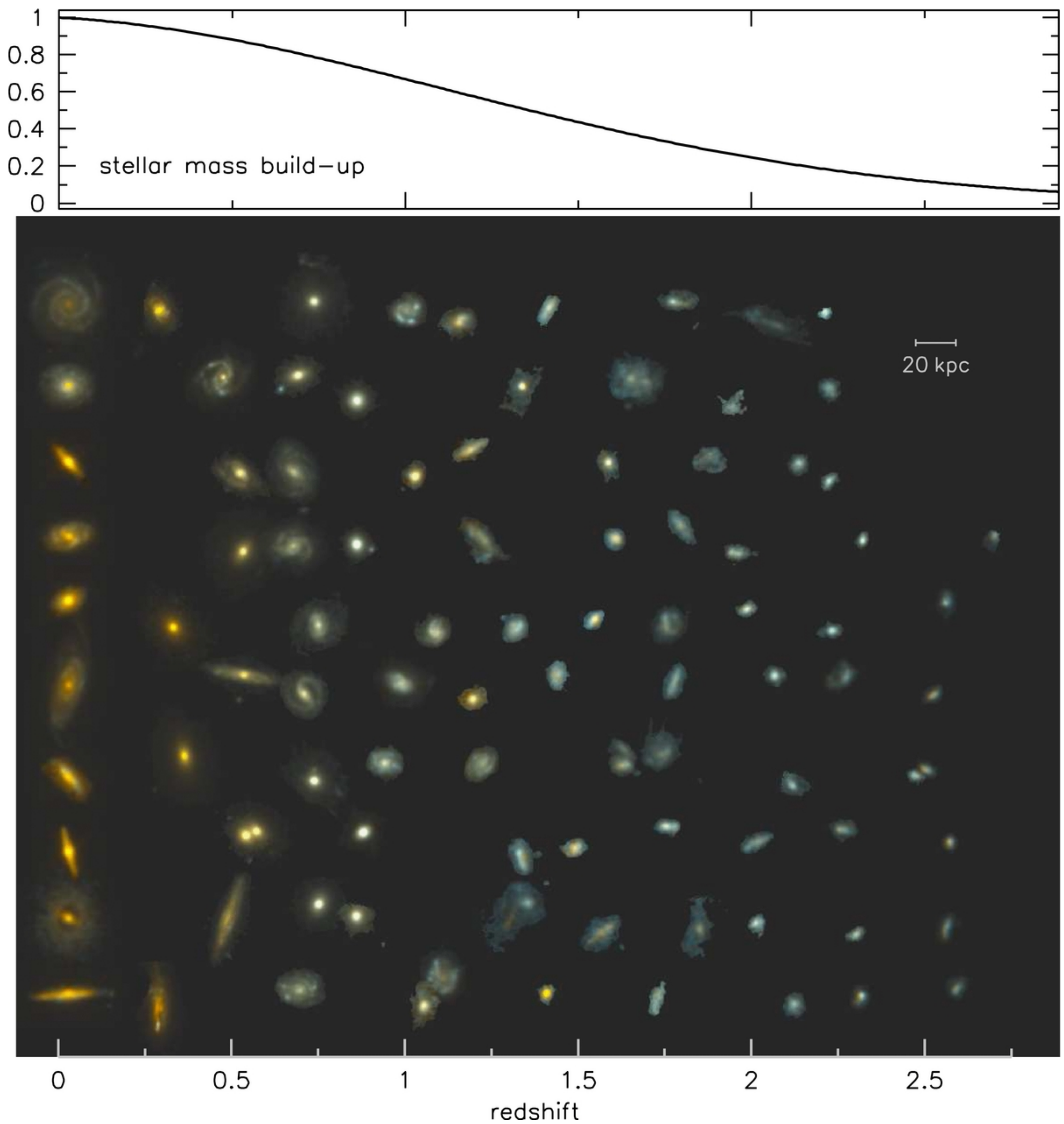

Figure 1.2: Galaxies similar to the Milky Way throughout cosmic time
A subset of identified Milky Way progenitors in the GOODS and CANDELS surveys. Galaxies that have the present-day mass of the Milky Way have changed over the history of the Universe. The upper panel illustrates the rate at which the Milky Way built its stellar mass over cosmic time.
Image Credit: van Dokkum et al. (2013) © AAS, reproduced with permission.

$M_\odot$ (cold gas, Mo, van den Bosch & White, 2010). In this case the dynamics of the galaxy are largely dominated by the stellar disk, which is an order of magnitude more massive than the gaseous component. Sites of new star formation are largely adjacent to the spiral arms. These stars are forming at a rate of 1 - 2 $M_\odot$/yr (e.g. Chomiuk et al., 2011; Licquia et al., 2015). However, the Milky Way has undergone a long past of evolution to get to this point.

If we look to the earlier Universe, galaxies look and behave much differently and Figure 1.2 illustrates this point. Galaxies with masses comparable to the Milky Way account for a large fraction of the stellar mass density of the Universe: after $z \sim 6$ it is these galaxies that dominate star formation (Behroozi et al., 2013). However, galaxies of similar mass to the Milky Way at previous epochs will be found as elliptical galaxies in the Universe now. Using cosmological models, we can estimate the mass of the Milky Way at different epochs in the evolution of the universe. Figure 1.2 shows galaxies similar to the Milky Way at different redshifts, chosen by matching to this mass. In this figure, high redshift galaxies have been identified in the 3D-HST (Giavalisco et. al, 2004) and CANDELS (Grogin et. al, 2011) surveys, while low redshift galaxies are from SDSS. There is significant evolution in the characteristics of these galaxies over time. As we move from higher to lower redshift, the galaxies grow larger and appear more disky. Over this time their bulges evolve and we see that at high redshift, galaxies either have no bulge or a very weak bulge. As we move to redshift zero galaxies also appear redder, there is less active star formation.

1.2 Star formation in galaxies now

At the present time, the distribution of dark matter through the Universe is well understood. However, baryons play a crucial role in the buildup of galaxy properties. Baryons, specifically their resolved properties in the ISM, are not completely understood on the galactic scale. Many simulations explore the regulation of star formation on the cosmological scale; at this scale the full nature of the ISM cannot be fully captured at the currently available resolutions. As a field, we have answered so many questions about dark matter and structure formation. There are equally as many questions unanswered about the role and nature of the ISM and star formation in the full galactic context. This single, resolved galaxy scale is the scale of interest in this work.

1.2.1 A brief primer on star formation

Stars form in large collections of molecular gas and dust called giant molecular clouds (GMCs). GMCs have typical masses between 10^4 and 10^6 $M_\odot$, and typical sizes between 50 and 100 pc. These complexes are the exclusive sites of star formation in normal spiral galaxies like our Milky Way (McKee & Ostriker, 2007). They can be found in large concentrations near spiral arms, but are distributed throughout the galactic disk. However it should be noted that clouds in different galactic environments have been shown to have different properties. For example, there is a contrast between the properties of arm, inter-arm and central clouds (Colombo et al., 2014). GMCs have typical average densities of 100 cm^{-3}. As star formation proceeds, these complexes futher fragment and collapse into dense molecular clumps and star-forming cores. Star formation is thought to proceed in gas with surface densities above ~ 116 $M_\odot$/pc^2 ($A_K \sim 0.8$), which corresponds to a volume density of 10^4 cm^{-3} (Lada et al., 2010).

If we go up one spatial scale, we consider the distribution of gas through the entire galactic disk. The molecular gas fraction, $R_{\rm mol}$, is defined as the ratio of molecular to atomic gas, $M_{\rm H_2}/M_{\rm HI}$. In Milky Way-like galaxies, the typical molecular gas fraction is ~ 0.3 (Saintonge et al., 2011). The radial distribution of these two gases is not the same throughout the galactic disk. The molecular gas has an exponential distribution, with a scale length on the order of a quarter the optical radius (Schruba et al., 2011). In contrast, the atomic hydrogen has a roughly flat radial distribution across the star-forming disk (e.g. Bigiel et al. (2008) on galactic scales or Lee et al. (2012) on GMC scales).

1.2.2 The distribution of gas in galaxies

To further discuss the distributions of atomic and molecular gas we will use NGC 6946, the fireworks galaxy, as a case study. Figure 1.3 shows an example of different high resolution stellar and gas maps for NGC 6946. The distributions of atomic and molecular gas are shown in the bottom two panels of Figure 1.3. In this case, the distribution of molecular hydrogen is traced using CO emission as a proxy; the rotational transitions of molecular hydrogen require high temperatures to directly observe.

In the bottom right panel of Figure 1.3 the CO $J = 2 \rightarrow 1$ emission is shown: this traces molecular hydrogen gas.The location of molecular hydrogen is concentrated in the central region and the spiral arms. However, if we look to the atomic hydrogen, we see a different story. The atomic hydrogen is distributed over the entire galactic disk, and is only slightly more concentrated in the locations of the spiral arms. There is also no significant atomic hydrogen over-density in the

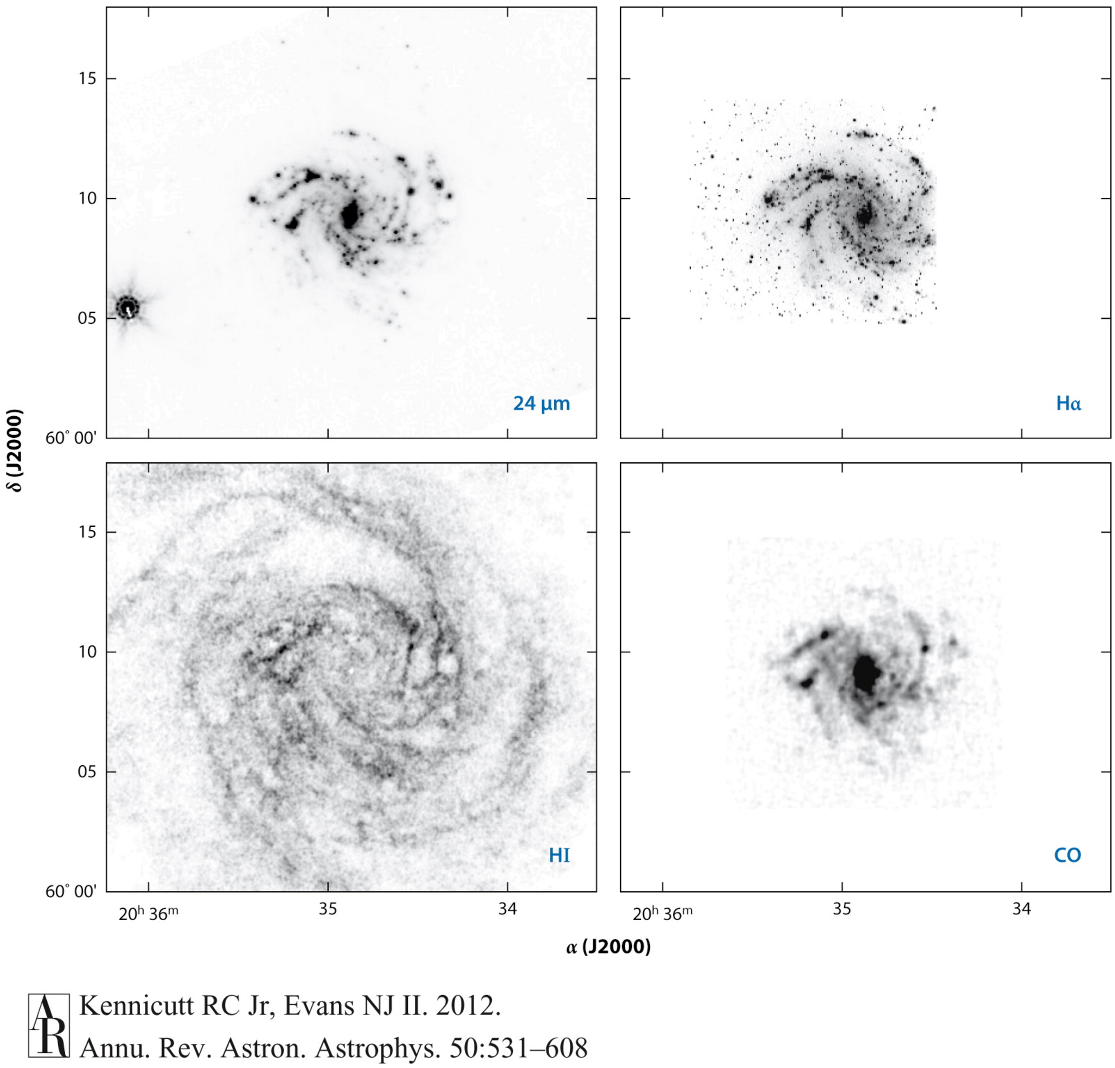

Figure 1.3: The distribution of star formation in galaxies
Star formation and gas maps for the galaxy NGC 6946, the fireworks galaxy. The upper left panel shows 24 μm emission, which traces star formation in the last 100 Myr. The upper right panel shows Hα, which traces star formation in the last 10 Myr. The bottom row shows the the distribution of atomic hydrogen (left) and molecular hydrogen as traced by CO (right).
Image Credit: Kennicutt & Evans (2012) © Annual Reviews Inc., reproduced with permission.

central region of the galaxy.

These distributions should connect in some way to the distribution of star formation in the galaxy. In the top left panel of Figure 1.3 the 24 μm dust emission is shown; 24 μm emission traces star formation that has occurred in the last 100 Myr (Rieke et al., 2009). In the top right panel, the Hα emission is shown; Hα emission traces young star formation that has occurred in the last 10 Myr (Hao et al., 2011; Murphy et al., 2011). Similarly to the molecular hydrogen distribution, the recent star formation is concentrated in two main locations, the central region of the galaxy and in the spiral arms. In this galaxy, the distribution of atomic hydrogen is much more extended than either the molecular gas or star formation. Whereas the molecular hydrogen component is centrally condensed and can have high surface density, that of HI does not exceed ~ 10 M$_{\odot}$/pc^2 (Bigiel et al., 2008). This is typical of normal spiral galaxies.

The most accessible galaxy to us is, of course, the Milky Way: the galaxy in which we live. However, observing a galaxy from within comes with its own challenges. Distances, for instance, are difficult to infer and certain regions remain obscured. Therefore, if we want to build a statistical sample of galaxy properties against which to test our theories of star formation, we must look outside the Milky Way.

1.2.3 Extragalactic observational studies

Studying the radial distributions of galaxy properties has been helped immensely by the advent of large multi-wavelength surveys. Surveys like the GALEX Nearby Galaxies Survey (Gil de Paz et al., 2007) or the Spitzer Infrared Nearby Galaxies Survey (Kennicutt et al., 2003) have shown us the properties of star formation in a range of different galaxies. Surveys for the same targets can then be undertaken in HI (e.g. THINGS, Walter et al., 2008) or CO (e.g. HERACLES, Leroy et al. (2009), NGLS Wilson et al. (2009)). It is these types of datasets that enable the comparisons made in Figure 1.3. These types of surveys are suited to studying the large-scale properties of the ISM and star formation in the galactic context (see e.g. Bigiel et al., 2008; Leroy et al., 2008).

An alternative to large surveys is choosing a single galaxy on which to focus observational efforts. In the local group, there have been recent studies focusing on M33, the triangulum galaxy, at high resolution; these have been used to constrain the life cycles of giant molecular clouds (Corbelli et al., 2017). Another recent target has been M51, the whirlpool galaxy. PAWS (Schinnerer et al., 2013) has given us a detailed look at the molecular gas structure of M51 at 60 pc spatial resolution. At this resolution, it is possible to access the detailed properties of GMCs and to explore the role of spiral arms in the cycle of star formation (e.g. Colombo et al., 2014b; Meidt et al., 2015; Schinnerer et al., 2017).

In the near future, large surveys like PHANGS (Leroy et al., in prep.), will give us an unprecedented look at star formation in 70 galaxies in the local volume. With gas and stellar resolution comparable to PAWS, we will get at look at not just resolved GMC properties but also the resolved properties of star formation (e.g. Sun et al., 2018).

1.2.4 Star formation relations

One of the most famous empirical laws used to characterize star formation in galaxies is the Kennicutt-Schmidt relation (Kennicutt, 1998). The KS relation links the star formation rate surface density, $\Sigma_{\rm SFR}$, to the total gas surface density, Σ_g,

$$\Sigma_{\rm SFR} = {\rm A}\ \Sigma_g^{1.4}, \tag{1.2}$$

where A is a constant relating to the star formation timescale. The concept of a power-law relation connecting star formation and gas density can be dated back to Schmidt (1959). This relation can be measured using many different techniques and at a variety of spatial scales. Figure 1.4 shows a compilation of measurements plotted in this plane (Kennicutt & Evans, 2012).

There are three main regions in the Kennicutt-Schmidt plot, denoted by the vertical gray dashed lines in Figure 1.4. Starburst galaxies populate the region where $\Sigma_g \gtrsim 200$ $M_\odot$/pc^2. In this regime star formation efficiencies are high, approaching 100%. At these surface densities, galaxies are H_2-dominated. Normal spiral galaxies can be found between $10 \lesssim \Sigma_g \lesssim 200$ $M_\odot$/pc^2. These galaxies do not form stars as efficiently, with star formation efficiencies approaching 10%. Both starburst and normal spiral galaxies appear to have the same power-law slope, although the starburst regime seems to be offset from the spiral regime.

At the lowest surface densities, $\Sigma_g \lesssim 10$ $M_\odot$/pc^2 are low surface brightness galaxies and the edges of normal spiral galaxies. In this region, measurements are HI-dominated. Here, there appears to be a break in the power law relation. At this point, there is almost no correlation between the two quantities and stars can form at any efficiency.

It may be that the total gas surface density is not the best parameter to quantify the star formation rate. If the molecular gas surface density, $\Sigma_{\rm H_2}$, is used instead there is no turnover at the transition from HI and H_2 dominated regions (at $\Sigma_g \sim 10$ $M_\odot$); the slope becomes linear and is consistent through this transition region (Schruba et al., 2011).

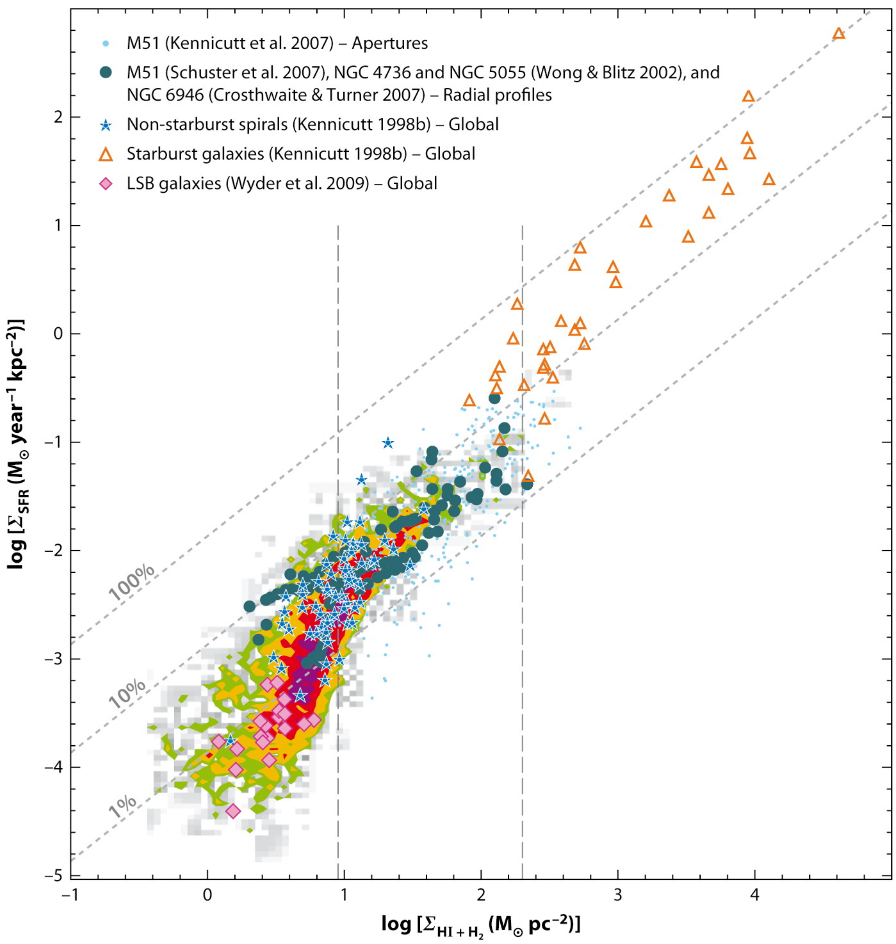

Kennicutt RC Jr, Evans NJ II. 2012.
Annu. Rev. Astron. Astrophys. 50:531–608

Figure 1.4: The Kennicutt-Schmidt Relation
The Kennicutt-Schmidt relation for nearby galaxies (Kennicutt & Evans, 2012). This figure combines three different methods of measurement. Diamonds, stars and triangles show measurements that have been averaged over the entire galactic disk. The large filled circles show measurements taken in annuli at different radii within a galaxy. The small light blue circles and the coloured contours show measurements that have been taken in single sub-kpc apertures in different galaxies. Finally, dashed lines shows lines of of constant efficiency, or depletion time.
Image Credit: Kennicutt & Evans (2012) © Annual Reviews Inc., reproduced with permission.

There are also three different measurement scales included in Figure 1.4. On the largest scale are global measurements, taken in apertures the size of an entire galaxy (diamonds, triangles and stars). In this case we can see a fairly tight correlation that has a non-linear power law index of ~ 1.4. Although, as mentioned above, there is a slight offset in the normalization of starburst galaxies when compared to normal spirals. The next scale of interest is labelled radial profiles in Figure 1.4. In this case points represent the average in annuli at different galactic radii; these types of measurements are plotted as the large filled circles. These measurements support the power law observed for the galactic average points, but scatter begins to emerge more prominently. Finally, at the smallest scale, are measurements taken in sub-kpc apertures. In Figure 1.4, these measurements as plotted as the small light blue circles. Data for multiple galaxies from Bigiel et al. (2008) taken in 750 pc apertures are also plotted as the coloured contours. At this scale, we can see significant scatter begins to emerge.

There is some debate as to whether this scatter is real and meaningful, or if it is a consequence of measurement techniques. It has been suggested that differences in SFR estimation techniques, CO conversion factors, spatial resolution or even the chosen fitting method could be a source of some scatter. The CO conversion factor is crucial in the starburst regime, and this many account for the offset in the transition region from starbursts to normal spirals.

However, this scatter is not present if we consider the tracks of individual galaxies on this relation. Shown in Figure 1.5 are a sample of different radial galaxy profiles, for both total gas and the molecular gas. Individual galaxies occupy their own region of the $\Sigma_{sfr} - \Sigma_g$ plane; there is a general trend but one clear slope or normalization. This implies that there may be a second parameter that dictates where galaxies live in this plane and that the scatter in the Kennicutt-Schmidt relation is intrinsic.

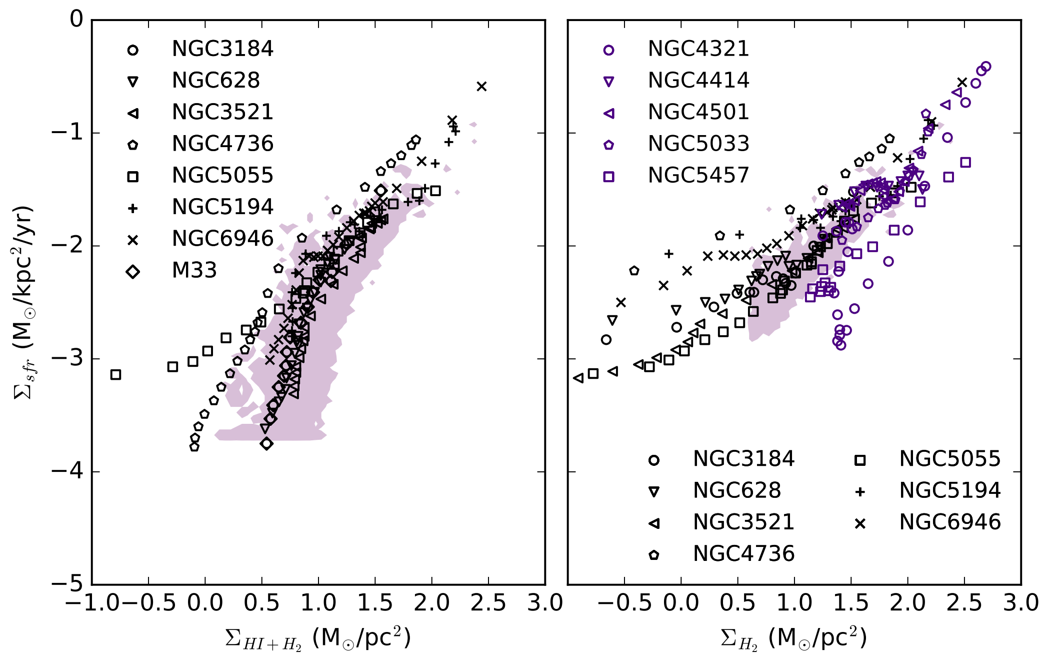

Figure 1.5: The Kennicutt-Schmidt relation in individual galaxies
The Kennicutt-Schmidt relation as measured in radial profiles. The purple contours show the region occupied by sub-kpc aperture measurements of galaxies as reported in Bigiel et al. (2008), as in Figure 1.4. The open symbols show radial profiles. The black open symbols are taken from Bigiel et al. (2008). The purple open symbols are taken from Wong & Blitz (2002) and Heyer et al. (2004). This reinforces that the scatter in the Kennicutt-Schmidt relation is intrinsic. Individual galaxies occupy tight tracks, but these tracks do not agree, leading to spread when all galaxies are combined.

There are different physical processes regulating star formation in the three different Σ_g regimes discussed above. In the starburst regime, $\Sigma_g \gtrsim 100$ M$_\odot$/pc^2, the timescale for star formation should be set by stellar feedback (e.g. Ostriker & Shetty, 2011; Shetty & Ostriker, 2012). In the normal spiral regime ($10 \lesssim \Sigma_g \lesssim 100$ M$_\odot$/pc^2), FUV heating from young stars may play a large role in this process, in combination with stellar feedback (e.g. Parravano, 1988; Ostriker et al., 2010; Kim et al., 2011).

In the portion of the relation where $\Sigma_g \lesssim 10$ M$_\odot$/pc^2, we enter an interesting regime. To some extent, star formation relies on the two-phase nature of the

ISM; there needs to be cold dense gas available to fuel star formation. If there is only a single warm phase present, star formation cannot occur. In this low surface density regime it is thought that the two-phase instability, or the derth of cold phase case, regulates star formation (e.g. Elmegreen & Parravano, 1994; Schaye, 2004). This is of additional interest as it is the regime into which the star-forming galaxy thresholds fall.

Referring back to Figure 1.3, there is no star formation in the outer disks of the galaxy. This is seen in all spirals, a fall-off in the star formation rate and molecular gas content, even though there is a significant fraction of atomic hydrogen available. This indicates some threshold either in star formation, or the conversion of HI to molecular gas and that it is tied to the conditions in the outer disks of galaxies.

There exists a strong correlation between the hydrostatic pressure and the molecular gas fraction in galaxies (Blitz & Rosolowsky, 2004, 2006). Pressure plays a role in the regulation of star formation. We can assume that gas exists in the ISM in either a cold dense or warm diffuse phase. Stars form from this cold dense phase. Star formation occurs as a result of gravitational instability. This gravitational force is a form of negative pressure. If there is not enough pressure generated by things like turbulence and feedback, there is an imbalance. It is this imbalance that causes gas to condense from the warm phase into the cold phase and form stars (e.g. Ostriker et al., 2010).

This concept can also help to explain some of the scatter in the Kennicutt-Schmidt relation. It has been suggested that a third parameter in this relation is the total stellar surface density (Shi et al., 2018). If we reparameterize the relation such that $\dot{\Sigma}_* \propto \Sigma_g \Sigma_*^N$, much of the scatter in the normal spiral regime can be eliminated. Many different parameterizations have been suggested, including using the orbital or free-fall time (e.g. Silk, 1997; Elmegreen, 1997; Salim et al., 2015). However, as of now, none can fully explain the intrinsic scatter or identify the missing parameter beyond a reasonable doubt.

1.3 Isolated galaxies as tools to study star formation

Section 1.1 details the process of using cosmological simulations to study star formation. However, star formation on the galactic scale is inextricably linked with the ISM. If we wish to study regulation in this context, we must resolve the ISM. At this point, this is not possible in cosmological volumes. This can be done in cosmological zoom-ins. However, these are very expensive as they cannot balance numerical load efficiently. Further, a large amount of the surrounding volume must be re-simulated, when it is of no interest to the galactic context.

An alternative route would be to study the ISM and star formation in pieces of galaxies, often kpc-scale (e.g. Walch et al., 2015). This offers higher resolution than could be achieved in a cosmological zoom. These studies often include complex chemistry models and are able to resolve high densities. The first problem with these types of approaches is that, unless a shearing box is used, the galactic shear is not accounted for. The galactic shear can be important to generate turbulence in the ISM (McNally et al., 2009). Further, the geometry of these boxes has severe consequences for stellar feedback. Outflow in the form of winds requires a spherical geometry, which is not the case when a stratified box is used. Galactic winds cannot be correctly modelled in the geometry present in these boxes. This leads to unrealistically bursty star formation and an over-pressurized ISM (Martizzi et al., 2016).

In the middle of these scales lies isolated galaxy simulations. These types of simulations do not employ the cosmological zoom technique. Instead, a single galaxy is modelled in isolation. Two approaches can be taken. The galaxy can be placed in a static halo potential, which saves resolution as dark matter and old stars are not required. Alternatively, the galaxy can live in a live dark matter and stellar halo. The second option is more numerically costly, but it is also more realistic.

There are a few main differences to consider between cosmological zoom-ins and isolated galaxies, which can operate on the same scales. First, isolated galaxies present the opportunity to have a more controlled halo or disk. This can be initialized as desired, and can be guaranteed to be axisymmetric, at least at the outset. Second, isolated galaxies do not have any infall, satellites or substructure. They cannot be used to test theories of CDM or to study how baryons get into galaxies; in that case a cosmological zoom-in is the better choice. Isolated galaxies focus instead on the processes internal to galaxies, not the larger hierarchy.

Even beyond these differences, as discussed earlier, there are many reasons to choose isolated galaxies. We are still not able to simulate galaxies ab initio - from the CMB to the Milky Way. However, observations have provided us with better and better measures of the empirical properties of galaxies. These measured properties of galaxies, especially at $z = 0$, are now well-known. If we match those galaxies from the start, without trying to generate them ab initio, we are creating a much more controlled situation in which to study star formation.

If the focus of a study is on these internal processes, then isolated galaxies offer a unique and largely under-utilized approach to studying star formation in galaxies. They offer the opportunity to tailor initial conditions to chosen galaxies in a way that is not possible in the cosmological context. They also offer the full galactic context, including shear, as opposed to stratified boxes. In this thesis, isolated galaxies are the chosen tool used to study star formation.

In the literature, isolated galaxies are typically used for studying the formation of giant molecular clouds. Isolated galaxies provide an opportunity to study the formation of these objects with a larger statistical sample, i.e. the whole disk. We are now at a point in time where we can simulate GMCs as they condense out of the disk in a way that we can match observational properties of GMCs, both in the Milky Way and other nearby galaxies (e.g. Tasker & Tan, 2009; Dobbs & Pringle, 2013; Benincasa et al., 2013). However, what is often missing from these studies is effective feedback algorithms. Recent studies have begun to address this issue, and study GMC formation in galaxies that include effective supernovae feedback (e.g. Ward et al., 2016; Grisdale et al., 2018).

Another common approach is to use isolated galaxies to calibrate feedback or star formation recipes. They can be used to explore the differences between different types of feedback physics (e.g. Hopkins et al., 2011, 2012) or star formation recipes (e.g. Hopkins et al., 2013; Semenov et al., 2016). They can also be used to test different ways of implementing supernovae feedback (e.g. Agertz et al., 2013).

In this work we use isolated galaxies to study the physical processes in galaxies. We specifically focus on star formation on the galactic scale. This is in contrast to studies that focus only on star formation in its context in molecular clouds. In this way, we hope to gain insight on dense structure formation and the physical origins of relations like the Kennicutt-Schmidt law.

1.4 This thesis

As discussed above, isolated galaxies provide a unique avenue to study star formation. At a time when we are beginning to try to link the smallest and largest scales of interest in galaxies, isolated galaxy simulations constitute a compelling approach. In this thesis we use this approach to study star formation in galaxies. In chapter 2, we explore the connection between the star formation rate and the total pressure. By using controlled simulations, we are able to create a quantitive model that describes how changes in the pressure equilibrium lead to changes in the star formation rate. In chapter 3 we develop a new method to study the formation of bound structure in galaxy simulations. We seed turbulent events and use the expected velocity spectrum to create a mass spectrum of bound objects. In chapter 4, we present the results of an isolated galaxy simulated with the new radiative transfer algorithm TREVR. This is the first full galaxy simulation to include both effective supernova feedback and self-consistent FUV heating provided by the radiative transfer. In this work, we return to explore the pressure balance model first discussed in chapter 2. Finally, in chapter 5 we summarize the achievements of this work and discuss future directions.

Bibliography

Agertz, O. and Kravtsov, A. V. and Leitner, S. N. and Gnedin, N. Y., 2013, ApJ, 770, 25

Behroozi, P. S., Conroy, C. and Wechsler, R. H., 2010, ApJ, 717, 379

Behroozi, P. S. and Wechsler, R. H. and Conroy, C., 2013, ApJ, 770, 57

Benincasa, S. M. and Tasker, E. J. and Pudritz, R. E. and Wadsley, J., 2013, ApJ, 776, 23

Bigiel, F., Leroy, A., Walter, F., Brinks, E., de Blok, W. J. G., Madore, B. and Thornley, M. D., 2008, AJ, 136, 1846

Blitz, L. and Rosolowsky, E., 2006, ApJ, 650, 933

Blitz, L. and Rosolowsky, E., 2004, ApJ, 612, L29

Blumenthal, G. R., Faber, S. M., Primack, J. R. and Rees, M. J., 1984, Nature, 311, 517

Bond, J. R., Cole, S., Efstathiou, G. and Kaiser, N., ApJ, 1991, 379, 440

Brooks, A. M. and Zolotov, A., 2014, ApJ, 786, 87

Chomiuk, L. and Povich, M. S., 2011, AJ, 142, 197

Colless, M. and Dalton, G. and Maddox, S. and Sutherland, W. and Norberg, P. and Cole, S. and Bland-Hawthorn, J. and Bridges, T. and Cannon, R. and Collins, C. and Couch, W. and Cross, N. and Deeley, K. and De Propris, R. and Driver, S. P. and Efstathiou, G. and Ellis, R. S. and Frenk, C. S. and Glazebrook, K. and Jackson, C. and Lahav, O. and Lewis, I. and Lumsden, S. and Madgwick, D. and Peacock, J. A. and Peterson, B. A. and Price, I. and Seaborne, M. and Taylor, K., 2001, MNRAS, 328, 1039

Colombo, D. and Hughes, A. and Schinnerer, E. and Meidt, S. E. and Leroy, A. K. and Pety, J. and Dobbs, C. L. and García-Burillo, S. and Dumas, G. and Thompson, T. A. and Schuster, K. F. and Kramer, C., 2014, ApJ, 784, 3

Colombo, D. and Meidt, S. E. and Schinnerer, E. and García-Burillo, S. and Hughes, A. and Pety, J. and Leroy, A. K. and Dobbs, C. L. and Dumas, G. and Thompson, T. A. and Schuster, K. F. and Kramer, C., 2014, ApJ, 784, 4

Conroy, C. and Wechsler, R. H., 2009, ApJ, 696, 620

Corbelli, E. and Braine, J. and Bandiera, R. and Brouillet, N. and Combes, F. and Druard, C. and Gratier, P. and Mata, J. and Schuster, K. and Xilouris, M. and Palla, F., 2017, A&A, 601, A146

Dobbs, C. L. and Pringle, J. E., 2013, MNRAS, 432, 653

Eadie, G. M. and Springford, A. and Harris, W. E., 2017, ApJ, 835, 167

Elmegreen, B. G., 1997, Revista Mexicana de Astronomia y Astrofisica Conference Series, 6, 165

Elmegreen, B. G. and Parravano, A., 1994, ApJ, 435, L121

Fall, S. M. and Efstathiou, G., 1980, MNRAS, 193, 189

Garrison-Kimmel, S. and Hopkins, P. F. and Wetzel, A. and Bullock, J. S. and Boylan-Kolchin, M. and Keres, D. and Faucher-Giguere, C.-A. and El-Badry, K. and Lamberts, A. and Quataert, E. and Sanderson, R., 2018, arXiv:1806.04143

Geller, M. J. and Huchra, J. P., 1989, Science, 246, 897

Giavalisco, M. et al., 2004, ApJ, 600, L93

Gil de Paz, A. and Boissier, S. and Madore, B. F. and Seibert, M. and Joe, Y. H. and Boselli, A. and Wyder, T. K. and Thilker, D. and Bianchi, L. and Rey, S.-C. and Rich, R. M. and Barlow, T. A. and Conrow, T. and Forster, K. and Friedman, P. G. and Martin, D. C. and Morrissey, P. and Neff, S. G. and Schiminovich, D. and Small, T. and Donas, J. and Heckman, T. M. and Lee, Y.-W. and Milliard, B. and Szalay, A. S. and Yi, S., 2007, ApJS, 173, 185

Grisdale, K. and Agertz, O. and Renaud, F. and Romeo, A. B., 2018, MNRAS, 479, 3167

Grogin, N. A. et al., 2011, ApJS, 197, 35

Guth, A. H., 1981, Phys. Rev. D, 23, 347

Hao, C.-N., Kennicutt, R. C., Johnson, B. D., Calzetti, D., Dale, D. A. and Moustakas, J., 2011, 741, 124

Heyer, M. H. and Corbelli, E. and Schneider, S. E. and Young, J. S., 2003, ApJ, 602, 723

Hopkins, P. F. and Narayanan, D. and Murray, N., 2013, MNRAS, 432, 2647

Hopkins, P. F. and Quataert, E. and Murray, N., 2012, MNRAS, 421, 3488

Hopkins, P. F. and Quataert, E. and Murray, N., 2011, MNRAS, 417, 950

Hudson, M. J., Gillis, B. R., Coupon, J., Hildebrandt, H., Erben, T., Heymans, C., Hoekstra, H., Kitching, T. D., Mellier, Y., Miller, L., Van Waerbeke, L., Bonnett, C., Fu, L., Kuijken, K., Rowe, B., Schrabback, T., Semboloni, E., van Uitert, E. and Velander, M., 2015, MNRAS, 447, 298

Keller, B. W. and Wadsley, J. and Couchman, H. M. P., 2016, MNRAS, 463, 1431

Kennicutt, Jr., R. C., 1998, ApJ, 498, 541

Kennicutt, Jr., R. C. and Armus, L. and Bendo, G. and Calzetti, D. and Dale, D. A. and Draine, B. T. and Engelbracht, C. W. and Gordon, K. D. and Grauer, A. D. and Helou, G. and Hollenbach, D. J. and Jarrett, T. H. and Kewley, L. J. and Leitherer, C. and Li, A. and Malhotra, S. and Regan, M. W. and Rieke, G. H. and Rieke, M. J. and Roussel, H. and Smith, J.-D. T. and Thornley, M. D. and Walter, F., 2003, PASP, 115, 928

Kennicutt, Jr., R. C. and Calzetti, D. and Walter, F. and Helou, G. and Hollenbach, D. J. and Armus, L. and Bendo, G. and Dale, D. A. and Draine, B. T. and Engelbracht, C. W. and Gordon, K. D. and Prescott, M. K. M. and Regan, M. W. and Thornley, M. D. and Bot, C. and Brinks, E. and de Blok, E. and de Mello, D. and Meyer, M. and Moustakas, J. and Murphy, E. J. and Sheth, K. and Smith, J. D. T., 2007, ApJ, 671, 333

Kennicutt, R. C. and Evans, N. J., 2012, ARA&A, 50, 531

Kim, C.-G. and Kim, W.-T. and Ostriker, E. C., 2011, ApJ, 743, 25

Klypin, A. and Kravtsov, A. V. and Valenzuela, O. and Prada, F., 1999, ApJ, 522, 82

Lada, C. J. and Lombardi, M. and Alves, J. F., 2010, ApJ, 724, 687

Lee, M.-Y. and Stanimirović, S. and Douglas, K. A. and Knee, L. B. G. and Di Francesco, J. and Gibson, S. J. and Begum, A. and Grcevich, J. and Heiles, C. and Korpela, E. J. and Leroy, A. K. and Peek, J. E. G. and Pingel, N. M. and Putman, M. E. and Saul, D., 2012, ApJ, 748, 75

Leroy, A. K. and Walter, F. and Bigiel, F. and Usero, A. and Weiss, A. and Brinks, E. and de Blok, W. J. G. and Kennicutt, R. C. and Schuster, K.-F. and Kramer, C. and Wiesemeyer, H. W. and Roussel, H., 2009, AJ, 137, 4670

Licquia, T. C. and Newman, J. A., 2015, ApJ, 806, 96

Linde, A. D., 1982, Physics Letters B, 108, 389

Madau, P., Pozzetti, L. and Dickinson, M., 1998, ApJ, 498, 106

Martizzi D., Fielding D., Faucher-Giguère C.-A., Quataert E., 2016, MNRAS, 459, 2311

McKee, C. F. and Ostriker, E. C., 2007, ARA&A, 45, 565

McMillan, P. J., 2011, MNRAS, 414, 2446

McNally C. P., Wadsley J., Couchman H. M. P., 2009, ApJ, 697, L162

Meidt, S. E. and Hughes, A. and Dobbs, C. L. and Pety, J. and Thompson, T. A. and García-Burillo, S. and Leroy, A. K. and Schinnerer, E. and Colombo, D. and

Querejeta, M. and Kramer, C. and Schuster, K. F. and Dumas, G., 2015, ApJ, 806, 72

Mo, H. and van den Bosch, F. C. and White, S.,"Galaxy Formation and Evolution",UK: Cambridge University Press, 2010

Moore, B. and Ghigna, S. and Governato, F. and Lake, G. and Quinn, T. and Stadel, J. and Tozzi, P., 1999, ApJ, 524, L19

Moster, B. P., Naab, T. and White, S. D. M., 2013, MNRAS, 428, 3121

Müller, O., Pawlowski, M. S., Jerjen, H. and Lelli, F., 2018, Science, 359, 534

Murphy, E. J., Condon, J. J., Schinnerer, E., Kennicutt, R. C., Calzetti, D., Armus, L., Helou, G., Turner, J. L., Aniano, G., Beirão, P., Bolatto, A. D., Brandl, B. R., Croxall, K. V., Dale, D. A., Donovan Meyer, J. L., Draine, B. T., Engelbracht, C., Hunt, L. K., Hao, C.-N., Koda, J., Roussel, H., Skibba, R. and Smith, J.-D. T., 2011, ApJ, 737, 67

Navarro, J. F., Frenk, C. S. and White, S. D. M., 1996, ApJ, 462, 563

Ostriker, E. C. and Shetty, R., 2011, ApJ, 731, 41

Ostriker E. C., McKee C. F., Leroy A. K., 2010, ApJ, 721, 975

Parravano, A., 1988, A&A, 205, 71

Planck Collaboration, Ade, P. A. R., Aghanim, N., Arnaud, M., Ashdown, M., Aumont, J., Baccigalupi, C., Banday, A. J., Barreiro, R. B., Bartlett, J. G. and et al., 2016, A&A, 594, A13

Press, W. H. and Schechter, P., ApJ, 187, 425

Rees, M. J. and Ostriker, J. P., 1977, MNRAS, 179, 541

Rieke, G. H., Alonso-Herrero, A., Weiner, B. J., Pérez-González, P. G., Blaylock, M., Donley, J. L. and Marcillac, D., 2009, ApJ, 692, 556

Saintonge, A. and Kauffmann, G. and Kramer, C. and Tacconi, L. J. and Buchbender, C. and Catinella, B. and Fabello, S. and Graciá-Carpio, J. and Wang, J. and Cortese, L. and Fu, J. and Genzel, R. and Giovanelli, R. and Guo, Q. and Haynes, M. P. and Heckman, T. M. and Krumholz, M. R. and Lemonias, J. and Li, C. and Moran, S. and Rodriguez-Fernandez, N. and Schiminovich, D. and Schuster, K. and Sievers, A., 2011, MNRAS, 415, 32

Salim, D. M. and Federrath, C. and Kewley, L. J., 2015, ApJ, 806, L36

Salmon, B., Coe, D., Bradley, L., Bradač, M., Huang, K.-H., Strait, V., Oesch, P., Paterno-Mahler, R., Zitrin, A., Acebron, A., Cibirka, N., Kikuchihara, S., Oguri, M., Brammer, G. B., Sharon, K., Trenti, M., Avila, R. J., Ogaz, S., Andrade-Santos, F., Carrasco, D., Cerny, C., Dawson, W., Frye, B. L., Hoag, A., Jones, C., Mainali, R., Ouchi, M., Rodney, S. A., Stark, D. and Umetsu, K., 2018, arXiv:1801.03103

Schaye, J., 2004, ApJ, 609, 667

Schinnerer, E., Meidt, S. E., Pety, J., Hughes, A., Colombo, D., García-Burillo, S., Schuster, K. F., Dumas, G., Dobbs, C. L., Leroy, A. K., Kramer, C., Thompson, T. A. and Regan, M. W., 2013, ApJ, 779, 42

Schinnerer, E. and Meidt, S. E. and Colombo, D. and Chandar, R. and Dobbs, C. L. and García-Burillo, S. and Hughes, A. and Leroy, A. K. and Pety, J. and Querejeta, M. and Kramer, C. and Schuster, K. F., 2017, ApJ, 836, 62

Schmidt, M., 1959, ApJ, 129, 243

Schruba, A. and Leroy, A. K. and Walter, F. and Bigiel, F. and Brinks, E. and de Blok, W. J. G. and Dumas, G. and Kramer, C. and Rosolowsky, E. and Sandstrom, K. and Schuster, K. and Usero, A. and Weiss, A. and Wiesemeyer, H., 2011, AJ, 142, 37

Semenov, V. A. and Kravtsov, A. V. and Gnedin, N. Y., 2016, ApJ, 826, 200

Shetty, R. and Ostriker, E. C., 2012, ApJ, 754, 2

Shi, Y. and Yan, L. and Armus, L. and Gu, Q. and Helou, G. and Qiu, K. and Gwyn, S. and Stierwalt, S. and Fang, M. and Chen, Y. and Zhou, L. and Wu, J. and Zheng, X. and Zhang, Z.-Y. and Gao, Y. and Wang, J., 2018, ApJ, 853, 149

Silk, J., 1997, ApJ, 481, 703

Springel, V., Frenk, C. S. and White, S. D. M., 2006, Nature, 440, 1137

Springel, V., White, S. D. M., Jenkins, A., Frenk, C. S., Yoshida, N., Gao, L., Navarro, J., Thacker, R., Croton, D., Helly, J., Peacock, J. A., Cole, S., Thomas, P., Couchman, H., Evrard, A., Colberg, J. and Pearce, F., 2005, Nature, 435, 629

Sun J., et al., 2018, ApJ, 860, 172

Tasker, E. J. and Tan, J. C., 2009, ApJ, 700, 358

van Dokkum, P. G., Leja, J., Nelson, E. J., Patel, S., Skelton, R. E., Momcheva, I., Brammer, G., Whitaker, K. E., Lundgren, B., Fumagalli, M., Conroy, C., Förster Schreiber, N., Franx, M., Kriek, M., Labbé, I., Marchesini, D., Rix, H.-W., van der Wel, A. and Wuyts, S., 2013, ApJ, 771, L35

Walter, F. and Brinks, E. and de Blok, W. J. G. and Bigiel, F. and Kennicutt, Jr., R. C. and Thornley, M. D. and Leroy, A. , 2008, AJ, 136, 2563

Walch, S. and Girichidis, P. and Naab, T. and Gatto, A. and Glover, S. C. O. and Wünsch, R. and Klessen, R. S. and Clark, P. C. and Peters, T. and Derigs, D. and Baczynski, C., 2015, MNRAS, 454, 238

Ward, R. L. and Benincasa, S. M. and Wadsley, J. and Sills, A. and Couchman, H. M. P., 2016, MNRAS, 455, 920

White, S. D. M. and Rees, M. J., 1978, MNRAS, 183, 341

Wilson, C. D. and Warren, B. E. and Israel, F. P. and Serjeant, S. and Bendo, G. and Brinks, E. and Clements, D. and Courteau, S. and Irwin, J. and Knapen, J. H. and Leech, J. and Matthews, H. E. and Mühle, S. and Mortier, A. M. J. and Petitpas, G. and Sinukoff, E. and Spekkens, K. and Tan, B. K. and Tilanus, R. P. J. and Usero, A. and van der Werf, P. and Wiegert, T. and Zhu, M., 2009, ApJ, 693, 1736

Wong, T. and Blitz, L., ApJ, 569, 157

York, D. G. et al. and SDSS Collaboration, 2000, AJ, 120, 1579

Chapter 2

The anatomy of a star-forming galaxy: Pressure-driven regulation of star formation in simulated galaxies

S. M. Benincasa, J. W. Wadsley, H. M. P. Couchman, and B. W. Keller

2016, The Monthly Notices of the Royal Astronomical Society, Volume 462, Issue 3, pp. 3053–3068, DOI: 10.1093/mnras/stw1741. Reproduced with permission from the Monthly Notices of the Royal Astronomical Society and Oxford University Press.

Abstract

We explore the regulation of star formation in star-forming galaxies through a suite of high-resolution isolated galaxy simulations. We use the SPH code GASOLINE, including photoelectric heating and metal cooling, which produces a multi-phase interstellar medium. We show that representative star formation and feedback sub-grid models naturally lead to a weak, sub-linear dependence between the amount of star formation and changes to star formation parameters. We incorporate these sub-grid models into an equilibrium pressure-driven regulation framework. We show that the sub-linear scaling arises as a consequence of the non-linear relationship between scale height and the effective pressure generated by stellar feedback. Thus, simulated star-formation regulation is sensitive to how well vertical structure in the ISM is resolved. Full galaxy disks experience density waves which drive locally time-dependent star formation. We develop a simple time-dependent, pressure-driven model that reproduces the response extremely well.

2.1 Introduction

The process of star formation is limited, in principle, by the availability of cold, dense gas fuel. However, in typical disk galaxies it proceeds inefficiently relative to characteristic time-scales for the gas, such as the local free-fall time in Giant Molecular Clouds (~ 10 Myr). In fact, globally, star formation proceeds on a time-scale comparable to several galactic rotation periods ($\sim$1 Gyr, Kennicutt, 1998; Krumholz & Tan, 2007). This is commonly attributed to self-regulation. Highly resolved samples of nearby star-forming galaxies, such as The HI Nearby Galaxies Survey (THINGS, Walter et al., 2008), the PdBI Arcsecond Whirlpool Survey (PAWS, Schinnerer et al., 2013), and the Panchromatic Hubble Andromeda Treasury (PHAT, Dalcanton et al., 2012) have provided a detailed look at the interstellar medium (ISM) on sub-kpc scales. This lets us connect the local physics of the ISM to the regulation of star formation on larger scales(e.g. Krumholz et al., 2009).

Although observations indicate that star formation must be regulated overall, the details of regulation are difficult to pin down using observational data due to the timing offset between tracers of gas and tracers of star formation (e.g. Kruijssen & Longmore, 2014). Thus the physical cycle of regulation is most easily studied theoretically. Simulations using isolated galaxies have tended to focus on exploring different kinds of feedback and overall star formation rates (Hopkins et al., 2011, 2012). Galaxy-scale simulations cannot directly resolve the detailed process of regulation, leading to increasingly complex sub-grid models. Studies of star-formation regulation have also been extended into the cosmological context (Agertz et al., 2013; Agertz & Kravtsov, 2015). Going to larger scales includes more of the galactic environment at the cost of lower resolution which potentially compromise elements of the regulation mechanism.

Ostriker et al. (2010) presented a detailed semi-analytical model of equilibrium star formation and applied it to the THINGS galaxy sample. In this model, star formation is regulated by satisfying two equilibria in a galaxy. The first, a vertical dynamical equilibrium, requires a balance between ISM weight and pressure support. The second, a thermal or energy equilibrium, requires energy balance between feedback and heating/cooling processes (Ostriker et al., 2010; Ostriker & Shetty, 2011; Kim et al., 2011; Kim & Ostriker, 2015). In this work we do not need to make any explicit assumptions regarding energy balance as the simulations do that explicitly.

Following the first requirement, the ISM is compressed by its own weight, set by the gas column and the gravity of the various components of the galaxy (gas, dark matter and stars). The weight is then a function of the height of the gas layers. This sets an expected pressure at the mid-plane, which determines the cold gas fraction via the two-phase instability. Star formation occurs steadily in cold, dense gas. To keep this model consistent, the ISM must have sufficient means of support to provide that mid-plane pressure. In the Ostriker et al. (2010) model, this pressure is effectively set by the star formation rate. The equilibrium semi-analytic model provided an excellent fit to star formation rates in the THINGS galaxies, where the vertical gravity is dominated by stars.

Determining the total effective pressure is key for vertical pressure balance. The dominant mechanisms providing this effective pressure support can change in different environments. In most nearby galaxies ($\Sigma_g \gtrsim 10$ M$_\odot$ pc^{-2}), however, pressure from turbulent support plays the major role. This model assumption has been tested on small scales and in two- and three-dimensional simulations (Kim et al., 2011; Ostriker & Shetty, 2011). Stellar feedback is responsible for generating this support. This may come from supernovae, however, in starbursts, some authors argue that alternate mechanisms, such as radiation pressure, play a major role (Hopkins et al., 2011). Supernovae as regulators of star formation have been explored through small-box simulations in several works (e.g. de Avillez & Breitschwerdt, 2005; Joung et al., 2009; Creasey et al., 2013).

In the prior scenarios, the effective pressure is strongly linked to the local star formation rate. We note in passing that in the outer regions of disks, ($\Sigma_{\rm g} \lesssim 10$ $M_\odot$ pc^{-2}), gas could be supported due to non-local heating or turbulence associated with galactic shear (McNally et al., 2009). A two-phase structure may not develop, limiting star formation in these environments (Elmegreen & Parravano, 1994; Schaye, 2004).

Local simulations with a fixed surface density are conducive to reaching a steady equilibrium and thus ideal to study the hydrostatic, equilibrium framework of the Ostriker et al. (2010) model. Pressure-driven regulation should also play a key role in disk-scale simulations, with the addition of time dependent, spatial variations. Isolated galaxy simulations naturally include all of the necessary components (e.g. large-scale shear) but still allow relatively high resolution for the ISM. High-resolution simulations of isolated galaxies have been extensively used to study the formation of dense star-forming gas (Dobbs, 2008; Dobbs et al., 2011; Renaud et al., 2013; Tasker & Tan, 2009; Tasker, 2011). However, a realistic feedback and star-formation regulation cycle was not a major focus of these works.

Examining pressure balance and star-formation regulation requires high numerical resolution. Fundamentally, one must be able to resolve the scale height of the gas disk, particularly for the colder phases, where stars form, which have scale heights of order 100 pc or less. Forming multiple phases is also numerically demanding. Turbulence is an important contributor to the detailed structure of star forming clouds. As a result, galaxy-scale simulations can directly examine star cluster-scale formation at best. Thus even high-resolution simulations must still rely on star formation recipes. Turbulence also contributes to regulation and pressure support. Galactic turbulence is generated at a range of scales up to several kpc and then cascades down to smaller scales. Simulations have difficulty maintaining this cascade. In particular turbulent energy is typically suppressed (via numerical dissipation) on scales substantially above the resolution limit (Price & Federrath, 2010). In galaxy-scale simulations this severely limits turbulence on small scales in the ISM. However, turbulence on scales comparable to the scale height is strongly linked to stellar feedback and thus star-formation regulation. An attractive option is to avoid the numerical issues by injecting energy on small scales as an effective pressure as in Agertz et al. (2013).

The pressure-driven regulation framework has profound implications for simulators. The fact that most simulated models are able to regulate star formation suggests that just providing a source of effective pressure linked to young stars is sufficient for basic regulation. In addition, star formation and feedback models typically have a lot of parameter freedom to tune star formation rates to match expectations. Thus achieving regulation or even tuning it to match a narrow set of observations is not that remarkable. The pressure-driven picture should explain these results if we incorporate typical sub-grid models into the framework.

For example, a common outcome from the prior work discussed above has been that simulated star formation rates do not scale linearly with variations in star formation and feedback parameters (e.g. Hopkins et al., 2011). Linear scaling in the star formation rate constant, for example, would be the naive expectation. This assumes that star formation and the ISM are weakly coupled. However, variations in key ISM properties such as scale height are likely to be artificially limited at low resolution. By moving to higher resolution than has typically been employed for many sub-grid models in use today, one can probe how robust these results are.

The above issues with sub-grid star formation in whole-galaxy simulations undermine the common approach of using regulated star formation as the primary benchmark for a successful model. The key question raised is whether the regulation achieved in simulated galaxies is actually similar to that occurring in nature. An associated question is how much predictive power these models have when used outside the cases on which they were calibrated.

The pressure regulation idea is extremely general and should apply to all steadily evolving galaxies, even as conditions and modes of feedback are varied. Small scale simulations have confirmed the utility of these ideas for local, relatively uniform conditions (e.g. Kim et al., 2011, 2013). We would like to apply this insight to understand simulations on the scale of a whole galaxy. To do so we should extend the framework to include the time dependent behaviour, (e.g. in response to density waves), expected in the broader galactic context. To do so, one needs to move from vertical hydrostatic equilibrium to a non-equilibrium pressure-driven framework.

In the current work, we employ a suite of high resolution simulations of isolated galaxies to explore basic ideas of star-formation regulation. Though we use high resolution and incorporate a fairly complex ISM model, we have kept the star formation and feedback prescriptions simple to make the results easier to interpret. None-the-less, these models are quite similar to the most popular star formation and feedback models in use in simulations at the current time and should therefore also provide direct insight into how those models operate.

Given that our resolution is much higher than much of the early work in which the sub-grid models were developed (e.g. Stinson et al., 2006), a first step is to test basic sensitivity to parameter choices. We can also compare to other recent, high-resolution simulations of isolated galaxies, which have tended to use much more complex feedback (e.g. Hopkins et al., 2011).

A further feature of this work is to test the pressure-driven framework in a dynamic environment with time dependence and spatial variations (e.g. density waves) arising naturally in a galactic setting. This necessitates extending the model into a time-dependent, (non-equilibrium) pressure-driven framework.

The structure of the paper is as follows. In section 2.2, we describe our simulation set-up for an isolated galaxy and our simple feedback recipe. In section 2.3, we characterize the overall simulated galaxy behaviour. In particular, it shows sub-linear scaling of star formation rates with respect to the model parameters and we explore how these arise. In section 2.4, we demonstrate that the galaxies were behaving in a manner consistent with expectations from the pressure balance framework. Section 2.5 demonstrates the local time variability in star formation and associated ISM properties. Finally, in section 2.6, we present a time-dependent model extension of the pressure-driven framework. This reproduces the behaviour seen in the simulations including the sub-linear scaling with star formation parameters.

2.2 Simulation Method

We use the modern SPH code GASOLINE (Wadsley et al., 2004) including recent improvements (with details described in Keller et al., 2014). Our simulations are high resolution, with a particle mass of 442 $M_\odot$ (force softening length of 20 pc). These choices allow us to resolve the scale height of the disk. Our simulations also form GMC-scale dense clouds, meaning we can maintain two-phase structure in our ISM (for a detailed study of GMCs formed in our simulations see Ward et al., 2016).

This resolution is similar to that used by Hopkins et al. (2011). The new features used in this work include a treatment for photoelectric heating in the ISM and a simpler feedback model, described below.

2.2.1 Photoelectric heating

The dominant source of heating due to photoelectric absorption by dust grains comes from Ultra-Violet (UV) radiation from stars. The heating rate due to photoelectric heating is set by

$$n\Gamma_{\rm PE} = 10^{-24}\epsilon n G_0 \text{ erg cm}^{-3}\text{ s}^{-1} \tag{2.1}$$

where ϵ represents a heating efficiency, G_0 is the intensity of the radiation field in units of the average interstellar radiation field and n is the number density of the gas. In this work we assume that $\epsilon G_0 \sim 0.05$ (Tielens, 2005). To model this photoelectric heating throughout the disk we employ a FUV heating term similar to Tasker & Tan (2009):

$$n\Gamma_{\rm FUV} = n\Gamma_{\rm PE} \times \begin{cases} e^{-(4-R_0)/4} & : \; R < 4 \text{ kpc} \\ e^{-(R-R_0)/4} & : \; R \geq 4 \text{ kpc} \end{cases} \tag{2.2}$$

with $R_0 = 8.5$ kpc, where R is a cylindrical radius. This functional form is chosen to match the FUV profile used in Wolfire et al. (2003) which was derived from an assumed distribution of young stars consistent with the Milky Way. Thus, for the current work the FUV heating is not directly coupled to simulated star formation events. However, the typical Galactic optical depth to FUV is fairly low, with mean free paths of order a kpc. A smoothed FUV field is a reasonable approximation and

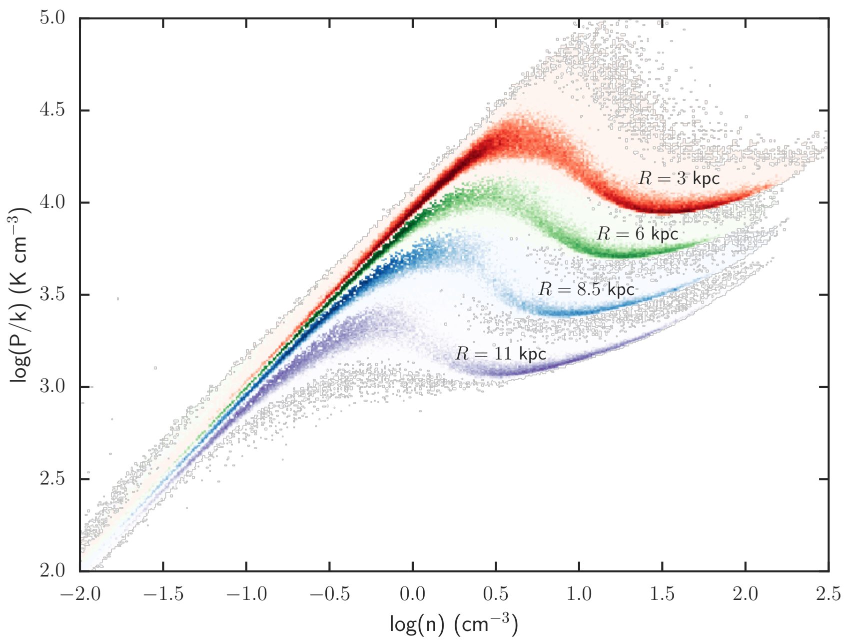

Figure 2.1: Phase diagram for the reference galaxy

Phase diagram for the reference galaxy at a time of 500 Myr. Gas was sampled in annuli centred at the labelled radii +/- 50 pc, with different colouring denoting different radii. Here, darker colouring denotes more mass residing at that location in the phase space. Since the photoelectric heating term varies with radius, the equilibrium is different at different radii in the disk. This variation changes the minimum density required to maintain a two-phase structure in the ISM.

this was assumed by Wolfire et al. (2003) in deriving a radial profile. We expect star formation to occur throughout the disk in a distribution similar to the one that gives rise to this FUV field and this was the outcome seen in our simulation runs. This approach has been used in other simulations (Dobbs et al., 2011; Tasker, 2011). A higher degree of consistency would require simulated radiative transfer.

We also approximate the depletion of elements onto dust grains. This is done by multiplying the total metal abundance by a constant depletion factor of 0.4, similar to that assumed in Wolfire et al. (2003). This generates a linear decrease in the metal cooling which gives a closer match to the heating and cooling behaviour in Wolfire et al. (2003).

The outcome of this treatment for photoelectric heating is shown in Figure 2.1. The phase diagram is shown for our reference galaxy at the final output time of 500 Myr. The phase diagram is plotted for four different radii; 3, 8.5 and 11 kpc (for comparison, see Wolfire et al. (2003) Figure 7). For the four tracks shown, areas of dark colour correspond to areas in the phase space containing more mass. In each case we see a clear preference for gas to be in either a warm or cold ISM phase. Our simulations are successful at producing an ISM with two-phase structure. Note the finite thickness and presence of some material in the unstable regime. These effects are due to the dynamics present in the simulations which occur on time-scales similar to or smaller than the characteristic time required for complete two-phase separation.

2.2.2 Star formation and feedback

The star formation recipe used here is as described in Stinson et al. (2006) with some modifications. In the recipe, stars form following a Schmidt law:

$$\frac{\mathrm{d}\rho_*}{\mathrm{d}t} = c_* \frac{\rho_g}{t_{dyn}}, \tag{2.3}$$

where ρ_* is the density of new stars formed, ρ_g is the density of eligible gas, $t_{dyn} = 1/\sqrt{4\pi G\rho}$ is the dynamical time and c_* is the chosen efficiency (see section 2.3). Gas is considered eligible for star formation if it lies above a set density threshold, below a maximum temperature and belongs to a converging flow.

The original recipe required that gas particles be below a set temperature threshold to form stars. We now compare the effective temperature associated with the total energy (including thermal and non-cooling, as discussed below) to the threshold value. This ensures that feedback will always locally limit star formation. In this work the temperature threshold value is taken at 100 K. The key star formation model parameters that apply here are the minimum density threshold for gas to form stars (n_{th}), the star formation efficiency per dynamical time (c_*) and the feedback efficiency (ϵ_{fb}) relative to the standard amount from supernovae, as described below.

We employ the supernova feedback method of Agertz et al. (2013). This model differs from the older blastwave model of Stinson et al. (2006) and the newer superbubble model of Keller et al. (2014) in that it is a simpler way to deposit the energy from SNe that still produces similar results and robust feedback regulation. Specifically, rather than being a complex function of local properties, the conversion time for injected energy is a set parameter. This gives us direct knowledge of how long feedback energy remains available as effective pressure and removes the associated uncertainty in interpreting our results. In more detailed models, feedback energy might take the form of pockets of hot gas, cosmic rays, radiation pressure, winds and small-scale turbulence, all injected on initially very small scales ($\sim$pc, see e.g. Hopkins et al., 2012). Many of these processes are difficult to model, convert energy rapidly from one form to another and suffer from numerical effects including excess dissipation. The associated effective pressures become important for driving dynamics when they act on scales comparable to the scale height. A simple model ensures a well characterized coupling of feedback energy to the dynamics on these scales. It also allows us to side-step the unresolved issue of the relative importance of different types of feedback energy and how efficiently it converts into different forms.

We normalize our energy input relative to that of supernovae. A single supernova deposits 10^{51} erg of energy into the surrounding ISM. Based on the stellar initial mass function of Chabrier (2003), approximately one in 100 stars will undergo a supernova event, resulting in an average specific supernova energy of 10^{49} erg/M$_{\odot}$. On average, this energy is injected steadily over the first 40 Myr after the formation of a star cluster. In this method, feedback energy, E_{fb}, does not cool radiatively and is steadily converted into regular thermal energy at a fixed rate similar to Agertz et al. (2013). The relevant energy equations are,

$$\frac{\mathrm{d}u_{\text{th}}}{\mathrm{d}t} = \frac{u_{\text{fb}}}{\tau} + \dot{u}_{\text{th},P\mathrm{d}V} - \Lambda \tag{2.4a}$$

$$\frac{\mathrm{d}u_{\text{fb}}}{\mathrm{d}t} = -\frac{u_{\text{fb}}}{\tau} + \dot{u}_{\text{fb},P\mathrm{d}V} + \dot{u}_{\text{fb},*} \tag{2.4b}$$

where u_{th} is gas thermal energy, u_{fb} is the non-cooling energy, $\dot{u}_{P\mathrm{d}V}$ represents energy exchanges due to hydrodynamics, Λ is the cooling rate and $\dot{u}_{\text{fb},*}$ is new feedback energy injected by stars. Feedback energy can be decreased through PdV work pushing the gas around and is also steadily converted back into the regular, cooling form. This latter change occurs over a chosen conversion time-scale, τ. For the purpose of this work, we adopt a conversion time of $\tau = 5$ Myr. This energy deposition due to supernovae will begin immediately after a star cluster forms. This covers the period where other forms of feedback are effective such as stellar winds. Thus in this model, the exact nature of the feedback is not specified, just that the total energy is measured relative to the expected supernova amount and that it is injected over a time period from the formation of the star cluster for a period of 40 Myr as determined by the supernova rate.

2.2.3 Initial conditions

We generated our suite of high resolution galaxy simulations around a common galaxy model. Detailed descriptions of parameter choices for each run are discussed in section 2.3.1. The isolated disk galaxy model was given a density profile decreasing exponentially with radius as follows,

$$\Sigma_g(R) = \Sigma_0 \left(\frac{R^2}{R^2+1} \right) e^{-(R-8)/5} \tag{2.5}$$

where R is a cylindrical radius in kpc and Σ_0 =14 M$_\odot$ pc^{-2}, chosen to model a Milky Way-type galaxy. This results in a disk with a total gas mass of 7.51$\times$10^9 M$_\odot$. For comparison, the gas mass of the Milky Way is approximately 4.5×10^9 M$_\odot$ (Tielens, 2005). We exclude the centre of the disk at radii interior to 1 kpc. By excluding this region, we do not have to resolve nuclear star formation. Choosing to have an unresolved galaxy centre, or not have a centre at all are common strategies (e.g. Dobbs, 2008; Benincasa et al., 2013).

The disks were evolved in a static dark matter halo potential. A log halo potential was used:

$$\Phi_{\mathrm{L}} = \frac{1}{2} v_0^2 \ln\left(R_c^2 + R^2 + \frac{z^2}{q_\Phi^2}\right) \tag{2.6}$$

where $R,\ R_c$ and z are in units of kpc. This gives a circular speed as a function of radius of:

$$v_c = \frac{v_0 R}{\sqrt{R_c^2 + R^2}} \tag{2.7}$$

(Binney & Tremaine, 2008). For our galaxy, $q_\Phi = 1$, $R_c = 1$ kpc, and $v_0 = 220$ km s^{-1}. Again, we choose v_c to match the rotation velocity at the solar radius in the Milky Way.

2.3 Simulations

2.3.1 The simulation suite

The suite of high resolution isolated galaxy simulations primarily explored the three parameters from the star formation and feedback recipes: the density threshold (n_{th}), the star formation efficiency per dynamical time (c_*) and the feedback efficiency (ϵ_{fb}). We chose as our reference parameter set a density threshold of $n_{\mathrm{th}} = 100$ cm^{-3}, a star formation efficiency of $c_* = 6\%$ and a feedback efficiency of $\epsilon_{\mathrm{fb}} = 100\%$. Our choice of threshold coincides with the average density of GMCs. Our reference efficiency per dynamical time of 6%, corresponds to ∼3% per free-fall time ($t_{ff} = \sqrt{3\pi/32G\rho}$). For comparison, an efficiency of 5% is a common choice in galaxy simulations. We also chose efficiencies to match those of Hopkins et al. (2011) for ease of comparison.

The full set of parameter choices for each simulation in the suite is listed in

Table 2.1: List of Simulations

name	n_{th} (cm^{-3})	c_*	$\epsilon_{\rm fb}$
n100.c25	100	25%	100%
n100.c6†	100	6%	100%
n100.c6.FB30	100	6%	30%
n100.c6.FB10	100	6%	10%
n100.c1.5	100	1.5%	100%
n100.c0.35	100	0.35%	100%
n300.c6	300	6%	100%
n1000.c6	1000	6%	100%

† The reference parameter set.

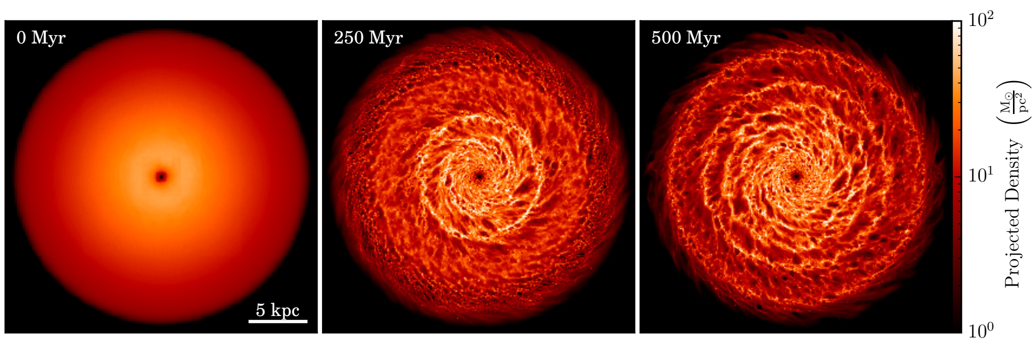

Figure 2.2: Surface density maps of the reference galaxy
Three surface density maps for the reference galaxy (n100.c6) at different times. *Left:* a snapshot of the initial condition from which each simulation is evolved. *Middle:* a snapshot at 250 Myr, halfway through the evolution of the galaxy. *Right:* a snapshot at 500 Myr, the point at which each simulation is stopped. The ring structures discussed in the text are clearly visible as the disk evolves. Each snapshot is 30 kpc across.

Table 2.1. The simulations are named following the convention n($n_{\rm th}$).c(c_*).(comments). The feedback efficiency is listed in the comments placeholder only if it deviates from our reference choice of 100%. For instance, our reference simulation with $n_{\rm th} = 100$ cm^{-3}, $c_* = 6\%$ and $\epsilon_{\rm fb} = 100\%$ is labelled n100.c6.

Figure 2.2 shows a density projection of our fiducial galaxy at three different times. By 500 Myr we see strong density ring features. As mentioned above, our model includes no old stellar disk. These rings are a side effect of the lack of gravity from this excluded component which would impose a dominant spiral potential if present. All of the galaxies in the suite exhibit these rings to a varying extent. Increasing or decreasing c_* increases or decreases the strength of the ring structures, respectively. This is similar to the behaviour for changes in feedback efficiency. When the efficiency of SNe is decreased to 10% (n100.c6.FB10), the prominent rings disappear.

2.3.2 The star formation rate

We begin by comparing the global Star Formation Rates (SFRs) for each simulation in the suite in Figure 2.3. Overall the rates are at the low end compared to nearby galaxies (e.g. Bigiel et al., 2008), even taking into account the quiet central region. We attribute this to the absence of an old stellar disk which causes a substantial reduction in the vertical gravity which would have decreased the scale height and increased the star formation rate. More specifically, the star formation models of Ostriker et al. (2010), as applied to THINGS disk galaxies, are heavily influenced by the old stellar disk and most new star formation occurs there. We defer examination of the role of an older stellar disk and associated spiral modes to future work. For now, this simpler picture is easier to interpret and compare to other isolated

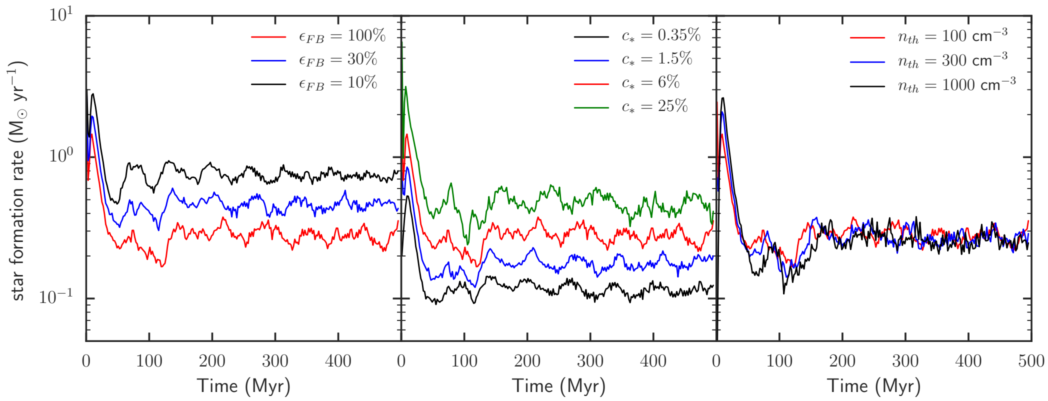

Figure 2.3: The global star formation rates for the suite of galaxies
The global star formation rates for our suite of galaxies. For each panel, the red line always denotes our fiducial galaxy. Left: the result of changing the feedback efficiency (ϵ_{fb}), holding all else constant. Middle: the result of changing the star formation efficiency (c_*). Right: the result of changing the density threshold (n_{th}). Raising the density threshold shows no accompanying change in the SFR, while raising either star formation or feedback efficiency causes sub-linear changes in the SFR (see text).

simulations of self-regulation.

There are a number of important features in the plots. First, is the scaling between the SFRs and changes in simulation parameters. The SFR is insensitive to a change in the threshold density required to form a star; changing the threshold by an order of magnitude does nothing to the global SFR. These findings are consistent with those of Hopkins et al. (2011), where changes in star formation parameters do not change SFRs in the Milky Way-type galaxy. Changes in threshold parameters are difficult to interpret in a global model as the density threshold is a parameter that impacts star formation on GMC scales.

The SFR is sensitive to efficiency-type parameters, specifically, those governing the star formation efficiency per dynamical time and the amount of feedback energy used. This sensitivity is not linear in the efficiency in either case, however. With respect to c_*, a change from 0.35% to 25%, a factor of 64 in efficiency, changes the star formation rate by a factor of 5 on average. In general, a change in c_* by a factor f_*, results in a change in the SFR by a factor of approximately $f_*^{0.3}$. With respect to $\epsilon_{\rm fb}$, a change from 10% to 100%, results in an increase in SFR by a factor of 2.5; in general a change in $f_{\rm fb}$, results in a change in the SFR by a factor of approximately $f_{\rm fb}^{0.4}$. All changes in the star formation rate are found to scale *sub-linearly* with changes to parameters. To better understand the origins of this scaling, we must consider the behaviour of the ISM.

Another characteristic feature is the oscillation in the rates. Specifically, although each of the rates settles to a fairly well-defined average, there is ongoing periodic variation about this equilibrium. Further, the frequency of this oscillation appears to be similar for all cases. This corresponding time-scale is approximately 75 Myr. This can be compared to the various time-scales important for the disk material. Firstly, there is the vertical oscillation time of the galaxy; in the Milky Way at the solar radius this time is 84 Myr (Binney & Tremaine, 2008). Due to the lack of old stars and associated surface density, the vertical oscillation time is longer at 220 Myr. Second, there is the time-scale over which star clusters deliver feedback. This feedback delivery time can cause bursts or ring structures in the disk at times when star formation itself is experiencing a burst. This occurs on a time-scale of approximately 40 Myr.

2.4 What holds up a galaxy?

In order to get an idea for what sets the star formation rate for a given galaxy, and better understand the scaling between this rate and other quantities we examine this behaviour within a pressure-driven framework for the regulation of star formation. We begin with equilibrium behaviour which is very similar to the vertical dynamical equilibrium portion of the framework developed by Ostriker et al. (2010) and Ostriker & Shetty (2011).

In the original pressure-driven framework, gas weight associated with vertical gravity is exactly matched by effective pressure support expected when star formation proceeds at a steady rate. Considering the weight of all disk components we arrive at an expression for the effective pressure *required* to maintain equilibrium:

$$\begin{aligned} \mathrm{P_R} &= \mathrm{P}_{dm} + \mathrm{P}_g + \mathrm{P}_* \\ &= \frac{1}{2}\Omega^2\Sigma_g\mathrm{H}_g + \frac{1}{2}\pi G\Sigma_\mathrm{g}^2 + \pi G\Sigma_g\Sigma_* \end{aligned} \tag{2.8}$$

where Ω is the shear rate, Σ_g is the gas surface density, H_g is the gas scale height and Σ_* is the stellar surface density. Detailed assumptions used in deriving these terms can be found in appendix A1.

Equation 2.8 indicates the level of pressure support required for the gas to avoid vertical collapse. In the galaxy support can come from sources which are linked to or independent of local star formation. Turbulence provides effective pressure where the original energy can come from galactic shear or stellar feedback processes. Thermal pressure, originating from UV radiation, photoelectric heating and dissipation of gas motions, can provide support. Sources of non-thermal pressure, such as magnetic fields and cosmic rays could also contribute. However, the scale height of cosmic rays is larger than that of the gas disk and so should not be a major factor. As noted above, in a simulation this translates to pressure support that is linked to local star formation (e.g. stellar feedback) or independent of local star formation (e.g. magnetic fields, cosmic rays, etc...). For the purposes of this study we consider only the support provided by turbulent or thermal pressure sources explicitly.

For small-scale contributions associated with stellar feedback, we do not specify the exact form that the pressure takes but refer to it simply as effective pressure associated with feedback, P_{fb}. For the purpose of providing support, the form is not important. Using our feedback model, it ultimately translates into thermal energy, u_{th}, on a fixed time-scale of 5 Myr as in Equation 2.4b . It can also push around gas, losing energy through PdV work and potentially increasing the effective turbulent support associated with vertical motions, v_z. In this work the pressure *support* we measure in the disk is calculated by:

$$\begin{aligned}
\mathrm{P}_{\mathrm{S}} &= \mathrm{P}_{th} + \mathrm{P}_{fb} + \mathrm{P}_{turb} \\
&= \frac{\Sigma_{\mathrm{g}}}{2\,H_g}\left(\frac{2}{3}u_{\mathrm{th}} + \frac{2}{3}u_{\mathrm{fb}} + v_z^2\right)_{z=0}.
\end{aligned} \tag{2.9}$$

This is the mid-plane support and all the quantities take on their mid-plane values. The mid-plane density, $\rho_{\mathrm{g},0}$, is well approximated by the gas surface density divided by twice the gas scale height, H_g.

2.4.1 Equilibrium behaviour in our simulated galaxies

Figure 2.4 shows the pressure contributions present for the reference galaxy in our suite (see section 2.3.1). The top panel in Figure 2.4 shows the effective pressure required to balance vertical gravity from dark matter (black), gas (green) and stars (orange). The bottom panel shows the pressure support provided by resolved turbulence (blue), thermal (purple) and feedback (red) energy. In both panels the dashed line is the total pressure as calculated by equation 2.8 and the dotted line is the total

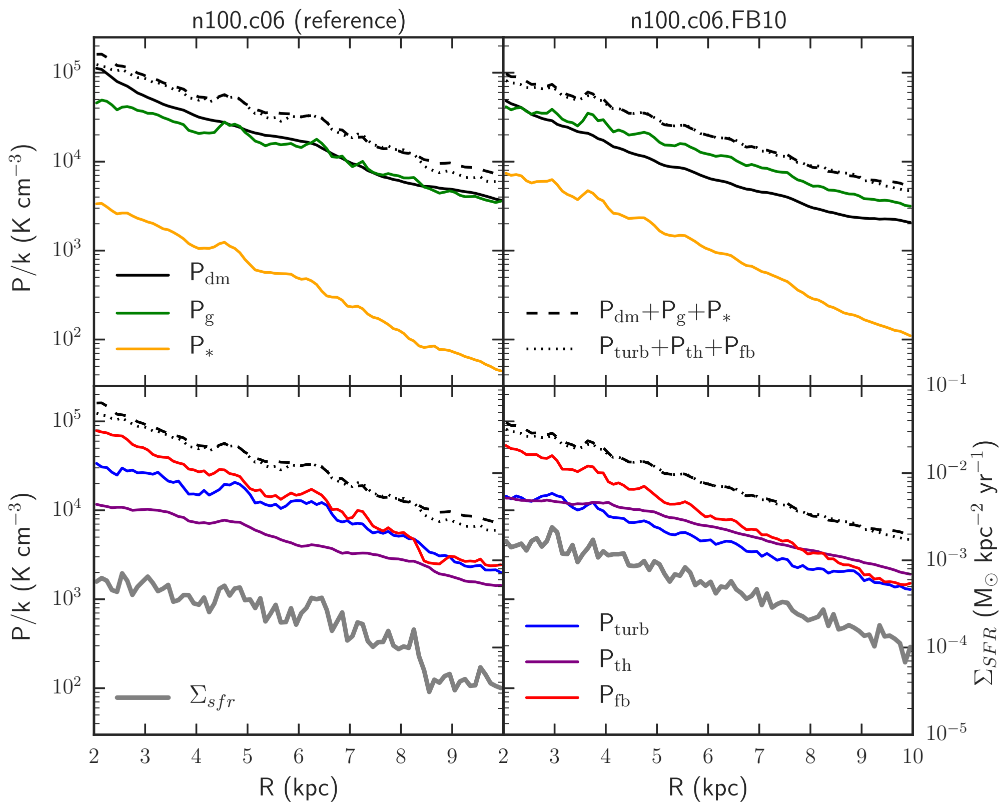

Figure 2.4: Average pressures for the reference galaxy
Left: average effective pressures for the reference simulation. *Right:* average effective pressures for the low feedback efficiency simulation (see Section 2.3.1 for details). The top panels show the effective pressure required to balance vertical gravity from the three components of the disk; dark matter (black), gas (green) and stars (orange). The bottom panels show the provided effective pressure support from turbulence (blue), thermal energy (purple) and feedback energy (red). The total pressure required to support vertical gravity (dashed line) is balanced by these effective pressure sources (dotted line). For comparison we also plot the SFR surface density (thick grey line, righthand scale). Each line shows an average over 100 Myr.

pressure as calculated by considering thermal and turbulent effective pressures (as in equation 2.9). Finally, the SFR surface density for each case is plotted in the bottom panels of Figure 2.4 (thick grey line). To facilitate a more direct comparison with the equilibrium models, we have smoothed in time, averaging over 100 Myr (from an output time of 400 to 500 Myr, to avoid early transients).

Referring again to Figure 2.4, the two lines denoting required and supplied support pressure in the disk agree in each case. This reflects the fact that on average the disk is in pressure equilibrium; star formation is regulated to balance vertical gravity requirements when averaged over long time periods. Similar agreement was seen in the simulations of Kim et al. (2011).

Due to the lack of an old stellar disk, the total stellar gravity contribution is minimal in our simulations. The young stellar population has a small scale height and the expression above is an upper-bound for this case. As noted previously, this is expected to make the effective pressure in our galaxy (and other similar simulations) lower than in typical nearby disk galaxies.

As mentioned above, we can use the time-averaged state of the galaxy to explore the equilibrium of the disk and how this can impact other galaxy properties. Since the pressure support in the disk is provided as a consequence of star formation, this must set the star formation rate. This equilibrium then must also be responsible for the sub-linear scaling between the star formation rate and star formation parameters.

In simulations, parameters are our tools to explore different types of galaxies. Different parameter combinations can cause different types of required pressure or pressure support to be dominant. When the feedback energy is high (100%), the scale height of the galaxy is much larger. This leads to a larger role for the vertical gravity from the dark matter component (see equation 2.24). In the top left panel of Figure 2.4 we see that at small radii the vertical gravity from dark matter does dominate the required pressure. At large radii there is an similar contribution from both dark matter and gas. Since the feedback energy is higher we also expect a large amount of the support to come from our feedback pressure ($\mathrm{P_{fb}}$). We see this in the bottom left panel of Figure 2.4. The pressure support provided by feedback is dominant in the inner regions of the disk, matched by support from turbulence in the outer regions of the disk.

Lowering the feedback energy (10%) leads to a change in the dynamics of the disk. Although the amount of star formation has increased, the total energy injected by those stars has decreased. The scale height decreases in response to the decrease in available energy and the gas component becomes the dominant source of vertical gravity (see eqn. 2.27). We also see that thermal energy plays a much larger role in setting the amount of pressure support although, at most radii, the feedback energy is still the dominant support term.

Although not shown here, similar trends exist when considering the star formation efficiency, c_*. Lowering the star formation efficiency creates similar results to lowering the feedback efficiency, both result in lowered energy injection rates when compared to the reference parameter set. This tells us that the injection rate of feedback energy is critical in setting the balance between pressure terms. A low star formation efficiency (e.g. 0.35% as in n100.c0.35) will produce the same behaviour in pressure terms that we see when lowering the feedback efficiency.

A key assumption in the Ostriker et al. (2010) model is the strong correlation between thermal pressure and the total effective pressure. In the Ostriker et al. (2010) model the contribution from FUV heating is important primarily because it sets the thermal pressure; the overall pressure (e.g. due contributions such as turbulence) is proportional to that with a multiplier of $\alpha = P_{tot}/P_{th} \sim 5$. This cor-

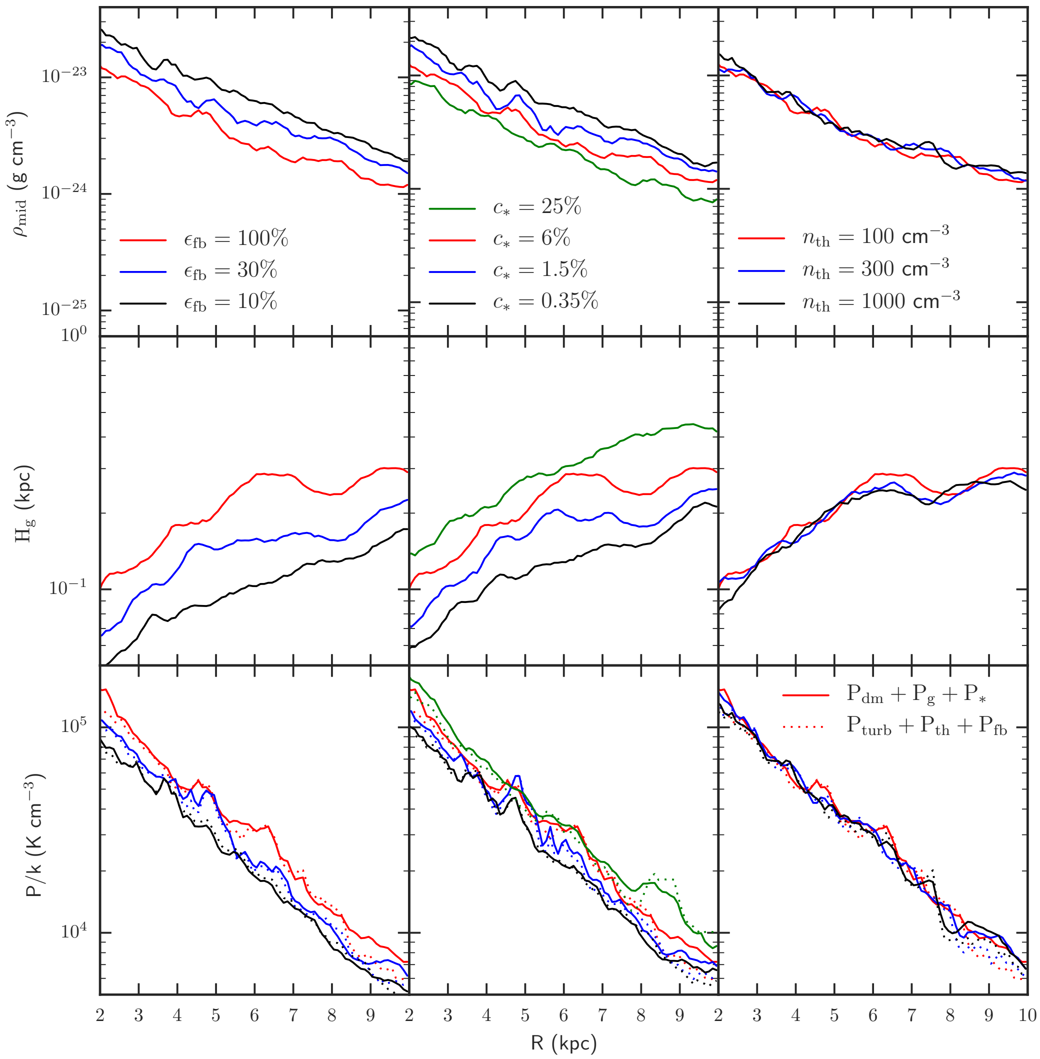

Figure 2.5: Summary of the three main galaxy regulation properties of interest Summary of the three main galaxy regulation properties of interest. Top row: the effective mid-plane density. Middle row: the scale height of the gas disk. Bottom row: the effective pressure. In this row dashed lines represent the total pressure support and solid lines represent the total pressure required.

relation has been confirmed directly in numerical simulations by Kim et al. (2011, 2013) and Kim & Ostriker (2015). Our results are consistent with this sub-dominant role for thermal pressure, as seen in Figure 2.4. Detailed studies of this partition would require high resolution local simulations (e.g. Kim & Ostriker, 2015).

A consequence of this strong correlation is the relationship between the SFR surface density and the total effective pressure. As seen in Figure 2.4 the SFR surface density changes in response to changes in the total effective pressure; the correlation is evident.

Figure 2.5 shows a sample of time-averaged galaxy properties. In all cases, the curves show quantities averaged over a span of 100 Myr (from a time of 400 to 500 Myr, see Figure 2.6). This is the same time span used to produce the average pressure quantities in Figure 2.4. The average properties change in response to changes in parameters and here we see similar behaviour to what we have already found in the global SFRs (see Figure 2.3).

What we can take away from this figure is that changes that impact global ISM properties are important to global regulation. For instance, we have previously seen that changes in density threshold do not result in changes to the SFR. In Figure 2.5 there are no changes to the mid-plane density, scale height or pressure as result of the change in threshold. The density threshold is a parameter that regulates star formation on the scale of GMCs, and so here does not play a role in changing global regulation. This is essentially the same result found by Hopkins et al. (2011).

Parameters which change the available energy *do* impact the global behaviour of the ISM. As shown, an increase in the feedback efficiency causes a corresponding increase in the scale height. A larger scale height increases the amount of pressure required. These together act to decrease the amount of star formation (as seen in Figure 2.3).

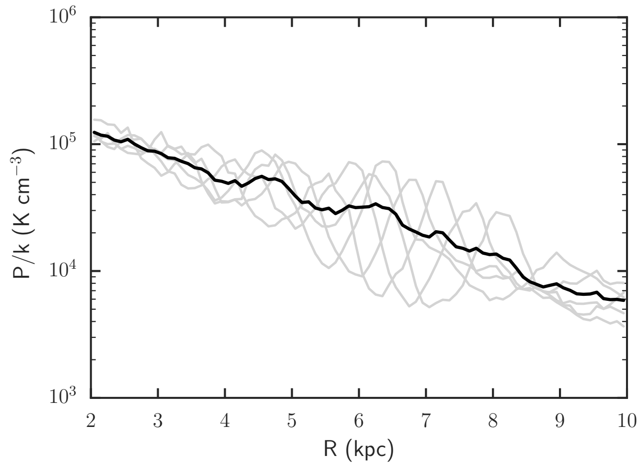

Figure 2.6: Variation of total pressure at different times for the reference galaxy Variation of total pressure at different times for the reference galaxy (n100.c6). The grey lines show the total pressure, as calculated using equation 2.9 at 25 Myr intervals between 400 and 500 Myr. The black line shows the average of the five times.

2.5 Time Variation

In the previous section we discussed our galaxies in a hydrostatic equilibrium framework. We now explore the time variability in our simulations. Figure 2.6 shows an example of the variability of the total pressure support for our reference galaxy (n100.c6). Plotted is the total pressure ($P_{\rm th} + P_{\rm fb} + P_{\rm turb}$) in radial bins. The grey lines show the pressure at specific timing points in 25 Myr intervals between 400 and 500 Myr, while the black line shows the average of these five times (as plotted in Figure 2.4). There is large variation in the five lines at various radii; disturbances move outward in the disk as time proceeds.

We now examine the time dependent response of a galaxy to changes in the star formation rate parameters. With all else fixed, the parameters cause instantaneous changes to the star formation rate. However, over time they also change the ISM. This response leads to net regulation. As noted in the introduction, star formation parameters represent tuneable knobs which can lead to different galactic structure and star formation behaviour. Ideally, they would be set through an understanding of the star formation process and the related constraint of producing a realistic ISM. Simulations typically only marginally resolve the ISM so this cannot be used as a constraint. Instead, gross properties such as the resulting star formation rate are used. The simulations examined here have sufficient resolution to probe key aspects of the ISM response.

In Figure 2.7 we plot three samples of local behaviour in the disk, one for our reference galaxy (n100.c6), one for our lowest feedback case (n100.c6.FB10) and one for a lower star formation efficiency (n100.c1.5). In these plots we have tracked a 100 pc wide annulus of the disk centred on a galactic radius of 4.5 kpc. Shown are the star formation rate (top), pressure support (second), pressure requirement from gravity (second), scale height (third) and gas surface density (bottom) for the three simulations mentioned above. We choose a radius of 4.5 kpc as substantial star formation occurs there and it is representative of the bulk of the star formation ongoing in the disk.

The first thing to note in these plots is that the behaviour of all of the quantities is periodic. For example, the characteristic period of the oscillations in the surface density is $\sim$ 90 Myr. This oscillation period is dependent on the galactic radius where the measurement is made. This period is seen in all three cases, regardless of the parameter choices.

Assuming pressure is driving the regulation of star formation, we expect a dynamic simulation to differ from the equilibrium Ostriker et al. (2010) picture. In the non-equilibrium case there will be lags in time before these responses are realized. In Figure 2.7 we can see the differing response times between star formation and the chosen quantities. These response times can be confirmed both visually and

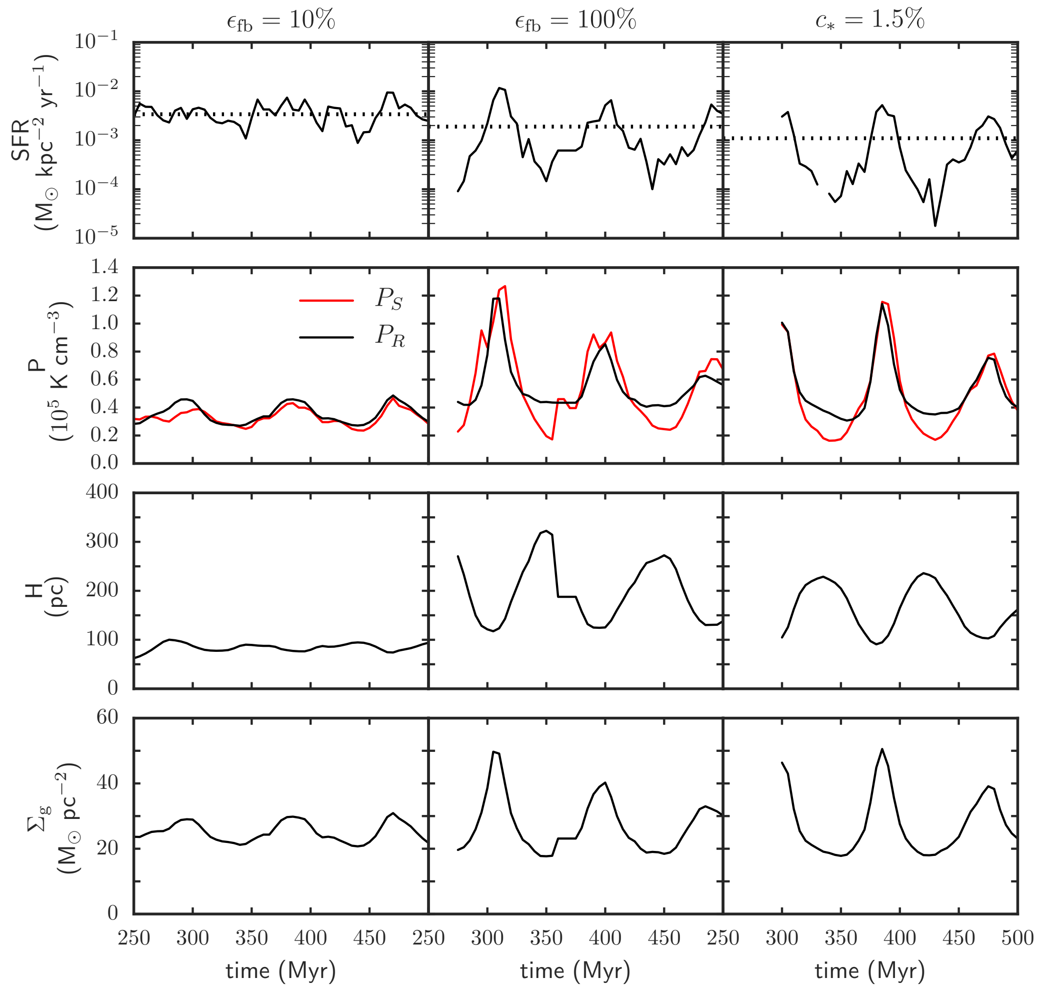

Figure 2.7: Local behaviour in an annulus

Local behaviour in an annulus of width 100 pc centered on a galactic radius of 4.55 kpc. *Left:* the behaviour of the ISM for the lowest feedback efficiency simulation (n100.c6.FB10). *Middle*: the behaviour for the reference galaxy (n100.c6). *Right:* the behaviour for a simulation with a lowered star formation efficiency (n100.c1.5). For a high feedback efficiency, the star formation rate shows clear bursts, this translates to large variations in other quantities. In contrast, for a lower feedback efficiency, a modest star formation rate can be maintained and this translates to a much smaller range of variation for other ISM quantities.

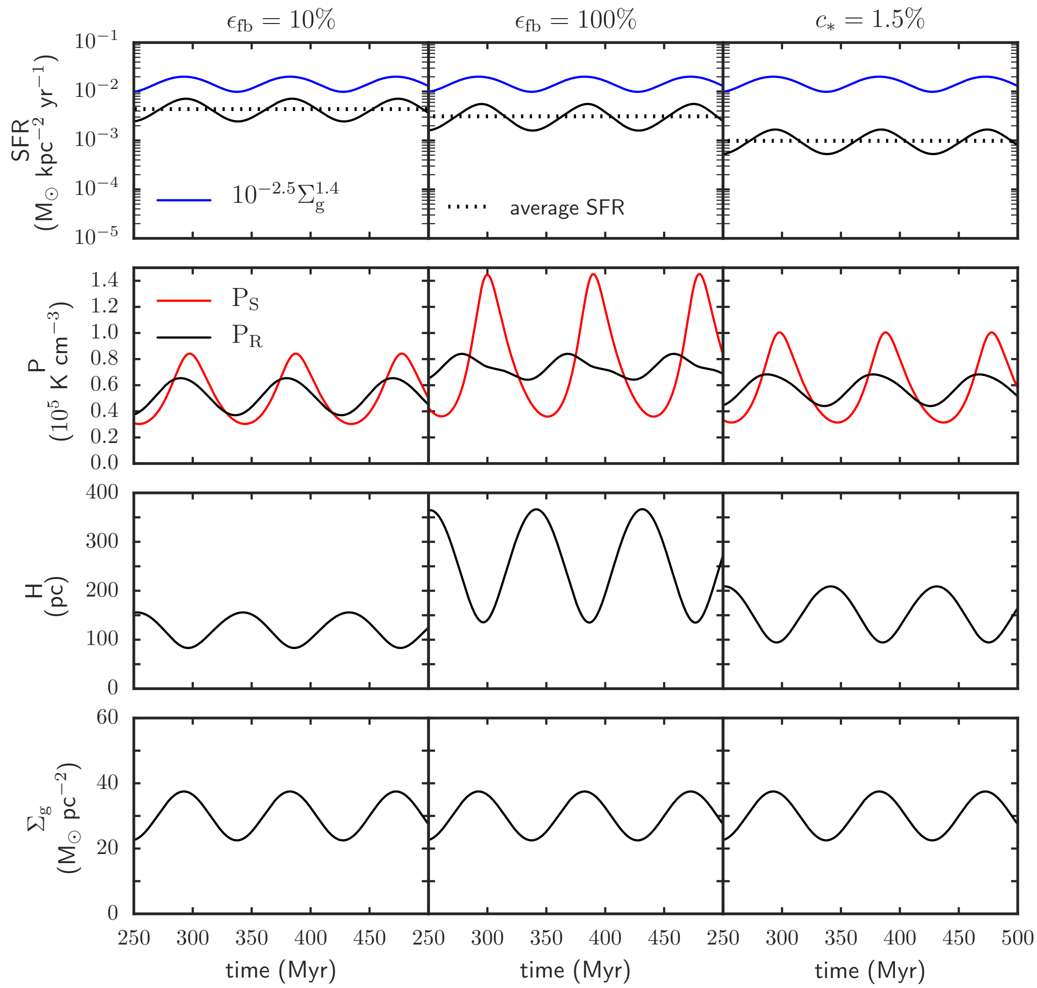

Figure 2.8: Results from our dynamic pressure driven model

Results from our dynamic pressure driven model. *Right:* a low feedback efficiency case, comparable to our simulation n100.c6.FB10. *Middle:* a high feedback efficiency case, comparable to our reference simulation n100.c6. *Left:* a low star formation efficiency case, comparable to our simulation n100.c1.5. Star formation rates are plotted in the top panels, where the black line shows the model rate, the blue line shows what is expected considering the Kennicutt-Schmidt relation (Kennicutt, 1998) and the dotted line denotes the average SFR.

through time signal analysis. In the following we refer specifically to the reference simulation (middle panels of Figure 2.7). Star formation is maximized at or just after a local peak in the mid-plane density or surface density when dense clouds are formed. The time between a peak in the local surface density and a local peak in star formation is $\sim$5 Myr (or less). Given that star formation is inefficient on the time-scales of these oscillations, the galaxy's main mechanism to decrease the star formation rate is to increase the scale height. An increase in the scale height implies that the mid-plane density of the gas is, on average, lower. This should lead to a decrease in the amount of star formation. As seen in Figure 2.7, the time after a local burst in star formation before the corresponding local maximum in the scale height is between 40 and 50 Myr: the galaxy cannot respond immediately to a change in the star formation rate.

It is more difficult to pick out similar response times in the lower feedback case. Decreasing the amount of available feedback energy changes the mode of star formation in the disk. In the middle panel of Figure 2.7, the star formation is very bursty; the events occur and then in between these the rate plummets effectively to zero. In contrast, when the feedback energy is lowered star formation can be sustained at a significant level for a longer period of time. In the top left panel, it is more difficult to pick out a clear periodic behaviour in the star formation rate, although it does still exist in the surface density. This corresponds to a smaller range of variation in the other ISM quantities as well. For example, when the feedback efficiency is high the scale height varies by approximately 200 pc between the minima and maxima of its cycle. When the feedback efficiency is lowered we see a variation of only approximately 50 pc.

Plotted in the right-most panel of Figure 2.7 is the result for a lowered star formation efficiency. Now, star formation events are more isolated in time and their intensity is decreased. Lowering the feedback efficiency is comparable to lowering the star formation efficiency. In each case, we have lowered the injection rate of feedback energy, just in different ways.

The dotted lines in Figure 2.7 denote the average SFR over the given time period. Here again we see similar sub-linear scaling between the average SFR and changes in parameters. In fact sub-linear scaling holds again for all quantities discussed. With this in mind we can now outline a general non-equilibrium framework to model the responses we see in our simulations.

2.6 A Dynamic Pressure-Driven Framework

The scale height of the gas may be defined as,

$$H_g = \frac{2}{\Sigma_{\rm g}} \int_0^\infty \rho_g z \, \mathrm{d}z. \tag{2.10}$$

The scale height changes in response to density waves moving in the plane of the disk as derived in appendix 2.7. An important property of waves is the lack of net motion which makes advection terms less important. This is precisely true for linear waves and in appendix A2 we show it holds for the disks simulated here.

This allows us to develop a local model of the galaxy. Using equation 2.42 from the appendix and neglecting the advection terms we have,

$$\frac{\partial H_g}{\partial t} = \bar{v}_z. \tag{2.11}$$

Thus the evolution of H_g is dominated by the mean vertical velocity in the half-plane,

$$\bar{v}_z = \frac{2}{\Sigma_{\rm g}} \int_0^\infty \rho_g v_z \, {\rm d}z. \tag{2.12}$$

In appendix A2 we show that the mean vertical velocity responds to differences between the mid-plane pressure and the total pressure required by gravity. Neglecting advection in equation 2.45 gives,

$$\frac{\partial \bar{v}_z}{\partial t} = \frac{2}{\Sigma_{\rm g}} \left({\rm P_S} - {\rm P_R} \right). \tag{2.13}$$

Thus the change in the mean vertical velocity depends on the difference between vertically integrated weight, which in section 2.4 we called the required pressure, $\rm P_R$, and the mid-plane supporting pressure, which we have denoted as, $\rm P_S$. These equations describe the dynamic pressure balance model. This model can incorporate the finite response time of the gas and inputs such as feedback that are distributed in time. We investigate this later in the Section.

To study the basic behaviour, we substitute in expressions for the pressures (i.e. eqn 2.8 and eqn. 2.9) We then get a time-dependent equation for the scale height,

$$\begin{aligned} \frac{\partial^2 H_g}{\partial t^2} &= \frac{2}{\Sigma_{\rm g}} \left({\rm P_S} - {\rm P_R} \right) \\ &= \frac{1}{H_g} (\gamma - 1) u_{\rm eff} - \Omega^2 H_g - \pi G \Sigma_{\rm g} - \frac{2\pi G \Sigma_* H_g}{H_g + H_*}, \end{aligned} \tag{2.14}$$

where we have bundled the pressure support terms in a single effective internal energy, $u_{\rm eff}$ with an effective γ. When $\rm P_S = P_R$ we recover the equilibrium solution. Thus, when the left-hand side is zero, we have an equation for the mean scale height, $\overline{H}_g$. We can examine oscillations about the mean using a small perturbation in height, $\Delta H_g = H_g - \overline{H}_g$, and retaining terms of order ΔH_g,

$$\frac{\partial^2 \Delta H_g}{\partial t^2} = -\left(\frac{1}{\gamma}\frac{c_{\text{eff}}^2}{\overline{H}_g^2} + \Omega^2 + \frac{2\pi G \Sigma_* H_*}{(\overline{H}_g + H_*)^2}\right)\Delta H_g, \tag{2.15}$$

where we have rewritten u_{eff} in terms of the associated effective sound speed, c_{eff}.

Because increasing scale height simultaneously lowers the mid-plane pressure while increasing the vertical gravity, the opposing pressure terms act together to stiffen the restoring force relative to that experienced by collisionless components. The characteristic gas vertical oscillation frequency, Ω_g, is thus given by

$$\Omega_g^2 = \frac{1}{\gamma}\frac{c_{\text{eff}}^2}{\overline{H}_g^2} + \Omega^2 + \frac{2\pi G \Sigma_* H_*}{(\overline{H}_g + H_*)^2}, \tag{2.16}$$

and is indirectly dependent on the gas surface density, Σ_g, through the mean scale height. Even when $\Sigma_g \ll \Sigma_*$, galactic gas disks tend to evolve to states where self-gravity is relevant so the mean height varies strongly with Σ_g. One would expect the oscillation frequency to fall between the collisionless vertical oscillation frequency and the effective vertical crossing frequency. However, because the terms in eqn. 2.16 all become additive, the frequency is lower than both of those expected.

In present-day spiral galaxies, the vertical gravity near the mid-plane is dominated by the old stellar population. This increases the collisionless vertical oscillation frequency without otherwise qualitatively changing the behaviour as the vertical gravity associated with the dark matter and the stellar disk have a similar form, roughly linear with height, z. The effective equation of states leaves $\gamma \sim 1$ for cases with modest feedback. For example, at 4.5 kpc in our simulations as shown in

Figure 2.7, the collisionless vertical oscillation period, $\frac{2\pi}{\Omega}$ = 130 Myr, whereas the time-scale for vertical gas oscillations can be as low as $\frac{2\pi}{\Omega_g}$ = 30-60 Myr depending on the mean support.

The gas is not oscillating freely, but is responding to the drivers of changes in the surface density. The period of the density waves is largely independent of the vertical response of the gas. In our simulations, the oscillations in surface density occur on characteristic time-scales of 90 Myr, as shown in Figure 2.7 and also in the time variation in the star formation rates in Figure 2.3. Thus the vertical motions are not particularly close to resonance. The primary effect is a small time lag in the minima of the scale height with respect to crests in gas column. The gas frequency indicates the time-scale $\approx \frac{1}{\Omega_g} \sim 10$ Myr for the scale height to respond to a change in conditions.

In the case of present-day disk galaxies the density waves are strongly decoupled from the gas response because the waves are dominated by the old stellar disk which is typically an order of magnitude more massive than the gas disk. This will change the characteristic frequencies of both the waves and vertical motions so that a more resonant response may be possible.

The local effective support can change substantially with strong stellar feedback in response to star formation. Feedback energy in any form increases the effective sound speed and causes the scale height to jump in response. This is particularly apparent in the middle panels of Figure 2.7, corresponding to 100% feedback efficiency and a reasonable star formation rate. In this case the pressure terms get substantially out of balance, leading to strong oscillations in the scale height. The ability of the dynamic pressure model to explain the behaviour of our simulated galaxy disks is explored in the next section.

2.6.1 Model with star formation

The non-equilibrium model from the previous section captures large scale vertical motions of the disk well, but small scale physics such as star formation is a challenge. To compare to the simulations we make three simple additions to the model. Firstly, we apply some modest damping to the vertical oscillation on a timescale comparable to the gas crossing time to mimic shocks and other kinetic energy losses,

$$\frac{\partial \bar{v}_z}{\partial t} = \frac{2}{\Sigma_\mathrm{g}} \left(\mathrm{P_S} - \mathrm{P_R}\right) - \bar{v}_z/\tau_\mathrm{D}, \tag{2.17}$$

where τ_D was set to 20 Myr for all the results shown here. Factors of two variation in this parameter moderately change the range of the scale height variation but do not strongly affect the star formation rate, for example.

Secondly, we need to model star formation. We elected to use a Schmidt Law similar to that employed in the simulations. The star formation surface density is thus,

$$\dot{\Sigma}_* = c_* f_\mathrm{DENS} \sqrt{G\,\rho_g}\Sigma_\mathrm{g}. \tag{2.18}$$

The density is estimated from the gas column $\rho_g = \frac{1}{2}\Sigma_\mathrm{g}/H_g$. The primary change over the simulation sub-grid model is a correction to estimate the fraction of the gas which is in cold clouds and is thus eligible for star formation. We used a fixed factor of $f_\mathrm{DENS} = 0.1$ for all cases. It is generally difficult to estimate the detailed density structure. This limits our ability to use this model to study the simulations where we varied the star formation density threshold. The parameter c_* is effectively equivalent to that used in the simulations.

Finally, we need to include stellar feedback. The simple feedback model employed in the simulation readily lends itself to inclusion in a simple model. Just as in the simulations, 10^{49} ergs per solar mass of new stars is applied over a period of 40 Myr and removed on a time-scale of $\tau = 5$ Myr. The energy per unit area, E_{fb}, changes as follows,

$$\dot{E}_{fb} = \epsilon_{\rm FB} 10^{49} {\rm erg\, M_\odot^{-1}}\, \dot{\Sigma}_* - \frac{E_{fb}}{\tau}. \tag{2.19}$$

The parameter, $\epsilon_{\rm FB}$ is identical to that used in the simulations. The mid-plane internal energy is given by $u_{fb} = \frac{1}{2} E_{fb}/H_g/\rho_g$.

To summarize, in our time dependent model, effective pressure support can come from two components. The first is a fixed contribution, that could be attributed to thermal and turbulence from large-scale shear. The second pressure component varies with the amount of star formation and encompasses supernovae and radiative feedbacks. In actuality, turbulence arises from many sources and can be strongly correlated with feedback. However, this is very difficult to characterize within a simple model. Turbulence could be modelled as a form of feedback with a locally variable characteristic decay time-scale. In this simple model we use a constant decay time. The non-cooling feedback energy is open to interpretation and could include turbulence.

2.6.2 Model results

In Figure 2.8 we show our results for the local model with three parameter choices: a high feedback case (corresponding to our reference parameter set), a low feedback case (corresponding to n100.c6.FB10) and a low star formation efficiency case (corresponding to n100.c1.5). This can be compared directly with Figure 2.7. The

Table 2.2: Comparison of the average SFR in annuli at $R = 4.5$ kpc for the simulation and our model

		varying $\epsilon_{\rm fb}$	
name	ϵ_{fb}	$\overline{\rm SFR}$ ($M_\odot$ kpc^{-2} yr^{-1})	model $\overline{\rm SFR}$ ($M_\odot$ kpc^{-2} yr^{-1})
n100.c6†	100%	0.0018	0.0031
n100.c6.FB30	30%	0.0026	0.0038
n100.c6.FB10	10%	0.0034	0.0044
		varying c_*	
name	c_*	$\overline{\rm SFR}$ ($M_\odot$ kpc^{-2} yr^{-1})	model $\overline{\rm SFR}$ ($M_\odot$ kpc^{-2} yr^{-1})
n100.c25	25%	0.0021	0.0097
n100.c6†	6%	0.0018	0.0031
n100.c1.5	1.5%	0.0011	0.00098
n100.c0.35	0.35%	0.00052	0.00027

† The reference parameter set.

results for the full parameter set are summarized in Table 2.2. We also include averages from the simulations in Table 2.2. We stress that the relative changes in the model SFRs versus the simulation SFRs should be compared, rather than the specific values.

Note that in creating the three model cases, the *only* parameters changed in the model were the feedback and star formation efficiency. The similarity with Figure 2.7 is striking. The local model exhibits the same time variation seen in the simulations. Vertical motions are driven by pressure imbalances. The slight lag between star formation peaks and pressure increases that is difficult to distinguish from noise in three-dimensional simulations is now far more apparent.

The match is not perfect, as should be expected, given the simple local model. The star formation model was kept very basic, avoiding the temptation of introducing tuneable parameters. A more complex model could be developed but is not necessary to explain the behaviour. This model works best for large scale effects such as feedback (e.g. varying $\epsilon_{\rm fb}$). The inherent small-scale nature of star formation makes it harder to model in the basic framework, particularly non-linear parameters such as thresholds for star formation. For this reason, we did not attempt to introduce star formation thresholds into the local model. As a result, the star formation varies more smoothly in the model than it does in the three-dimensional simulations.

The effect of changing the feedback efficiency is shown in the middle- and left-hand panels of Figure 2.8. A change in feedback efficiency by a factor of 10 increased the star formation by a factor of $\sim$2.5 in the entire simulated disk. At a radius of 4.5 kpc, as shown in Figure 2.7, that difference is $\sim$ 1.8 times. In the simple model, a similar sub-linear scaling emerges: the same change in parameters produces a change in star formation of $\sim$1.5 times.

The local model is more sensitive to the star formation efficiency (c_*) than are the simulations. In the simulations, at a radius of 4.5 kpc, decreasing the star formation efficiency by a factor of 4 decreases the amount of star formation by $\sim$ 1.6 times. As shown in Figure 2.8 (and Table 2.2) decreasing the star formation efficiency by a factor of 4 in the model decreases the star formation rate by $\sim$3.1 times. This is a stronger scaling than we see in our actual simulations (closer to linear). As noted earlier, star formation rates depend on ISM properties and small scale structure in a highly non-linear manner that is hard to mimic without resorting to a more complex model. This can be seen in the more peaked behaviour of the simulation star formation rates in Figure 2.7. Despite these issues the qualitative behaviour is quite similar.

The simple model is able to reproduce the relative relationships between different pressure support and requirement terms. For our 100% feedback efficiency case we saw an equal contribution to the required pressure from either the dark matter of gas component. The pressure requirement then became dominated by the gas term at lower feedback efficiency (10%). Similarly, at high efficiency the largest support came from the pressure due to feedback, with an increased role for the fixed component (which represents thermal and turbulent energy) as the efficiency is decreased.

We have over-plotted the expected star formation rate from the Kennicutt-Schmidt relation in the top panels of Figure 2.8 for reference. Just as for the simulations, the model star formation rates are lower than this, which we attribute to the lack of an old stellar disk. As the relation only depends on gas surface density, it is the same in each case. The different model parameters lead to different outcomes, however. Even in this simple model, there is plenty of freedom to adjust the parameters to improve the agreement and this calibration process is a common step for most simulation codes. However, most codes employ even more complex models and there is no guarantee that achieving a match to the relation creates a more realistic simulation overall. This is particularly true given that most codes are calibrated to isolated models.

The observed Kennicutt-Schmidt relation has considerable vertical scatter. Models such as this can be used to explore the origins of this. Both the vertical structure and the star formation rate depend on many factors, such as the stellar surface density, the rotation curve, the two-phase nature of the ISM and so forth. This was explored for local galaxies by Ostriker et al. (2010).

2.6.3 The origin of sub-linear scaling

For the cases shown in Figure 2.8 here we have assumed an oscillating surface density. Using a constant surface density decreases the average star formation rate and scale height by $\sim$10%. Holding the surface density constant causes the height oscillations to damp away. We reach an equilibrium where the required pressure equals the supporting pressure. This is equivalent to the equilibrium model of Ostriker et al. (2010). Thus in terms of averaged quantities, an equilibrium model is sufficient.

Setting $P_{\rm R} - P_{\rm S} = 0$ as in the right-hand side of equation 2.14 and keeping only those terms relevant to these simulations gives

$$\frac{1}{H_g}(\gamma - 1)(u_{\rm fb} + u_{\rm other}) - \Omega^2 H_g - \pi G \Sigma_{\rm g} = 0. \tag{2.20}$$

With our assumed Schmidt law (equation 2.18) and the simple feedback model (equation 2.19), the equilibrium feedback energy is,

$$u_{\rm fb} = \frac{\sqrt{G}}{2}\, \tau\, c_*\, f_{\rm DENS}\, \epsilon_{\rm fb}\, (10^{49}{\rm erg\,M_\odot^{-1}})\, \Sigma_{\rm g}^{1/2}\, H_g^{-1/2}. \tag{2.21}$$

When this is substituted into equation 2.20, the result is a non-linear equation for H_g. The solution for the mean scale height is within 10% of the average of H_g in figure 2.7. As is clear from equation 2.21, c_* and $\epsilon_{\rm fb}$ affect the scale height in the same way. The is exactly true in the local model and approximately true in the full simulations. The non-linear dependence of H_g on these quantities is the reason for the non-linear scaling seen in the simulations.

For parameter values in the region of interest, the scale height depends on c_* and $\epsilon_{\rm fb}$ roughly as $H_g \sim c_*^{0.4}\epsilon_{\rm fb}^{0.4}$. The star formation rate differs from the energy expression by one power in c_* and changes as $H_g^{-1/2}$. Thus the star formation rate depends on these parameters roughly as $\dot{\Sigma}_* \sim c_*^{0.8}\,\epsilon_{\rm fb}^{-0.2}$. This is essentially what we see in the local model. These particular power-laws are specific to this radius and local model parameters. However, similar sub-linear behaviour will occur generally.

2.7 Summary and Conclusions

We have presented a suite of high resolution isolated galaxies that include a purposefully simple feedback scheme. We use a wide range of parameter choices to explore both the implications of these choices and the process of regulation of star formation. We find a sub-linear scaling between parameter choices and the resulting amount of star formation. This is found in many other simulations (see, e.g. Hopkins et al., 2011). We adapted the equilibrium pressure regulation models of Ostriker et al. (2010) and Kim et al. (2011, 2013) to include representative simulation sub-grid recipes for star formation and feedback. This allowed us to demonstrate the origin of the sub-linear scaling with these parameters. The equilibrium models readily explain how feedback affects the star formation rates. The effect of changing the overall star formation efficiency is also well represented by the models, however, strongly non-linear parameters, such as star formation density thresholds, are harder to incorporate. Such parameters also reflect the complexity of star-formation and how difficult it is to model even in three-dimensional simulations.

The simulations show regular variations in the local star formation rates and other properties. These are driven by density waves which occur naturally in global models. In comparison, small box simulations (e.g. Kim et al., 2013) are expected to approach rough equilibrium and do not need to consider vertical oscillations. We extended the equilibrium models into a dynamic pressure-driven regulation framework. We show that advection plays a minor role and thus the vertical motions are driven by local effective pressure differences. We adapt the star formation and feedback models used in the simulations to produce a complete local model of star formation and feedback. These models are able to qualitatively reproduce the behaviour of our simulated galaxies, including the variability and the sub-linear scaling with the star formation and feedback efficiency parameters.

A goal of this work was to determine which aspects of the small-scale star formation physics strongly affect larger scale simulations. The simulation community has invested in a diverse array of feedback prescriptions and types. We demonstrate that the crucial factor is how feedback translates into effective pressure support on larger scales. It is the effective pressure support that regulates star formation and the vertical structure of the ISM. Realistic regulated star formation thus requires that the scale height be resolved.

Variable FUV backgrounds are a potentially important stellar feedback for normal spiral galaxies. Including this variability is feasible in local boxes (Kim et al., 2013) but is numerically challenging in global galaxy simulations. In future work, we plan to explore this mode of feedback using newly developed radiative transfer techniques (Woods et al., in preparation) including an old stellar disk. The inclusion of FUV that is coupled to star formation allows self-consistent measurement of the partition between different pressure components (Kim & Ostriker, 2015; Koda et al., 2016).

Acknowledgements

The authors thank the referee, Chang-Goo Kim, for a detailed report that greatly improved the paper. The authors thank Elizabeth Tasker, Alex Pettitt and Diederik Kruijssen for helpful discussions. The authors thank SHARCNET (Shared Hierarchical Academic Research Computing Network), SciNet, and Compute/Calcul Canada, who provided dedicated resources to run these simulations. Computations were performed on the gpc supercomputer at the SciNet HPC Consortium. SciNet is funded by: the Canada Foundation for Innovation under the auspices of

Compute Canada; the Government of Ontario; Ontario Research Fund - Research Excellence; and the University of Toronto. Data visualization was performed using the yt[1] toolkit by Turk et al. (2011). This work was supported by NSERC. SMB acknowledges financial support from the Vanier Canada Graduate Scholarship program.

A1 Pressure Terms

In the pressure driven regulation framework of Ostriker et al. (2010), gas weight set through vertical gravity creates a pressure requirement in the ISM that must be matched by some type of pressure support. We begin by examining the components of the galaxy that contribute to vertical gravity, namely dark matter, gas and stars. These add linearly to give a required mid-plane pressure,

$$P = \int_0^\infty \rho g \, \mathrm{d}z,$$

where ρ_g is the gas density and g is the total gravity. The contribution to the gravity from dark matter, which is taken here to include all spherically symmetric large-scale components of the galaxy, is directly related to galactic rotation and can be estimated near the disk as,

$$g_{\rm dm} = \Omega^2 z, \tag{2.22}$$

where Ω is the angular rotation rate. Then the pressure required for support against gravity from the dark matter component is

$$P_{\rm dm} = \int_0^\infty \rho_g g_{\rm dm} \, \mathrm{d}z \tag{2.23}$$

[1] http://yt-project.org

$$= \frac{1}{2}\Omega^2 H_g \Sigma_{\rm g}, \tag{2.24}$$

where H_g and Σ_g are the scale height and surface density of the gas, respectively.

Gravitational acceleration due to planar, disk material is given by,

$$g = 2\pi G\Sigma(z), \tag{2.25}$$

where $\Sigma(z)$ is the disk surface density within a height, z, of the mid-plane. Thus the pressure required for support against self-gravity from the gas in the disk is,

$$P_{\rm g} = \int_0^\infty \rho_g g_{\rm g}\, {\rm d}z \tag{2.26}$$

$$= \frac{1}{2}\pi G\Sigma_{\rm g}^2, \tag{2.27}$$

where now $\Sigma_{\rm g}$ denotes the total gas surface density.

Similarly, the expression for stellar gravity is,

$$g_* = 2\pi G\Sigma_*(z), \tag{2.28}$$

where $\Sigma_{\rm g}(z)$ is the gas surface density at a given height above the mid-plane. The pressure required for support against stellar gravity is,

$$P_* = \int_0^\infty \rho_g g_*\, {\rm d}z. \tag{2.29}$$

A solution for the pressure needed to balance the stellar component requires an assumption for the functional form of the gas and stellar densities. We assume the following form,

$$\rho_g = \rho_{g,0}\mathrm{e}^{-z/H_g} \tag{2.30}$$

$$\rho_* = \rho_{*,0}\mathrm{e}^{-z/H_*}. \tag{2.31}$$

Then an expression for the stellar surface density is

$$\Sigma_*(z) = 2\int_0^z \rho_* \mathrm{d}z \tag{2.32}$$

$$= \Sigma_*\left(1 - \mathrm{e}^{-z/H_*}\right), \tag{2.33}$$

where H_* is the stellar scale height, and $\rho_{g,0}$ and $\rho_{*,0}$ are the initial gas and stellar densities, respectively. Finally, the required pressure support for the stellar component is

$$\begin{aligned} P_* &= 2\pi G \int_0^\infty \rho_g \Sigma_*(z)\,\mathrm{d}z \qquad (2.34)\\ &= 2\pi G \Sigma_* \rho_{g,0} \int_0^\infty \mathrm{e}^{-z/H_g} - \mathrm{e}^{-z\left(\frac{1}{H_g}+\frac{1}{H_*}\right)}\mathrm{d}z \\ &= 2\pi G \Sigma_* \rho_{g,0} H_g \left[1 - \left(\frac{H_g}{H_g} + \frac{H_g}{H_*}\right)^{-1}\right] \\ P_* &= \pi G \Sigma_* \Sigma_g \left(\frac{H_g}{H_g + H_*}\right), \qquad (2.35) \end{aligned}$$

If we assume the stellar scale height H_* is small, as is appropriate for a very young stellar population, we get an upper bound on the stellar contribution to the total pressure, $P_* = \pi G \Sigma_* \Sigma_g$. As shown in section 2.4, the net contribution of stellar gravity in initially star-free, isolated disk tests such as the ones employed here is small.

In the case that the scale height of the stars is large, as in the case of an old stellar disk, the surface density associated with stars approaches a linear function of height, $\Sigma_* \approx 2\rho_{*,0}\, z$ as used in Ostriker et al. (2010), where $\rho_{*,0}$ is the mid-plane stellar density. Then the required pressure is approximately $P_* \approx 2\pi G \Sigma_g H_g \rho_{*,0}$ which matches 2.35 for the case when $H_g \ll H_*$.

A2 Dynamic Pressure Balance

Assuming symmetry about the $z = 0$ plane, the scale height of the gas may be defined:

$$H_g = \frac{\int_0^\infty \rho_g z \,\mathrm{d}z}{\int_0^\infty \rho_g \,\mathrm{d}z} = \frac{2}{\Sigma_\mathrm{g}} \int_0^\infty \rho_g z \,\mathrm{d}z, \tag{2.36}$$

The scale height changes in response to changes in conditions, in particular the gas column, Σ_g. The change in the gas column with time is dominated by density waves moving solely in the plane of the disk,

$$\frac{\partial \Sigma_\mathrm{g}}{\partial t} = -\vec{v}_{R\phi} \cdot \nabla \Sigma_\mathrm{g} - \Sigma_\mathrm{g} \nabla \cdot \vec{v}_{R\phi}, \tag{2.37}$$

where $\vec{v}_{R\phi}$ denotes motions in the plane that are assumed to be independent of z. This allows us to take planar velocity terms out of the integrals where necessary.

For linear waves, the advection term (first on the right in equation 2.37) is second order and negligible compared to the second term associated with compressive waves. In a non-linear disk scenario, fractional variations in Σ_g can be order unity, but the evolution of the gas column is still dominated by compressive rather than material waves and individual gas elements travel through the wave crests

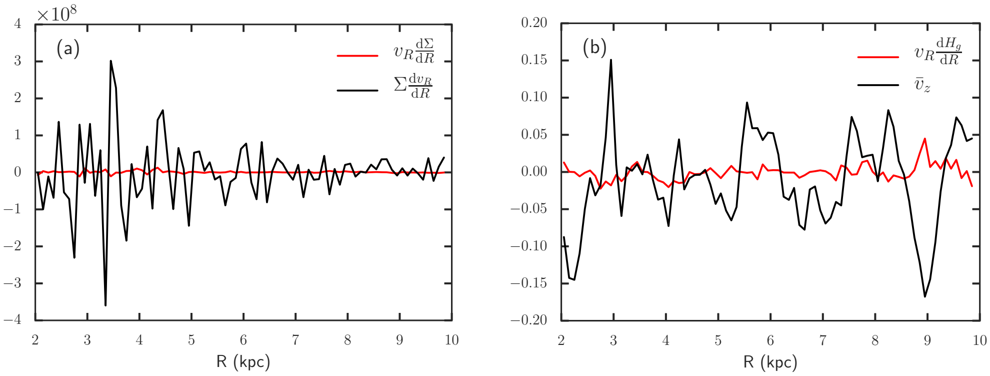

Figure 2.9: A comparison of the planar advection
Left: Planar advection vs. compression term in the rate of change of gas column.
Right: Planar advection vs. vertical motion term in the rate of change of scale height. In both cases the contribution of advection in the plane is small.

rather than with them. This is demonstrated to be the case for the simulations used here in Figure 2.9(a).

H_g changes over time due to the movement of gas both in the plane and vertically,

$$\frac{\partial H_g}{\partial t} = -\frac{H_g}{\Sigma_{\rm g}}\frac{\partial \Sigma_{\rm g}}{\partial t} + \frac{2}{\Sigma_{\rm g}}\int_0^\infty \frac{\partial(\rho_g z)}{\partial t}\,\mathrm{d}z. \tag{2.38}$$

The second term can rewritten using the conservation of mass,

$$\frac{2}{\Sigma_{\rm g}}\int_0^\infty \frac{\partial(\rho_g z)}{\partial t}\,\mathrm{d}z = \frac{2}{\Sigma_{\rm g}}\int_0^\infty \frac{\partial \rho_g}{\partial t}\; z\,\mathrm{d}z$$
$$= -\frac{2}{\Sigma_{\rm g}}\int_0^\infty \left(\nabla\cdot(\rho_g \vec{v}_{R\phi}) + \frac{\partial(\rho_g v_z)}{\partial z}\right)\; z\,\mathrm{d}z, \tag{2.39}$$

where the gradient, ∇, is used here to represent the gradient in the two planar directions (R and ϕ) only. The divergence term in the planar velocity can be broken into two parts,

$$
\begin{aligned}
&\frac{2}{\Sigma_{\rm g}} \int_0^\infty \nabla \cdot (\rho_g \vec{v}_{R\phi})\, z \,\mathrm{d}z \\
&= \frac{2}{\Sigma_{\rm g}} \int_0^\infty \vec{v}_{R\phi} \cdot \nabla(\rho_g z)\,\mathrm{d}z + \frac{2}{\Sigma_{\rm g}} \int_0^\infty (\rho_g z) \nabla \cdot \vec{v}_{R\phi}\,\mathrm{d}z \\
&= \vec{v}_{R\phi} \cdot \nabla H_g + \frac{H_g}{\Sigma_{\rm g}} \vec{v}_{R\phi} \cdot \nabla \Sigma_{\rm g} + \frac{2\,H_g}{\Sigma_{\rm g}} \nabla \cdot \vec{v}_{R\phi} \\
&= \vec{v}_{R\phi} \cdot \nabla H_g - \frac{H_g}{\Sigma_{\rm g}} \frac{\partial \Sigma_{\rm g}}{\partial t},
\end{aligned} \tag{2.40}
$$

where the last line makes use of equation 2.37.

The vertical mass flux term from 2.39 simplifies as follows,

$$
\frac{2}{\Sigma_{\rm g}} \int_0^\infty -\frac{\partial(\rho_g v_z)}{\partial z}\, z \,\mathrm{d}z = \frac{2}{\Sigma_{\rm g}} \int_0^\infty \rho_g v_z \,\mathrm{d}z = \bar{v}_z, \tag{2.41}
$$

using integration by parts and symmetry about the $z = 0$ plane. This term is the mass weighted mean vertical velocity in the half-plane, which we will denote by, $\bar{v}_z$.

Combining terms, we get a simple planar advection term for H_g plus changes due to vertical motions in the form of $\bar{v}_z$. Thus the comoving rate of change of the scale height is,

$$
\frac{dH_g}{dt} = \frac{\partial H_g}{\partial t} + \vec{v}_{R\phi} \cdot \nabla H_g = \bar{v}_z. \tag{2.42}
$$

As H_g is a ratio of density-weighted integrals, there is no equivalent of the compressive term for the gas column. As with the gas column, we expect the advection term to play a minor role so that changes in H_g are dominated by the mean vertical velocity. This is precisely true in the frame of fluid elements moving within the disk and passing through density waves. We show this is true at fixed points in our simulations in figure 2.9(b), confirming the unimportance of advection terms.

The rate of change of the mean vertical velocity is given by,

$$\frac{\partial \bar{v}_z}{\partial t} = -\frac{\bar{v}_z}{\Sigma_\mathrm{g}}\frac{\partial \Sigma_\mathrm{g}}{\partial t} + \frac{2}{\Sigma_\mathrm{g}}\int_0^\infty \frac{\partial(\rho_g v_z)}{\partial t}\,\mathrm{d}z. \tag{2.43}$$

Using the momentum conservation equation we can write,

$$\begin{aligned}&\frac{2}{\Sigma_\mathrm{g}}\int_0^\infty \frac{\partial(\rho_g v_z)}{\partial t}\,\mathrm{d}z \\ &= \frac{2}{\Sigma_\mathrm{g}}\int_0^\infty \left(-\nabla\cdot(\rho_g \vec{v}_{R\phi}) - \frac{\partial(\rho_g v_z^2)}{\partial z} - \frac{\partial \mathrm{P}}{\partial z} + \rho_g g\right)\,\mathrm{d}z,\end{aligned} \tag{2.44}$$

where $P(z)$ denotes the pressure and $g(z)$ is the vertical gravitational acceleration. Just as for the scale height, the sole remaining term from the $\partial\Sigma_\mathrm{g}/\partial t$ terms and the planar velocity terms is a term for the advection of $\bar{v}_z$. As a result we can express the comoving rate of change of the vertical velocity as,

$$\begin{aligned}\frac{d\bar{v}_z}{dt} &= \frac{\partial \bar{v}_z}{\partial t} + \vec{v}_{R\phi}\cdot\nabla\bar{v}_z \\ &= \frac{2}{\Sigma_\mathrm{g}}\left(\rho_g v_z^2\big|_0^\infty - \mathrm{P}\big|_0^\infty + \int_0^\infty \rho_g g\,\mathrm{d}z\right) \\ &= \frac{2}{\Sigma_\mathrm{g}}\left(\mathrm{P_S} - \mathrm{P_R}\right).\end{aligned} \tag{2.45}$$

Thus the change in the mean vertical velocity depends on the difference between the vertically integrated weight or required pressure, $\mathrm{P_R}$ and the mid-plane supporting pressure, $\mathrm{P_S}$. These pressures were defined in section 2.4 and their individual components calculated in appendix A1. These equations describe the dynamic pressure balance model.

As discussed above, planar advection is unimportant for density waves in the disk. Thus we can use the comoving and partial time derivative interchangeably for H_g and $\bar{v}_z$.

Bibliography

Agertz O., Kravtsov A. V., 2015, ApJ, 804, 18

Agertz O., Kravtsov A. V., Leitner S. N., Gnedin N. Y., 2013, ApJ, 770, 25

Benincasa S. M., Tasker E. J., Pudritz R. E., Wadsley J., 2013, ApJ, 776, 202

Bigiel F., Leroy A., Walter F., Brinks E., de Blok W. J. G., Madore B., Thornley M. D., 2008, AJ, 136, 2846

Binney J., Tremaine S., 2008, Galactic Dynamics: Second Edition. Princeton University Press

Chabrier G., 2003, PASP, 115, 763

Creasey P., Theuns T., Bower R. G., 2013, MNRAS, 429, 1922

Dalcanton J. J., et al., 2012, ApJS, 200, 18

de Avillez M. A., Breitschwerdt D., 2005, A&A, 436, 585

Dobbs C. L., 2008, MNRAS, 391, 844

Dobbs C. L., Burkert A., Pringle J. E., 2011, MNRAS, 417, 1318

Elmegreen B. G., Parravano A., 1994, ApJ, 435, L121

Hopkins P. F., Quataert E., Murray N., 2011, MNRAS, 417, 950

Hopkins P. F., Quataert E., Murray N., 2012, MNRAS, 421, 3488

Joung M. R., Mac Low M.-M., Bryan G. L., 2009, ApJ, 704, 137

Keller B. W., Wadsley J., Benincasa S. M., Couchman H. M. P., 2014, MNRAS, 442, 3013

Kennicutt Jr. R. C., 1998, ApJ, 498, 541

Kim C.-G., Ostriker E. C., 2015, ApJ, 815, 67

Kim C.-G., Kim W.-T., Ostriker E. C., 2011, ApJ, 743, 25

Kim C.-G., Ostriker E. C., Kim W.-T., 2013, ApJ, 776, 1

Koda J., Scoville N., Heyer M., 2016, ApJ, 823, 76

Kruijssen J. M. D., Longmore S. N., 2014, MNRAS, 439, 3239

Krumholz M. R., Tan J. C., 2007, ApJ, 654, 304

Krumholz M. R., McKee C. F., Tumlinson J., 2009, ApJ, 699, 850

McNally C. P., Wadsley J., Couchman H. M. P., 2009, ApJ, 697, L162

Ostriker E. C., Shetty R., 2011, ApJ, 731, 41

Ostriker E. C., McKee C. F., Leroy A. K., 2010, ApJ, 721, 975

Price D. J., Federrath C., 2010, MNRAS, 406, 1659

Renaud F., et al., 2013, MNRAS, 436, 1836

Schaye J., 2004, ApJ, 609, 667

Schinnerer E., et al., 2013, ApJ, 779, 42

Stinson G., Seth A., Katz N., Wadsley J., Governato F., Quinn T., 2006, MNRAS, 373, 1074

Tasker E. J., 2011, ApJ, 730, 11

Tasker E. J., Tan J. C., 2009, ApJ, 700, 358

Tielens A. G. G. M., 2005, The Physics and Chemistry of the Interstellar Medium

Turk M. J., Smith B. D., Oishi J. S., Skory S., Skillman S. W., Abel T., Norman M. L., 2011, ApJS, 192, 9

Wadsley J. W., Stadel J., Quinn T., 2004, New Astron., 9, 137

Walter F., Brinks E., de Blok W. J. G., Bigiel F., Kennicutt Jr. R. C., Thornley M. D., Leroy A., 2008, AJ, 136, 2563

Ward R. L., Benincasa S. M., Wadsley J., Sills A., Couchman H. M. P., 2016, MNRAS, 455, 920

Wolfire M. G., McKee C. F., Hollenbach D., Tielens A. G. G. M., 2003, ApJ, 587, 278

Chapter 3

A tale of two clump masses: a new way to study clump formation in numerical simulations

S. M. Benincasa, J. W. Wadsley, H. M. P. Couchman, A. R. Pettitt, and E. J. Tasker

This article has been submitted to The Monthly Notices of the Royal Astronomical Society.

Abstract

We present a new method to study the characteristic scales of collapse and fragmentation in galactic disks. Clump formation is seeded in simulations via controlled perturbations with a specified wavelength and velocity. These are applied to otherwise quiet gas disks ranging from analogues of present day spirals to gas-rich, high-redshift galaxies. The results are compared to linear theory, turbulently perturbed disks and observations. The results reflect the expectations of linear, non-axisymmetric theory with a finite window for growth into a bound clump. We identify two new modes of clump formation: rotation-driven fission and fragmentation of tidal tails, though both are expected to rarely contribute to clump formation in observed disks. We find that bound clumps are generally much smaller than the so-called Toomre mass. The preferred scale for fragmentation increases with the disk gas mass but cannot produce bound objects larger than $\sim 10^9$ M$_\odot$. The most likely bound clump mass increases from 3×10^6 in low mass disks up to 5×10^8 M$_\odot$. We conclude that observed massive stellar and gaseous clumps on 1 kpc scales at high redshift are most likely aggregates of many initially distinct bound clumps.

3.1 Introduction

The typical size of star clusters must, to some degree, be dependent on the galactic environment. This dependence can manifest itself in different ways. The Jeans' mass, which changes based on environment, plays a role (e.g. Hopkins, 2012). The pressure likely plays a role; high pressure environments such as Arp 220 have larger star clusters when compared to other local galaxies (e.g. Wilson et al., 2006). If we begin by considering low redshift galaxies, a preferred mass-scale for star cluster formation is apparent. In the Milky Way itself, star clusters have typical masses between $10^3 - 10^4$ $M_\odot$ (Fall & Chandar, 2012). A preferred scale for star clusters may in turn suggest a preferred scale for Giant Molecular Clouds (GMCs). In the Milky Way GMCs have typical masses between $10^5 - 10^6$ $M_\odot$ and typical sizes of 50 - 100 pc (Fukui & Kawamura, 2010; McKee & Ostriker, 2007).

If we consider galaxies at higher redshifts, these preferred scales appear to change. Stellar observations are able to identify large UV-bright star-forming regions called *clumps* (Elmegreen et al., 2007). The CANDELS survey has provided extensive clump catalogues for galaxies between 0.5 $< z <$ 3.5. The properties of clumps identified in CANDELS galaxies suggest they are extremely large, with typical masses of $10^7 - 10^9$ $M_\odot$ and typical sizes ~ 1 kpc (Guo et al., 2015, 2018). Other compilation studies find masses between $10^5 - 10^9$ $M_\odot$ (Dessauges-Zavadsky & Adamo, 2018). Either way, these are orders of magnitude more massive than present-day clusters or star-forming regions.

This picture is even more complex if we add in starbursts or merger-driven systems. As mentioned above, if we consider Arp 220, there are many active sites of star formation and the star-forming complexes may be much larger than those in the Milky Way (Murray et al., 2010, and references therein). In these environments the masses of stellar clusters increase dramatically. Wilson et al. (2006) find masses approaching 10^7 $M_\odot$, which may make them candidates for young globular clusters.

The conditions in star-forming regions should be imprinted in the properties of gas. At higher redshifts, and in starburst systems, the conditions both within and around galaxies were different than at low redshift. Specifically, at higher redshifts the galaxy interaction rate was higher and galaxies themselves are much more likely to be gas rich.

It is no surprise that in such gas-rich, highly molecular environments the properties of star-forming regions are likely to be different. Indeed, the appearance of gas disks beyond z$\sim$0.5 are much more clumpy in nature (e.g. Förster Schreiber et al., 2009). This highly molecular clumpy nature may suggest that star-forming regions may be larger in both mass and spatial extent. Wide beam observational studies suggest these objects have masses between 10^8 - 10^{10} $M_\odot$, or approximately $1 - 10\%$ of the total disk mass (e.g. Tacconi et al., 2010; Swinbank et al., 2010, 2011; Genzel et al., 2011; Hodge et al., 2012). The corresponding physical sizes range from as small as 100 pc to as large as 2 kpc (e.g. Swinbank et al., 2010; Tacconi et al., 2010).

However, recent results from the SGASS lensing survey have shown a finer level of substructure, albeit in galaxies less massive than those typical in the CANDELS sample (Johnson et al., 2017a). These results show that stellar clump sizes can be consistent with present-day star clusters, which would originate from objects similar to present day GMCs with high star formation efficiency (Johnson et al., 2017b; Rigby et al., 2017). Another such lensing study has been done in the Cosmic Snake (Cava et al., 2018). Using data from the CLASH survey, the authors have obtained both a lensed arc and counterimage. In this way they can compare two spatial resolutions for the same object. They find that the lower resolution image (counterimage) produces clumps that are amplified by a factor of 2-5 on average, for a decrease in resolution of 10 times. Studies like these suggest two important points. First, the gas mass of a galaxy is important for determining the scale of star formation. Second, the resolution of earlier studies may not be sufficient to resolve clumps.

With the typical physical resolution of instruments at high redshift being generally poorer, it may be that we are treating collections of GMCs (Tacconi et al., 2010) as a single entity. This idea has been lent credence by samples of lensed galaxies: while directly observed galaxies are often large due to selection effects, lensed galaxies are typically of lower mass ($M_\star \sim 10^9$ $M_\odot$). They provide us with a better resolved picture of the molecular gas. For example, Swinbank et al. (2010) find gas clumps of similar size to Milky Way GMCs, approximately 100 pc. They propose that these objects would be similar to present-day star-forming regions except with more star-forming cores with higher densities. Hodge et al. (2012) infer typical internal densities of $\sim$ 100 cm^{-3}, in accordance with the typical density of low-redshift GMCs. If we infer masses from these sizes, we can assume that these objects would likely have masses similar to large present-day GMCs: maybe between $10^5 - 10^7$ $M_\odot$. Local starburst galaxies with enhanced star formation and kinematic properties similar to galaxies at z $\sim$ 1.5 can also be used as a testbed for these theories. Their proximity offers better resolution studies and HST-DYNAMO has studied 13 such galaxies (White et al., 2017). Studies here confirm that clump clustering is likely to impact the measurement of clump properties at higher redshifts, where resolution degrades (Fisher et al., 2017).

If we look to isolated galaxy simulations, we see results consistent with small star-forming regions. For example, Tamburello et al. (2015) find smaller clump masses ($< 10^7$ $M_\odot$). The higher resolution available in isolated galaxy simulations also offers the perfect place to study the impacts of resolution on structure identification. Some work has suggested that the resolution of HST at the redshifts concerned is insufficient to fully resolve these clumpy objects. Tamburello et al. (2017) and Dessauges-Zavadsky et al. (2017) have argued that at the spatial resolution of 1 kpc, it is not possible to fully resolve these stellar clumps. This supports the idea that we are just seeing collections of smaller stellar clumps, clustered closely together. Indeed, Behrendt et al. (2016) have shown that closely clustered clumps could be confused for more massive objects with the resolution of surveys like CANDELS.

At the other extreme, it has been suggested that in massive, gas-rich galaxies the physics of clump formation changes with Violent Disk instabilities (VDI) producing different outcomes (Dekel et al., 2009). This idea has been invoked to explain certain cosmological zoom simulations exhibiting larger clumps in the range 10^{7-9} $M_{\odot}$ (Mandelker et al., 2014, 2017). However, it has been theorized that not all gas rich disks host VDI, and that this behaviour is largely dependent on feedback strength rather than a qualitative difference in how clumps form (Fiacconi et al., 2017). Regardless, other studies of cosmological zoom simulations also report clump masses in this higher range (Agertz et al., 2009; Oklopčić et al., 2017). These larger clumps masses are seen not just in cosmological simulations, but in isolated galaxy simulations as well (Hopkins et al., 2012; Bournaud et al., 2014).

When comparing all of this data, we are faced with a seemingly inescapable difficulty. All of the studies discussed previously involve different methods. Some involve simulations on cosmological scales while others model isolated galaxies and the resolution of these two types of simulations can be quite different. Different studies use different numerical methods or different hydrodynamical schemes. Beyond that, perhaps the largest variable, is the type of feedback chosen. The type and strength of feedback chosen plays a large role in determining the structure of star-forming gas and, consequently, the structure of stellar clusters. All of these variables makes it incredibly confusing to compare results among different studies. Add on top of that the different types of observations we are considering, stellar versus gas, lensed versus un-lensed, and we are left with great difficulty in interpreting the results in the literature.

We propose a new method to study clump formation in simulations. Our method avoids the problems associated with many of the algorithm-specific assumptions discussed above. We seed clump formation events by hand and study their growth in high-resolution isothermal disks that do not include feedback. In this way, we can constrain the initial mass of clumps formed in a variety of disks. These are directly comparable to both observationally determined masses and masses from theories of fragmentation.

The rest of the paper is laid out as follows. We begin by examining the predictions from linear theory in section 3.2. Linear theory is difficult to extrapolate to non-linear clump properties. Instead, we use it to design simulations to explore clump formation in disks ranging from Milky Way-like cases to the heavy, turbulent disks expected at high redshifts. In section 3.3, we describe our controlled simulation approach which allows for high resolution and relatively easy interpretation of the results. We make first use of this in section 3.4, looking at isolated, turbulent disks. In order to study the key scales for fragmentation and clump formation in a controlled way, we take a new approach of seeding non-linear perturbations. We present details of the approach and results in section 3.5. In section 3.6, we extrapolate from our simulation results to estimate likely clump masses based on disk conditions. Finally, in section 3.7 we discuss the observational implications of this study.

3.2 Theoretical Expectations

While galactic disks are complex systems they are still amenable to theoretical analysis. The classic analysis by Toomre (1964) assumed a razor-thin, axisymmetric system. This analysis applies in the case where the perturbations are effectively rings or very tightly wound (highly localized). In this case the dispersion relation has three main terms,

$$\omega^2 = \kappa^2 - 2\pi G\Sigma|k| + {c_s}^2 k^2. \tag{3.1}$$

The terms representing rotation (the epicycle frequency, κ) and pressure (the sound speed, c_s) act to stabilize the perturbations against gravity (Newtonian constant G) due to the underlying surface density Σ. As the physical scale, given by the wavenumber k, changes from large (k ∼0) to small, we transition from being stabilized by rotation to sound waves or pressure; a stabilized regime is one in which the oscillation frequency, $\omega^2 > 0$. A key physical scale is the Toomre length,

$$\lambda_{\rm Toomre} = \frac{4\pi^2 G\Sigma}{\kappa^2}. \tag{3.2}$$

Beyond this scale all perturbations are stabilized by shear (rotation). This sets a hard upper limit on the mass of clumps collapsing directly from a single perturbation. This can be translated into a mass, the Toomre mass, by assuming intrinsically circular collapsing regions,

$$M_{\rm Toomre} = \pi \left(\frac{\lambda_{\rm crit}}{2}\right)^2 \Sigma. \tag{3.3}$$

This mass is sometimes used an initial mass for clumps (Reina-Campos & Kruijssen, 2017; Kruijssen, 2012). However, this is somewhat ad hoc given that the linear dispersion relation applies to plane waves which would collapse to filaments or rings in the case of axisymmetric global perturbations. So linear, axisymmetric theory is, at best, a rough guide.

At intermediate scales, $\lambda \sim \lambda_{\rm Toomre}/2$, gravity is at its most effective and ω can be imaginary (unstable) if the Toomre Q parameter is less than one.

$$Q = \frac{c_s \kappa}{\pi G \Sigma} < 1. \tag{3.4}$$

The aforementioned violent disk instabilities are effectively non-linear Toomre instabilties. Thus the Toomre Q parameter should be a guide to locations where gas and stellar clumps can form (Inoue et al., 2016). It has been suggested that galaxies should be unstable in this mode until z~1-0.5 (Cacciato et al., 2012).

There are several complicating factors with applying these results directly to galactic disks. The first is that real disks are not razor thin. The primary impact is that disks can have Q as low as $\sim 2/3$ without being unstable to axisymmetric modes depending on how thick the disk is (Romeo & Wiegert, 2011). Secondly, galaxies are comprised of both gas and stars which act together and affect each other's individual stability (Goldreich & Lynden-Bell, 1965a; Romeo et al., 2010; Agertz & Kravtsov, 2015). Another limiting complication is that the linear theory is a local approximation and does not apply for structures that are comparable in size to the disk.

A key feature of these linear modes is that the growth rate is independent of both the amplitude and time so that for $\omega^2 < 0$ they are predicted to grow indefinitely so that finite disturbances may result. In other words, perturbations can grow indefinitely without being sheared apart.

A less commonly considered factor is the assumption of axisymmetry or tight winding. It is widely recognized that disks grow large-scale perturbations (e.g. spiral structure) for supposedly stable Q-values in the range of 1-2. Secondly, the structures that grow are not axisymmetric. Axisymmetry greatly simplifies the dynamics as such perturbations do not elongate due to shear. Local non-axisymmetric perturbations including the role of shear were examined by Goldreich & Lynden-Bell (1965b). In this case, the behaviour of plane waves does not simplify to a quadratic dispersion relation and even linear waves must be integrated as differential equations. Here we present the evolution equation for small amplitude surface density perturbations in the form given by Jog (1992), and simplified for the case of a single gaseous component,

$$\left(\frac{d^2\theta}{d\tau^2}\right) - \left(\frac{d\theta}{d\tau}\right)\left(\frac{2\tau}{1+\tau^2}\right) = \frac{-\theta}{4A^2}\left[\kappa^2 + \frac{8AB}{1+\tau^2} - 2\pi G\Sigma k_y\sqrt{1+\tau^2} + c_s^2 k_y^2(1+\tau^2)\right], \quad (3.5)$$

where $\theta = \delta\Sigma/\Sigma$ is the fractional perturbation to the gas surface density, $\tau = 2At - k_x/k_y$ is a dimensionless time (such that the perturbation is radial at $\tau = 0$), Σ is the unperturbed surface density, κ is the epicycle frequency, A and B are the Oort constants, (k_x, k_y) is the wavevector, and c_s is the gas sound speed.

The terms in the square brackets are directly analogous to the terms in the axi-symmetric dispersion relation, Eqn. 3.1, and reduce to it in the appropriate limit. The first two terms represent shear and rotation but with an added time dependence associated with the instantaneous orientation of the wavefront. The latter terms depend on the instantaneous wavenumber which is sheared and thus minimized near $\tau = 0$. The pressure term always dominates for very early and late times.

Thus the behaviour of these linearized equations (in θ) is such that growth occurs briefly near $\tau \sim 0$ as the waves transition from leading to trailing, as noted by Goldreich & Lynden-Bell (1965b) and Jog (1992). The behaviour is oscillatory for other times. This means that the net growth is limited. Thus to achieve interesting outcomes from a relatively quiet start we must have multiple cycles of growth enabled by non-linear (e.g. wave to wave) interactions that reform leading waves. Put another way, to achieve bound structures we must start with substantial perturbations and grow these.

In the vigorously star forming disks of interest, we have feedback and turbulence to provide non-linear perturbations. For example, individual superbubbles sweep up material on kpc scales. Interactions of many feedback events are expected to result in a turbulent velocity spectrum over a range of scales up to of order the disk scale height. Structure in the disk, such as pre-existing spiral modes, can also extract energy from the disk rotation to power turbulence on scales similar to the spiral waves themselves; this is comparable to the disk size for very unstable disks. Thus we would argue from the theory that the growth of finite, non-linear perturbations is a consistent picture of the development of bound clumps.

3.3 Simulation Methods and Disk Models

Astrophysical simulations always struggle to resolve the turbulent cascade and small scale structures developed through the coupling of turbulence and thermal instabilities. Taken from a broad perspective, however, turbulence behaves similarly to a polytropic gas. For this work, we have used isolated disks with an isothermal equation of state which is very simple to model relative to the full complexities of small scale turbulence. However, it directly provides the effective support we require of the turbulence and simultaneously provides a simple, straightforward model for the cooling losses. The effective equation of state of the ISM is complex but broadly similar to an isothermal one. In particular, Goldreich & Lynden-Bell (1965b) show that for equations of state with polytopic index $\gamma \sim 1$, non-linear unstable clumps will remain unstable and continue to collapse. Thus with this choice we can have confidence regarding the future fate of collapsing regions.

All of the disk simulations presented here use a static, logarithmic halo potential (Binney & Tremaine, 2008) to represent the background of the dark matter halo, bulge and old stellar disk. This provides a well defined rotation curve (i.e. $\kappa(r)$). There is a small adjustment to this rotation curve due to the gas component. The gas surface density is exponential with a scale length of 5 kpc from 2 to 12 kpc with a smooth tailing off to zero below 2 kpc and beyond 12 kpc. Combined with a constant sound speed, this generates a Toomre Q that varies slowly in the active region from 2 to 12 kpc with a minimum value at ~ 5 kpc, and with values exceeding twice the minimum below 2 kpc and beyond 12 kpc.

We use the modern smoothed particle hydrodynamics code GASOLINE (Wadsley et al., 2004, 2017) to simulate the gas component, including self-gravity with a softening length of 10 pc. We have experimented with applying a Jeans floor that increases the effective pressure where the Jeans length is unresolved (following Robertson & Kravtsov, 2008). However, we find that for the simulations discussed here this makes no difference to the amount of fragmentation. We do not directly apply a star formation or feedback model as these contain subgrid prescriptions that are code dependent. Additionally, there is still debate regarding the importance of different types of feedback (Murray et al., 2010; Hopkins et al., 2012).

We have built three disk models for this work and their properties are summarized in Table 3.1. These models cover a range of galaxy masses quoted in the literature: from a Milky Way sized galaxy to a galaxy that is massive enough to

Table 3.1: The three main disk initial conditions discussed in this work.

name	c_s	T	mass	Σ_g(R $= 5$ kpc)	$Q_{\min}$
cold disk	5.16 km/s	2 500 K	6.95 $\times 10^9$ $M_\odot$	22 $M_\odot$/pc^2	1.07
warm disk	14.59 km/s	20 000 K	1.96 $\times 10^{10}$ $M_\odot$	61.6 $M_\odot$/pc^2	1.15
hot disk	35.75 km/s	120 000 K	5.56 $\times 10^{10}$ $M_\odot$	176 $M_\odot$/pc^2	1.1
name	λ_{crit}	M_{Toomre}			
cold disk	960 pc	1.5 $\times 10^7$ $M_\odot$			
warm disk	2.4 kpc	2.9 $\times 10^8$ $M_\odot$			
hot disk	5.4 kpc	4.1 $\times 10^9$ $M_\odot$			

evolve into a present-day elliptical.

The first is modelled after a Milky Way-type disk, analogous to a less massive high redshift object (which we have labelled cold). It has a total gas mass of 6.95×10^9 $M_\odot$ and we use 5.56 million particles. The gas sound speed is 5 km/s, with a gas particle mass of 1250 $M_\odot$. These smaller mass objects are more typical of lensed samples, as here we are just sampling the galaxy luminosity function.

For the second disk (warm) we have modelled a more massive disk, which is a closer comparison to a high redshift turbulent, gas-rich disk. This case has a total gas mass of 1.96×10^{10} $M_\odot$. Here the gas sound speed is increased to 14 km/s to mimic the larger amount of turbulence present in high redshift galaxies (Förster Schreiber et al., 2009). To leave the effective resolution and Q parameter the same we then increase the gas particle mass to 3535 $M_\odot$.

Finally, the third disk (hot) is the most massive and warmest of the three. This case has a total gas mass of 5.56×10^{10} $M_\odot$. The gas sound speed is raised to 40 km/s. Again, to leave the effective resolution the same this results in a gas particle mass of 10^4 $M_\odot$. Galaxies in this higher mass range are more comparable to samples like that of Guo et al. (2018) for example. These galaxies which are already this massive at high redshift will likely become massive ellipticals by the present day.

Since we are interested in triggering clump formation, the surface density profiles chosen are such that the initial Toomre Q parameter lies near the border line of stability. We choose 5 kpc as the galactic radius of interest, where Q is at a minimum. At 5 kpc, the cold disk has an initial Q_{min} of 1.07, the warm disk has an initial Q_{min} of 1.15, and the hot disk has an initial Q_{min} of 1.1. The target value of Q was 1.1 but the effects of self gravity of the gas disk made it hard to get a precise Q, particularly for heavier disks.

For reference, a razor-thin disk stable to axisymmetric, linear perturbations has Q above 1. In other tests, not reported here, we find that for values above $Q \sim 1.3$, it is difficult for even fairly large perturbations to push regions toward gravitational instability. Since high-z galaxies have substantial inflows, we expect that they will always evolve to a point with Q between 1 and 1.3 so that clumps can form.

The Truelove criterion states that in a finite-difference code four cells are needed to resolve the Jean's length accurately (Truelove et al., 1997). A similar criterion exists in SPH simulations, where we require that the Jean's mass be greater than the neighbour number multiplied by the particle mass (Bate & Burkert, 1997). We are able to resolve the Jean's mass up to 100 cm^{-3} in all of our disks, and up to 10^5 cm^{-3} two of our three disks. The disk in question is the coldest disk. We have resimulated higher resolution cases for a subset of our disks. In these cases we increase the resolution by splitting each gas particle eight times. In these high resolution cases we find no changes to the fragmentation or clump mass.

3.4 Turbulent Disk Simulations

We begin by studying how turbulence can drive clump formation using full turbulent disk simulations. To create these cases, the entire disk is overlaid with a turbulent spectrum in a manner similar to Price & Federrath (2010). We applied a Burgers' turbulent spectrum (k^{-4}) with a peak scale of 2 kpc to the initially quiet disks from Section 3.3. There is no stellar feedback to sustain the turbulence so it decays over a few crossing times. Results at time 40 Myr are shown in the left column of Figure 3.1, which is slightly more than twice the shear time (κ^{-1}). These disks are clearly visually clumpy, but we require a more quantitative measurement.

3.4.1 Measuring Clump Masses

For cases that are able to produce a clump structure, we must be able to assign a mass to these objects. We use two different approaches to assign clump masses. To study clump masses in manner similar to radio frequency observations (e.g. Colombo et al., 2014), we use the package astrodendro (Rosolowsky et al., 2008) to identify massive, dense structures in our simulations. As a second approach we use SKID (Spline Kernel Interpolative Denmax)[1] to identify bound objects in our simulations. We have chosen to identify "clumps", which could be the progenitors to star clusters, as bound objects. SKID is able to identify groups of bound gas particles and so is perfect for this purpose.

3.4.1.1 Finding clump masses with Astrodendro

The package astrodendro uses dendrogram trees to identify related structures. Dendrograms are particularly useful for identifying objects embedded in larger hier-

[1] https://github.com/N-BodyShop/skid

archical structures, in a way that requires limited parameter choices (Rosolowsky et al., 2008; Colombo et al., 2015).

In order to pass data through the astrodendro package we convert all of our data into synthetic FITS files. For this conversion we use the method of Ward et al. (2012), wherein particles are mapped into pixels and then smeared using the SPH smoothing kernel. To make the identification more straightforward we zoom in on a region surrounding the clump, with a width of 1 kpc. For this analysis we use pixel sizes of 10 pc. At this time we do not make any attempt to map the gas to CO emission, and instead use the surface density.

The only parameter we set in astrodendro is a minimum value required for a pixel to be considered part of the tree. We have experimented with other parameters (mindelta, minnpix), but find that at our resolution they make little difference. We experiment with two thresholds for the tree. The first is a surface density of 100 $M_{\odot}/pc^2$, above which we can estimate that star formation would proceed. This is close to the extinction threshold of Lada et al. (2010). The second is a surface density of 10 $M_{\odot}/pc^2$, above which gas transitions to being mostly molecular (Bigiel et al., 2008). We find that this threshold makes little difference to the masses of the objects found. From this point on, we use the higher threshold of 100 $M_{\odot}/pc^2$ to build the trees.

3.4.1.2 Finding clump masses with SKID

SKID is an Nbody group finder. It identifies structures using a friends-of-friends algorithm. Each structure then has unbound particles removed. Thus the final group contains only the bound mass formed. To find these masses with SKID the only essential parameter is a linking length. We choose a group linking length of 20 pc. Additionally, we consider only particles above 100 cm^{-3}, as these particles are dense enough to be part of the molecular medium. When recording the mass using SKID we take the mass of the central bound object. For the remainder of this section we report results using only SKID. We defer a detailed comparison of SKID and AstroDendro to a later section.

3.4.2 Clump masses in the turbulent disk

Figure 3.1 shows results for the cold, warm and hot disk. The right column of Figure 3.1 shows the mass histograms for bound objects in the disk, while the right panel shows surface density maps of the disks at the measurement time. The Toomre mass is plotted in each histogram panel as the dashed line. The maximum masses produced are 5.3×10^6 $M_\odot$, 1.1×10^8 $M_\odot$ and 2.5×10^8 $M_\odot$ for the cold, warm and hot disk, respectively.

The Toomre mass is sometimes proposed as the typical starting mass for clumps. If we compare our measured clump masses to the Toomre mass, we can see that there is a disagreement. Our measured maximum masses are consistently smaller than the Toomre mass, sometimes by an order of magnitude. While this is interesting in and of itself, using the full disks may introduce biases into measuring clump masses. For instance, laying turbulence everywhere introduces a competitive fragmentation scenario. Since the growth times for the smallest modes is shortest, the smallest size scales should collapse first. This competitive fragmentation may bias these disks to smaller clump masses. Further study is required to confirm that Toomre scale clumps are unlikely.

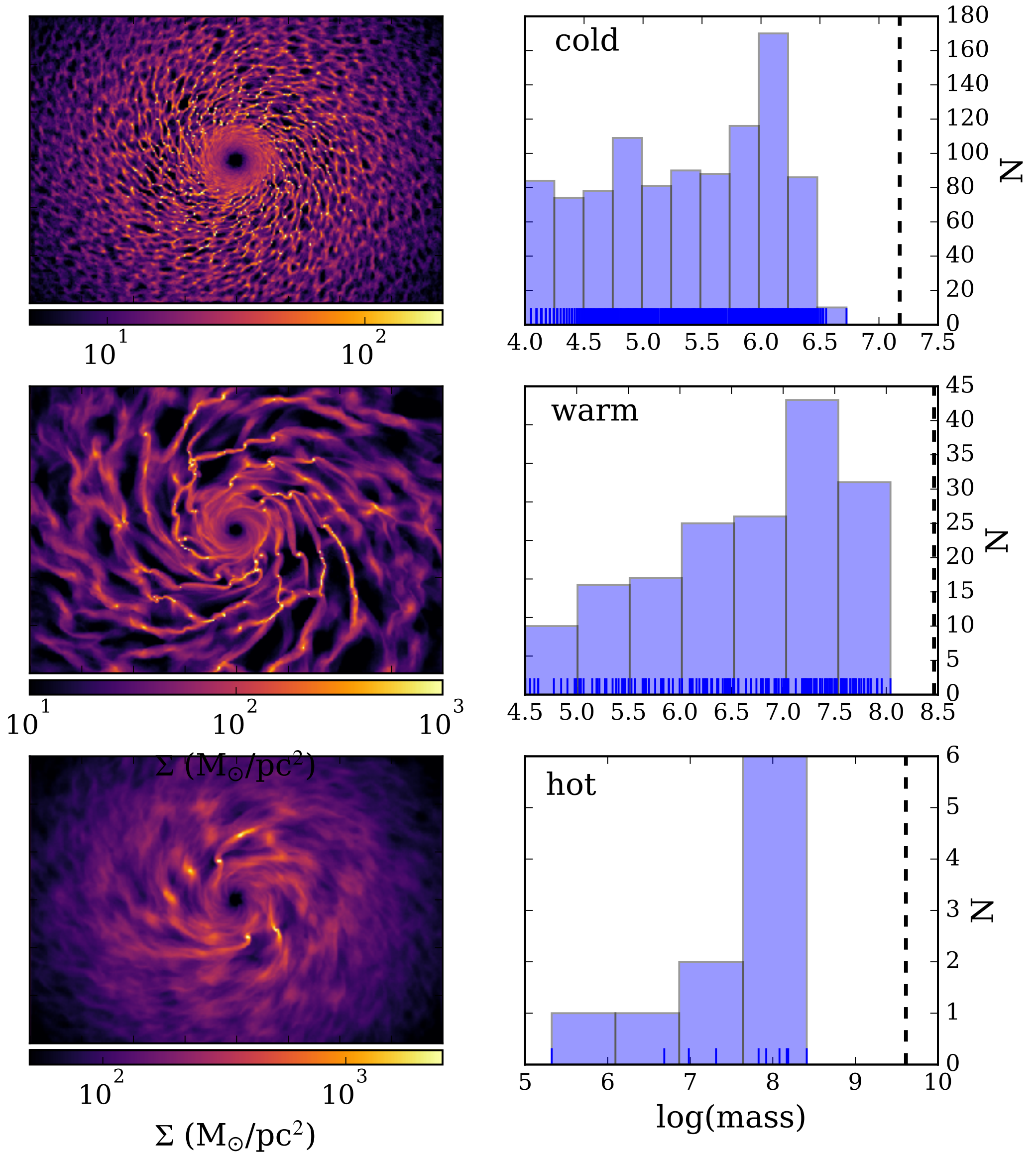

Figure 3.1: Mass distributions for clumps formed in the turbulent disks
Mass distributions for clumps formed in the turbulent disks. *Left*: surface density maps of the disks at 40 Myr (this is the time at which all mass measurements are made). *Right*: clump mass distributions measured using SKID. The dashed line shows the Toomre mass for each case. In the distributions, the blue short lines show the masses of each of the clumps to illustrate how the clumps are distributed between the bins. As the mass of the disk is increased, the mass of the clumps formed likewise increases. In all cases the clumps formed are less massive than the Toomre mass, sometimes by an order of magnitude.

3.5 Seeding Clump Formation

We now move on from the full turbulent disks discussed in the previous section. The fully turbulent disks have set an expectation for the range of clump masses possible in each of our quiet disk ICs. However, they are not a perfect comparison point. In particular, it is not possible to link each clump with the size scale and strength of the perturbation that seeded it. If we wish to compare to the Toomre mass, and the cases discussed in Section 3.2, we require a more controlled setup.

3.5.1 Seeding clump formation in quiet galaxies

In this section, we present a new approach to studying clump formation, or more generally the formation of bound structures, in simulations. In nature, turbulence is generated on large scales and then cascades down to feed smaller scales. It is these smaller scales which are of key interest in star formation. However, simulations struggle to capture the full turbulent cascade; it is difficult to resolve and maintain the full turbulent spectrum at the resolutions available for most galaxy-scale simulations (Kritsuk et al., 2007).

In Section 3.4, we avoided this problem by laying down a spectrum of turbulent velocities at the beginning of the simulation. The shape of our perturbation is modelled by the function

$$\Delta\vec{\mathrm{v}} = -\mathrm{v}_0 \, \left(\frac{r}{l/4}\right) \, e^{-0.5(r^2/(l/4)^2)} \, e^{0.5} \cdot \hat{r}, \tag{3.6}$$

where r is the distance from the centre of the perturbed region, v_0 is the chosen perturbation velocity, and l is the chosen perturbation wavelength. We choose this form such that $\Delta v_{max} = v_0$ at $r = l/4$, similar to a sine wave with wavelength l but

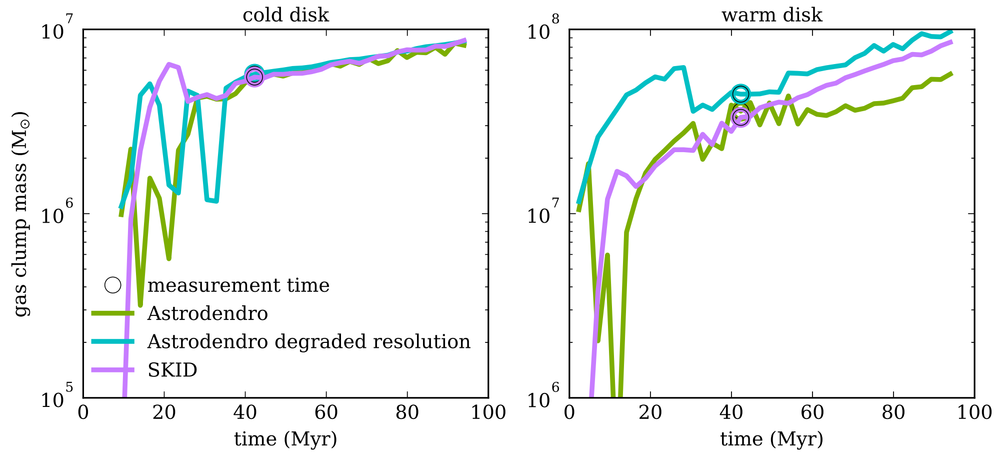

Figure 3.2: A comparison of the clump masses found by astrodendro versus SKID A comparison of the clump masses found by astrodendro versus SKID in the cold (left) and warm (right) disk. The green line shows the clump mass found by astrodendro as a function of time. The teal line shows the mass found by astrodendro if the initial resolution of the map is degraded to 100 pc. The purple line shows the bound mass identified by SKID as a function of time. The circles denote the time at which we record the mass measurement.

quickly returning to zero. For this function, the divergence is almost uniform (and negative) for $r < l/4$ and then smoothly returns to zero. Thus the characteristic collapse time is $l/(4v_0)$.

Effectively, we are introducing a radially compressive mode in the region of interest, such as could be generated by local feedback events. By then choosing different combinations of disk mass, perturbation wavelength and perturbation velocity, we can build a large parameter space of cases. In this way we can explore the conditions that tend to bound structure formation in disks of different masses.

3.5.2 Comparison of SKID and astrodendro

The clump masses as found by SKID and astrodendro agree when compared, after 30 Myr (the differences in the warm disk are no more than a factor of two). To illustrate this agreement, we choose two of our seeded clumps and follow their masses as a function of time with both SKID and astrodendro. The results of this analysis are shown in Figure 3.2. The left panel shows the results for a cold disk with a wavelength of 1 kpc and perturbation velocity of 10 km/s. The right panel shows the results for a warm disk with a wavelength of 1 kpc and a perturbation velocity of 30 km/s. The different coloured lines show different different clump finding methods; the purple line shows the results for SKID while the green line shows the results for astrodendro in each panel. Additionally, the teal line shows the results for astrodendro with the resolution degraded from 10 pc to 100 pc.

There are significant differences in the identified masses, but these differences occur while the clumps are still forming. The important region to consider is the span of time after which an identifiable bound object is formed. As mentioned previously, we take our mass measurements after ~ 30 Myr which is denoted as an open circle in Figure 3.2. In the cold disk, after this time, there is less than 10% variation between the different methods. As noted above, there are slightly larger differences when looking at the warmer disk, where the background surface density is intrinsically higher.

3.5.3 Clump Evolution

As mentioned previously, for the purposes of analysis we define a “clump” as a bound gas structure. We further require that this structure formed as a result of one of our seeded perturbations. To identify cases that are able to grow structure, we track the surface density of the perturbed region. For each case, we track the surface density in a 50 pc aperture centred on the initially perturbed particles. A sample plot for the evolution of the surface density with time can be seen in Figure 3.3 for five cases. The cases in Figure 3.3 span a range of velocities, from 1 to 15

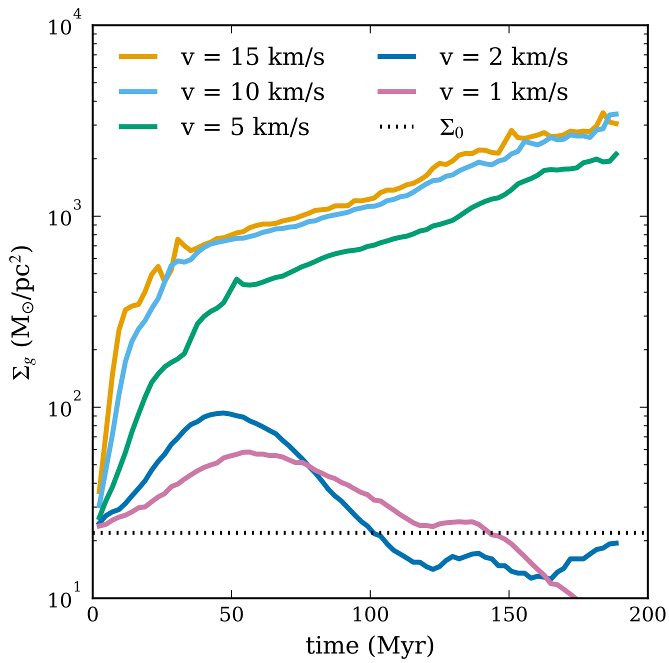

Figure 3.3: The evolution of the surface density for perturbations in the cold disk The evolution of the surface density for perturbations in the cold disk. The lines plot the surface density in a 50 pc aperture centred on the initially perturbed region. The cases with the smallest velocities, 1 and 2 km/s, show examples of perturbations that failed and could not produce a clump. The larger velocities, 5, 10 and 15 km/s, show examples of perturbations that produced a central clump. The dotted black line shows the initial background surface density of the disk.

km/s, but the wavelength of the initial perturbation is held constant at 1 kpc. The evolutionary tracks separate themselves into two distinct sets, those that increase in surface density and those that do not; we will discuss this in depth in the following sections.

To help visualize what our clump evolution actually looks like, we have plotted sets of surface density maps in Figures 3.4 and 3.5. For Figure 3.5, the snapshots are taken at the shear time,

$$t_{\text{shear}} = \frac{1}{\kappa}, \tag{3.7}$$

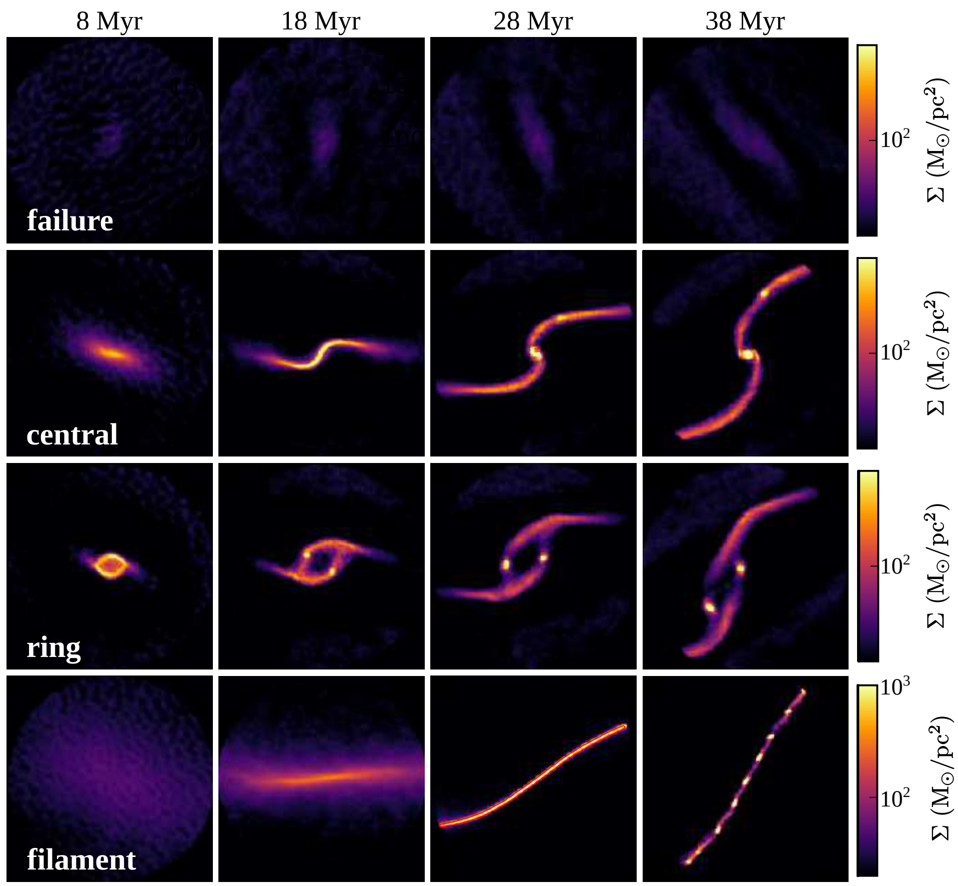

Figure 3.4: Evolution of the surface density for different clump formation scenarios Evolution of the surface density for different clump formation scenarios over time. *Top row*: a failed clump, as discussed in Section 3.5.4. *Second row*: a central clump, as discussed in Section 3.5.5. *Third row*: two ring clumps, as discussed in Section 3.5.6. *Bottom row*: a filament, as discussed in Section 3.5.7.

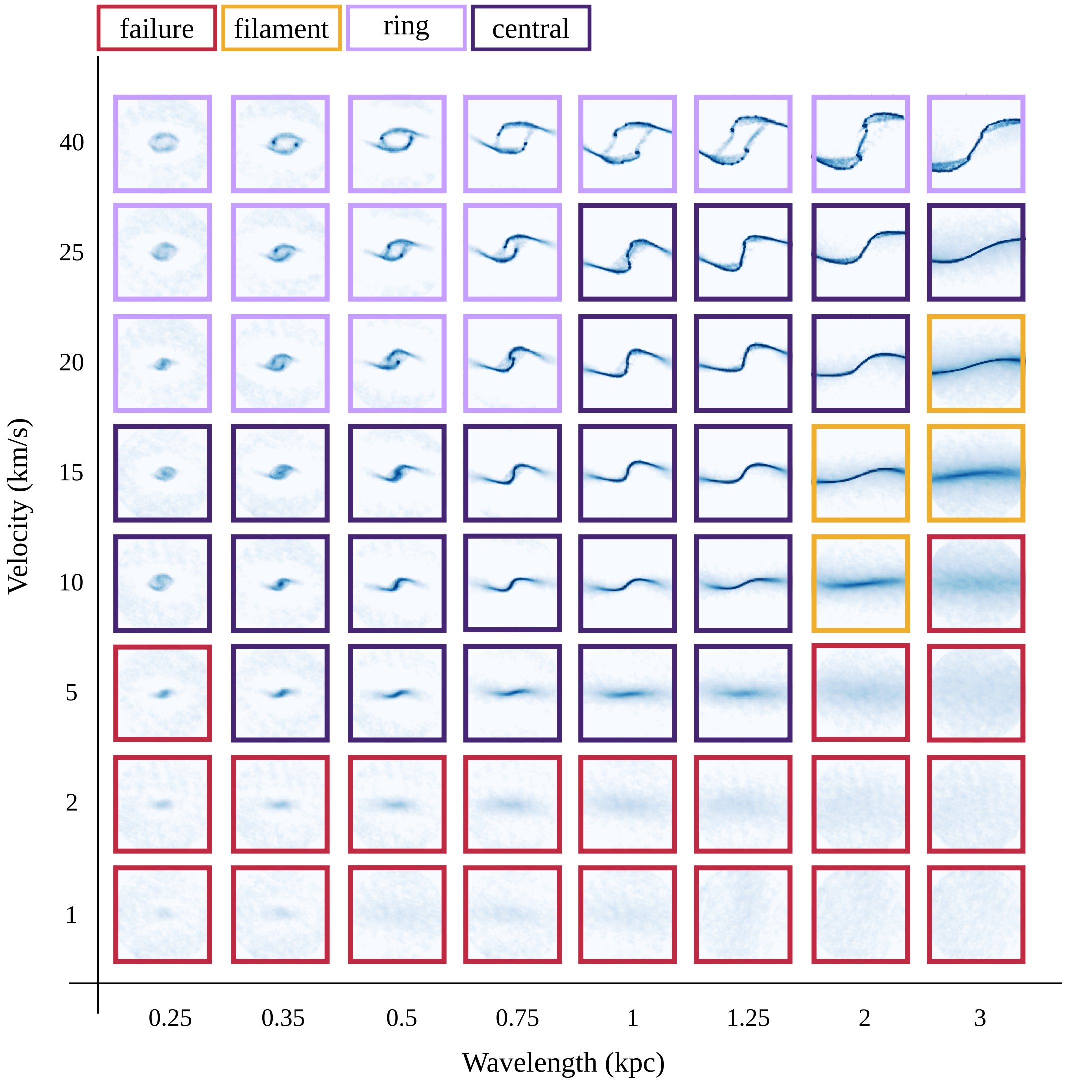

Figure 3.5: Sample surface density maps of different perturbations
Sample surface density images of different perturbations in the cold disk. There are four different types of cases when considering the evolution of the perturbation. Weak perturbations, with low velocity are clear failures; these images are outlined in red. Successful cases are those that form a dense object at their centre, where the original perturbation was centred. These cases are outlined in dark purple and occupy a distinct region in the l-v space. Strong perturbations, with high velocity, often lead to the formation of ring clumps. These cases are outlined in light purple. Lastly, are cases we label as filamentary. These are cases that exceed the maximum mass per unit length of a filament for fragmentation. These cases are outlined in yellow. These snapshots are taken at the shear time for the disk, ~ 15.5 Myr, and are 1 kpc across.

where κ is the epicycle frequency for the disk. In this case the shear time is 15.5 Myr. This is the time to shear out a distance equal to your size. We choose the shear time as the time to take representative snapshots as the perturbations have their fate determined by this point. On this timescale, a sheared structure can be shifted by order its own size; it is the period of a full epicycle. In this disk there are two main ways for a perturbation to fail. The first is thermal support due to the background sound speed in the disk. The second results from rotational support: this rotational support is associated with the initial shear and any later stretching due to ongoing shear. Thus, after one epicycle the perturbation should have started to collapse, or otherwise have begun to be sheared apart.

For the remainder of this section we discuss only the cold disk and use it as a case study to illustrate key concepts. All of the behaviour and cases discussed occur in all three of our galaxy disks, just in different regions of the $l - v$ parameter space.

3.5.4 Failed Perturbations

Referring back to Figure 3.3, two of the cases, with velocities of 1 and 2 km/s, are examples of perturbations that were not able to grow. Initially, they experience an increase in surface density, however, by $\sim$ 50 Myr, both have turned over and decrease until they oscillate around the background surface density of the disk; they are sheared apart. This behaviour can be seen in the top row of Figure 3.4, where a sample surface density map is shown in time spacings of 10 Myr. After 38 Myr of evolution, right before we take a mass measurement, there is no dense structure present. Cases like these are deemed “failures” and, looking at Figure 3.5, they occur mainly in the low velocity range. We can further define these cases as those that experience a turnover in their surface density.

The bottom two rows in Figure 3.5 show examples of failed cases, which are outlined in red. In a direct analogy with the Toomre criterion for linear perturbations, clump collapse can be opposed by both shear and pressure. The relevant timescales are the shear time and the sound-crossing time. Typically, depending on the scale, one of these dominates within a small region. Within a region roughly half the Toomre length, they are comparably important. This is quite similar to expectations for the linear, axisymmetric case (i.e. the Toomre criterion) and the non-axisymmetric case (Goldreich & Lynden-Bell, 1965b). In both those scenarios, and in this work, it is always the case that pressure and rotation work together to dissipate structure. Moving away from axisymmetry slightly boosts the role of rotation (see eqn 3.5).

The failed cases in Figure 3.5 trace out a rough parabolic shape in $l - v$ space. This parabola is reminiscent of the growth rate as a function of k for the Toomre instability. In the pure axisymmetric case, rings cannot shear and so the shear time is not important. In that case, any growth rate larger than zero leads to the growth of structure. However, in our non-axisymmetric case, rings can shear. This means that the growth rate must compete with the shear time: if the growth rate is not sufficient, perturbations will be sheared apart before structure forms. In our study, this is the case for long wavelengths. For shorter wavelengths the competition comes down to the pressure, or the sound crossing time. At those wavelengths, the sound crossing time must be less than the collapse time. In the coldest disk, this effectively requires that the perturbation velocity be larger than 5 km/s.

3.5.5 Central Clumps

Cases where clumps have formed in the centre of the initially perturbed region are the easiest to interpret. They can easily be identified because the evolution of their surface density shows a rapid phase of increase, followed by a phase of constant, steady growth. In Figure 3.3 the cases with velocities of 5, 10 and 15 km/s are perfect examples of cases that form central clumps.

We note that at later times, when the surface density has climbed too high, these clumps are numerically poorly resolved. We know that they are bound and expected to collapse further. This has been shown analytically by (Goldreich & Lynden-Bell, 1965b) for non-linear collapsed perturbations with an isothermal equation of state. However, the precise evolution of the surface density with time would require adaptive resolution beyond that employed here. For that reason, we do not place any special meaning on the steady exponential growth phase seen for collapsed objects past ~ 50 Myr (as is seen in both surface density and mass, as shown in Figures 3.2 and 3.3).

We are also able to identify trends between the initial perturbation parameters and the resulting surface density of the central region. We see that as the initial velocity is increased, within a shear time, it is possible to get higher and higher surface densities. This effect does begin to saturate if the velocity gets too high, above $\sim$ 15 - 20 km/s (see next section).

The second row of Figure 3.4 shows an example of the evolution of a central clump. There is a stark difference when this case is compared to the surface density of the failed case. For a central clump, already by 8 Myr the surface density in the middle of the perturbed region has surpassed 100 $M_\odot/pc^2$ and by 28 Myr there is clearly a dense bound structure present. In Figure 3.5 these central collapse cases are deemed “centrals” and outlined in dark purple. They occupy a specific region of the $l - v$ space.

For this scenario of clump formation, in the cold disk, masses between 8.47×10^5 M$_\odot$ and 1.6×10^7 M$_\odot$ are possible. All the results for our measured clump masses are plotted in Figure 3.7, where the top panel shows the cold disk that we discuss in this section. Clumps that form by fragmenting in the centre of the perturbation, as discussed here, are plotted as filled symbols. In Figure 3.7 we can see general trends with both velocity and wavelength. Generally, as the velocity is increased, the masses of the central clumps also increase. Similarly, as the wavelength of the perturbations is increased the masses of the clumps formed tend to increase as well.

3.5.6 Ring Clumps

A clump forming in the centre of a perturbation in the location where all of the velocities were directed is the most straightforward situation. However, there are more complicated scenarios that lead to the formation of bound structures. One such scenario involves the fission of a ring-like structure. The perturbations are initially directed radially inward. The higher the initial velocity, the larger the radius from which material can reach the centre quickly, within the shear time, for example. The angular momentum of the initial disk material with respect to the centre of the perturbation increases as r^2, where r is measured from the perturbation centre. Therefore, for large velocities the angular momentum per unit mass of the initially collapsed clump becomes quite high. This high angular momentum can cause the centre region to have too much rotational support and thus re-expand as a ring.

This ring expands and, as it does, is caught in the large-scale shear flow.

This means that portions of the ring can be dragged spinwise or counter-spinwise until they are ultimately stretched out to join tidal-like features. The rings thus have strong m=2 type modes, which results in two over-densities rather than one.

The third row of Figure 3.4 shows an example of the evolution of two ring clumps. Here again by 8 Myr the surface density has exceeded 100 $M_\odot/pc^2$, this time in the ring structure. By 20 Myr, the two ring clumps have begun to fragment. By 38 Myr, the ring has begun to be sheared apart, and the two ring clumps are clearly visible. Fragmentation in high spin cases leading to multiple objects has been found to occur in protostellar disks (Kratter & Matzner, 2006; Kratter et al., 2008).

Since this scenario requires a large angular momentum per unit mass in the centre of the perturbed regions, these cases are seen at high velocities. In Figure 3.5 the ring cases are outlined in light purple and can be found for cases with v $\gtrsim 20$ km/s. For the final masses in these cases we take the total bound mass of the two ring clumps.

The clumps formed from rings tend to have similar masses to central clumps when the two bound structures are counted together. In this case, total masses of between 9×10^5 $M_\odot$ and 1.8×10^7 $M_\odot$ are typical in the cold disk. When considered individually though, the clumps are less massive than those formed through the central fragmentation scenario. In Figure 3.7 the open symbols show the masses of ring clumps. Generally, these clumps follow the same trends as the central clumps. As the velocity is increased the clump mass increases, and as the wavelength is increased the clump mass increases. We can also see that, in general, the ring clumps have total masses that are higher than the central clumps. These high spin objects are consistent with the idea that observed large objects could be the result of beam crowding. In that case, we would actually be seeing the mass of multiple clumps in close proximity that formed out of a similar structure.

3.5.7 Filamentary Fragmentation

As noted earlier, when considering non-axisymmetric perturbations and long enough timescales, shear dominates the evolution of everything except the innermost bound clump. The shear will eventually draw the unbound material out into ever elongating tidal arm features. In an unrealistically quiet disk (such as in the controlled cases here) and over very long timescales, this material is wrapped to form a ring-like structure. In practice, the galaxy would have other perturbations acting on smaller timescales that break the the material up and use it to form other structures. However, there is an intermediate stage where the features are drawn out into filaments.

Perturbations with long wavelengths can exhibit a different mode of fragmentation. As time passes the long structures begin to behave like star-forming filaments. Such a filament will begin to fragment once its mass exceeds the critical line mass,

$$M_{\text{line}} = \frac{2c_s^2}{G} \tag{3.8}$$

where c_s is the sound speed and G is the gravitational constant (Inutsuka & Miyama, 1997). For our coldest disk the line mass works out to 11,624 $M_{\odot}$/pc. The average width of our long wavelength filaments is on the order of 40 pc. This means that our filaments only have to exceed surface densities of $\sim$290 $M_{\odot}$/pc^2 to be above the critical line mass and begin to fragment.

As time goes on and shear continues to operate, the filaments become more and more drawn out, decreasing the mass per unit length. This suggests there is a set time limit for the fragmentation in these objects to begin. If the original density of the filament is not high enough they will just be sheared apart.

We see this exact behaviour in many of our long wavelength perturbations. The bottom row of Figure 3.4 shows an example of a perturbation that develops filamentary behaviour and then fragments. By 18-28 Myr the density in the filament has begun to exceed the critical surface density calculated above. Indeed, by 38 Myr the filament has completely fragmented.

More examples of these filamentary cases can be seen on the right side of Figure 3.5, outlined in yellow. We label any structure produced by this phenomenon as secondary fragmentation. While it does lead to bound structures, there is different physics responsible for their production on top of our initial perturbation. In general these fragments are less massive than the central or ring clumps for comparable wavelengths and velocities. For example, at a wavelength of 2 kpc and a perturbation velocity of 10 km/s, the filamentary fragments are on average 2.4×10^6 $M_{\odot}$. As noted above, only very quiet disks would get the opportunity to use this mode of fragmentation so we have elected not to use it when comparing to observed disk properties. These masses are not included in Figure 3.7 or in any of the following discussion of mass.

3.6 What is the most likely clump mass?

In this section we use our measured clump masses to determine the most likely clump mass in a given galaxy. We begin with the coldest disk in our sample. In nature, bound structures, like clumps, are seeded by a cascade of turbulent energy. An extensive amount of work has been done to characterize the nature of this turbulence in molecular clouds (Myers, 1983; Solomon et al., 1987; Kritsuk et al., 2013). There is a correlation between the velocity dispersion, or linewidth, and the size of

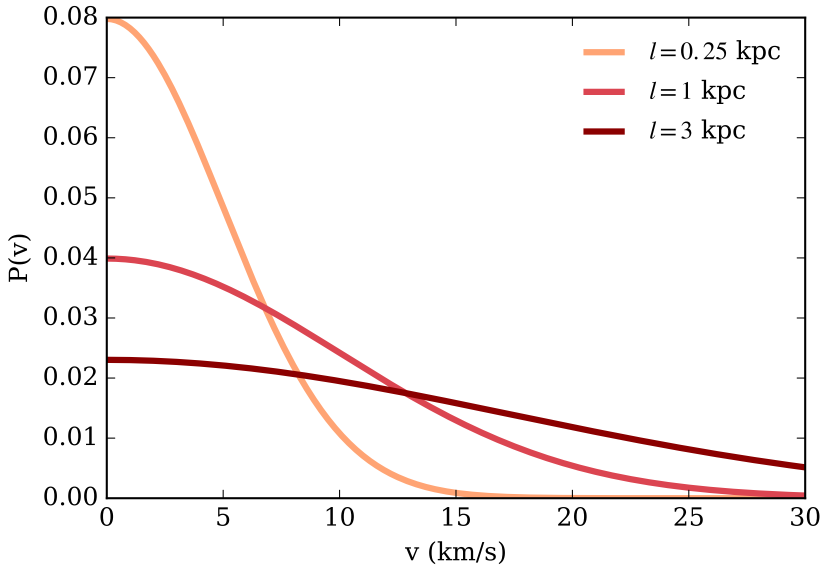

Figure 3.6: Sample probability distributions for three different wavelengths Sample probability distributions for three different wavelengths in the cold disk. These are generated assuming a spectrum of the form shown in equation 3.9. These are examples of the spectra used to generate the most likely mass for each wavelength. As we can see from the plot, for the cold disk, velocities above 15 km/s are very unlikely.

a region (Larson, 1981). Larson's first relation states

$$\sigma = A\,l^{1/2}, \tag{3.9}$$

where σ is the velocity dispersion, A is the normalization, and l is the scale at which that velocity is generated. For the cold disk, we assume that turbulence is generated by superbubbles, as it is in Milky Way-type galaxies. This gives σ_0 = 10 km/s, which is generated on a scale on the order of the scale height of the galaxy, l_0 = 1 kpc.

In order to assign a likelihood to each of our clump masses, we assign a probability to the velocity that seeded it. To assign this probability, we next assume that all of the velocities at a given wavelength are drawn from Gaussian distributions. Samples of the Gaussian distributions are shown in Figure 3.6 for three different wavelengths; 0.25, 1 and 3 kpc. Generating turbulent velocities by drawing from a Gaussian distribution is common practice (e.g. Price & Federrath, 2010).

In general, coherent velocities on large scales above 10 km/s begin to get more and more unlikely. By convolving these probabilities with the clump mass distributions that result from each velocity we can determine the most likely mass at each wavelength. The results of this analysis for the cold disk are shown in the top panel of Figure 3.7. In the middle panel of Figure 3.7 we plot the mass distribution for the warm disk, and the hot disk in the bottom panel. For these cases we assume a velocity dispersion of $\sigma_0 = 50$ km/s (Wisnioski et al., 2015). For the generation scale, we assume that this level of turbulence would be generated on a disk scale length, on the order of 3 kpc.

It is important to note that this study is useful for providing upper bounds on clump masses formed via fragmentation, since we do not include any star formation or feedback and do not account for any late stage accretion. That being said our approach offers a way to identify the most likely space for clump formation to operate in a given galaxy. In Figure 3.7 the dotted black line shows the most likely mass at each wavelength, while the grey shaded regions shows the 1σ probable region. We can see that in the cold disk, it is possible to get objects that begin to approach the predicted Toomre mass. However, the velocities required to form these objects are very high; they are not probable velocities. This in turn implies that while it is possible to make these larger bound structures approaching 10^7 M$_\odot$, it is not a likely outcome. This remains true as the disk mass, and thus the clump mass, is increased.

We can identify trends when considering the plots in Figure 3.7. First, as the velocity of the perturbations is increased, the mass of the resulting clumps increases. This is expected based on the the same trend observed for surface density in Figure 3.3. Second, there is a preferred mass scale for objects in a given disk. For the coldest disk the preferred fragmentation mass lies around 3×10^6 $M_\odot$, and little variation is seen away from this. This preferred mass lies around 4×10^7 $M_\odot$ and 5×10^8 $M_\odot$ for the warm and hot disks, respectively. As we increase the disk mass, of course, the clumps that form are generally more massive.

Additionally, there is a preferred fragmentation length in each disk. This length increases as the disk mass is increased. It is not possible to form bound structures below 0.25 kpc, 0.85 kpc, and 2 kpc for the cold, warm and hot disk, respectively. The physics behind these cutoffs was discussed in the previous section.

3.6.1 The Toomre Mass

As we did for the turbulent disk, we can compare the measured clump masses to the Toomre mass. As a reminder, for the coldest disk in our sample the critical wavelength is 940 pc, while the Toomre mass is 1.5×10^7 $M_\odot$. The Toomre mass is plotted as the orange star in Figure 3.7. The solid black line shows what the enclosed mass would be at different wavelengths. For the cold disk there is almost an order of mass discrepancy between the Toomre mass, and the expected mass (dotted line) at the critical wavelength. As the wavelength increases, so does the discrepancy between our measured masses and the ad hoc Toomre mass estimates.

In the warm disk, the critical wavelength is 2.4 kpc, which gives a Toomre mass of 2.9×10^8 $M_\odot$. If we move to the hot disk those get even larger, with a Toomre mass of 4.1×10^9 $M_\odot$ resulting from a critical wavelength of 5.4 kpc. These results are summarized in Table 3.1. Again, we see that masses predicted

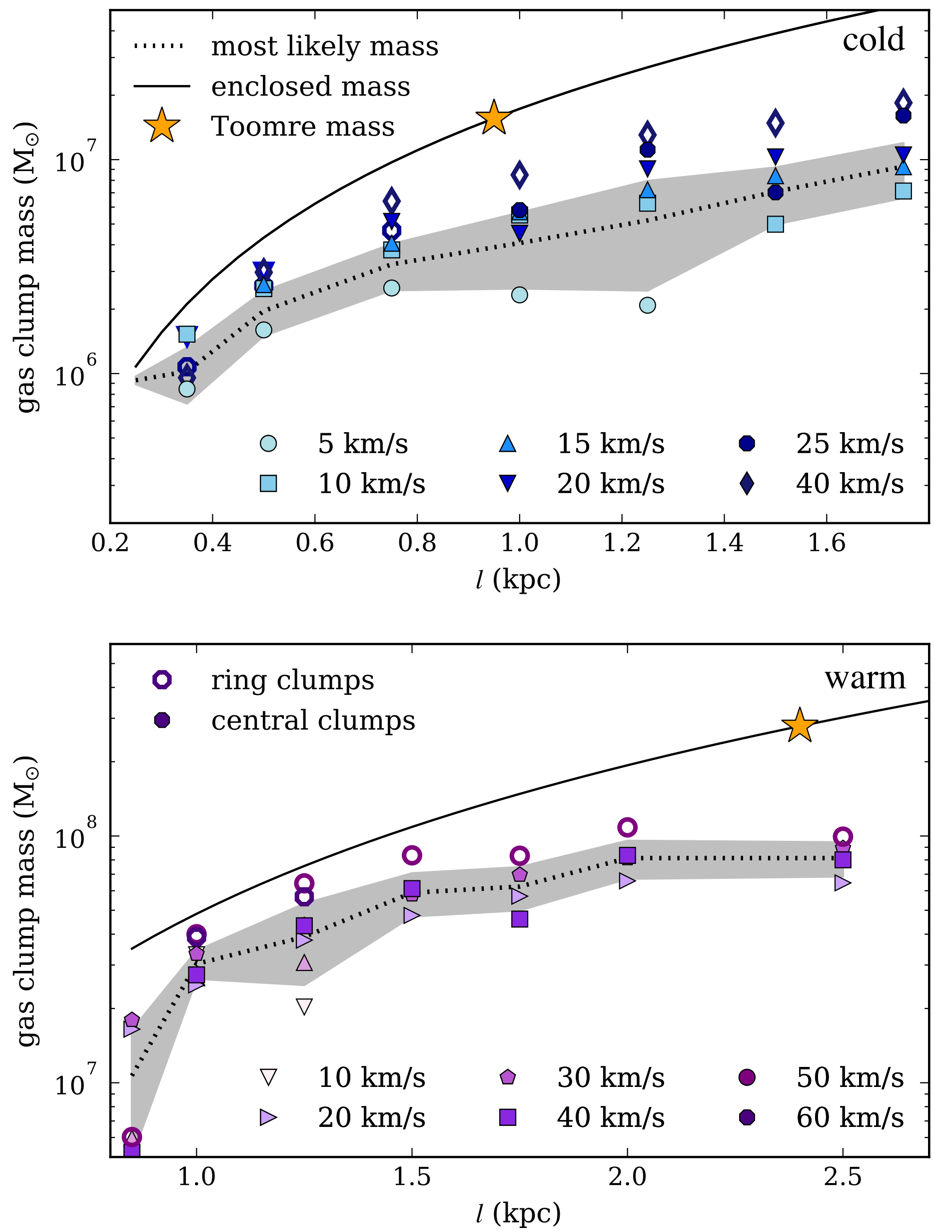

Figure 3.7: The most likely clump mass

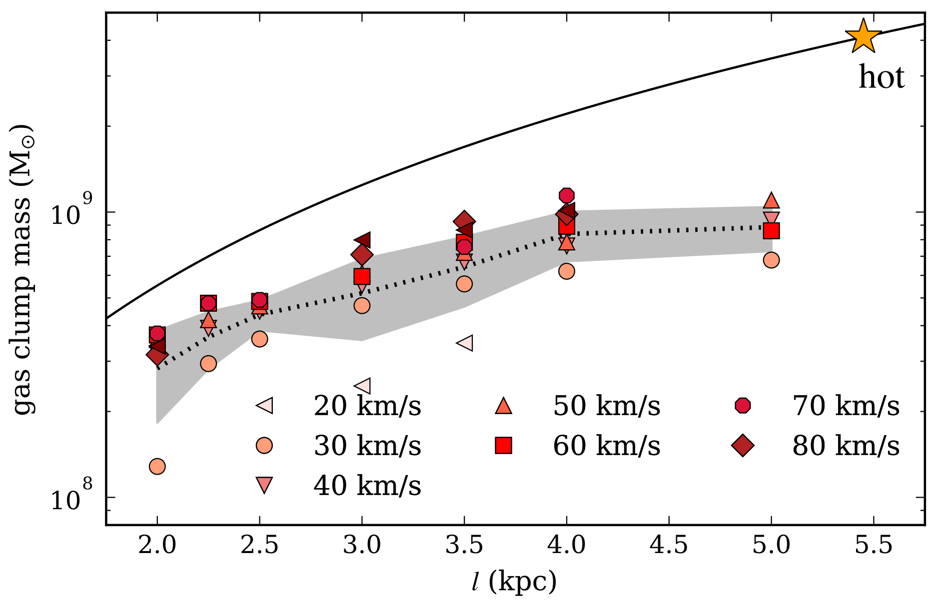

Figure 3.7: The most likely clump mass *cont'd*

The most likely clump mass. *Top*: the masses in our cold disk. *Middle*:the masses in our warm disk. *Bottom*: the masses in our hot disk. In each plot the filled symbols denote central clumps, the open symbols denote ring clumps and the stars show the Toomre mass at each wavelength. The grey dashed line shows the mean expected mass and the shaded region shows the 1σ deviation (see section 3.6). Our measured clump masses wind up being smaller than the predicted Toomre mass. The shaded 1σ region also shows us that, while it is possible to get closer to the Toomre mass, it is not a likely case in nature.

from Toomre theory are consistently over-estimates when compared to our seeded clump masses.

We find that our masses are between a quarter and half of the Toomre mass. This discrepancy can be explained by considering the limitations of Toomre theory. While the Toomre prediction is linear in construction, as objects grow more dense and fragment their behaviour is increasingly non-linear. Secondly, the system, and few systems in nature, are axisymmetric. Finally, as the mass of the disk and its sound speed increase, the critical wavelength likewise increases. In our most massive, hottest, disk the critical wavelength increases to 5.4 kpc. A critical wavelength that large represents a significant portion of a galaxy disk. In fact, at high redshift, that may be the entire radius of the galactic disk. This has likewise been noted by Reina-Campos & Kruijssen (2017). Through angular momentum considerations alone this scenario is not possible: the collapse of the whole disk is ruled out and thus $l \gtrsim r_d$ must fail.

3.7 Discussion & Observational Implications

Up to this point we have assumed very fine resolution for our measurements. This makes our mass measurements most comparable to high resolution observations, like those of Johnson et al. (2017b), with effective resolution of 40 pc. To compare to a broad range of observational results we must try to account for the possibility of coarser resolution.

We choose 1 kpc, to be comparable to the beams in the CANDELS survey which are typically between 500 pc to 1 kpc. This is in the range of resolution for multiple other high redshift surveys. To compare to the stellar mass of clumps, we also estimate the location of newly formed stars in our disks. We do not employ star formation and stellar feedback in these simulations. However, we can tag likely locations for star formation by identifying all gas that surpasses 116 $M_{\odot}/pc^2$; this is the threshold identified by Lada et al. (2010) for star formation. The simulations we use for comparison in this section are the seeded disks, discussed in section 3.5.

To estimate the impact of beam smearing we then change the way we assign masses to our seeded clumps. Up until this point, the masses quoted are the masses of a single bound structure at the centre of the perturbation or two bound objects in the case of a ring structure. In this section, we take all bound structures identified in the inner 1 kpc around the perturbation centre. The results of this analysis are plotted as the squares in Figure 3.8. These points show the average of the masses found in each disk. The error bars show the standard deviation, found using the velocity averaging method discussed in section 3.6.

We have had to make assumptions about the stellar mass content of our disks. We are using isolated galaxies in static potentials so our sample is not indicative of galaxies that have high stellar mass content. Typical gas fractions for galaxies above redshift 0.5 can fall anywhere between 0.2 and 0.8 (Morokuma-Matsui & Baba, 2015). Here we take the definition that the gas fraction is

$$f_{\mathrm{g}} = \frac{M_g}{M_g + M_*}, \tag{3.10}$$

where M_g and M_* are the total gas and star mass of the galaxy, respectively. Again, since our galaxies cannot capture the dynamics of those with a high stellar fraction, we take the maximum possible gas fraction for our galaxies to be 0.5.

For comparison in Figure 3.8 we plot the sample of clumps discussed in Guo et al. (2018). The averages of the clump masses in galaxy mass bins of width 0.5 dex are plotted as the black circles. The grey shaded region shows the range of the minimum and maximum clump mass in each bin. We also plot the higher resolution lensed clump sample discussed in Livermore et al. (2015). We note that the sample of Livermore et al. (2015) originally states only star formation rates for their clumps. We have converted these to rough masses by assuming the clumps form stars at this steady rate for their estimated lifetime.

The clump lifetime is still a debated topic. Some theories suggest that clumps migrate into the centre of galaxy disks, which suggests their lifetimes must be longer than 150 Myr (e.g. Shibuya et al., 2016). Other studies suggest a quick disruption due to strong feedback, giving a shorter lifetime of around 50 Myr (e.g. Krumholz & Dekel, 2010; Oklopčić et al., 2017). We take a clump lifetime of 100 Myr to convert the sample. This value means our masses estimated from the Livermore et al. (2015) sample will be an underestimate for the mass if the clump lifetime is long, and an overestimate if the lifetime is short in nature.

On the lower galaxy mass end, for our cold and warm disks, our sample agrees quite well with the findings of Livermore et al. (2015). For our most massive galaxy, the hot disk, our clump masses agree well with both the Guo et al. (2018) and Livermore et al. (2015) samples. As further comparison, the large blue, purple and red circles in Figure 3.8 show how many of our clumps would have to be crowded in a beam to get our mass to the average Guo et al. (2018) mass. For the cold, least massive disk, we would need to have 45 of our clumps in the beam. This number becomes more reasonable as we move to higher disk masses, 11 clumps in the warm disk and only 3 in the hot. These smaller factors agree well with the resolution scaling factors discussed by Cava et al. (2018).

Our results suggest insights into clump formation, particularly in galaxies on the lower mass end (below 10^{10} $M_{\odot}$). We stress that the observationally measured mass of clumps is not necessarily the mass at which they formed. Our results

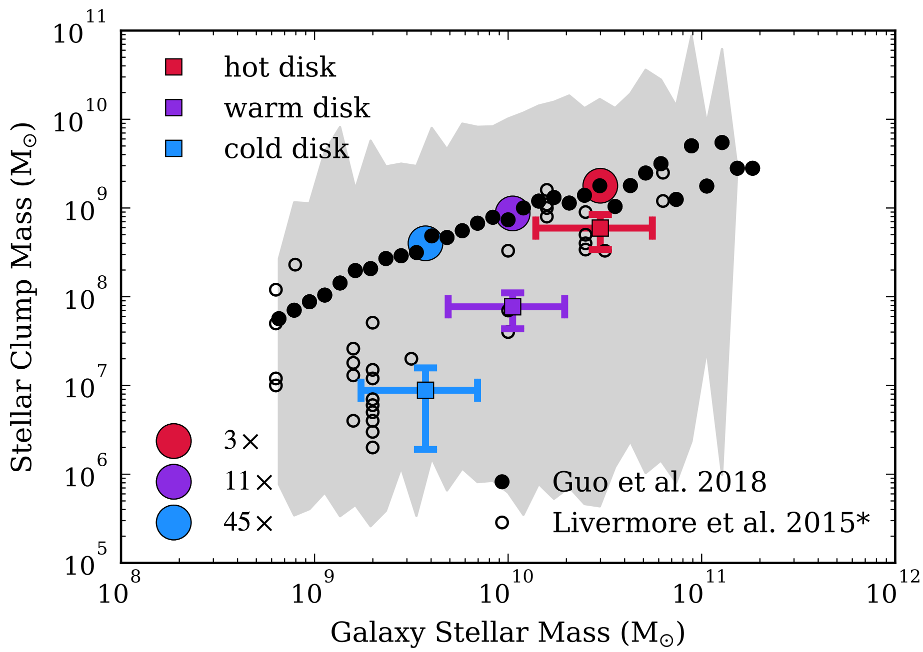

Figure 3.8: The expected stellar clump mass as a function of galaxy mass
The expected clump stellar clump mass as a function of the stellar mass content of the galaxy. The average of our seeded disk clumps is plotted as each of the filled squares. The vertical errorbars show the standard deviation of the data. The horizontal errorbars show possible values of gas fractions for the conversion from gas to stellar galaxy mass. Two observational samples are plotted for comparison. The black circles shows the average clump mass in 0.5 dex mass bins for the sample of Guo et al. (2018) and the grey shaded region shows the range spanned by the data. The open circles show our estimate of the clump mass for the lensed sample detailed in Livermore et al. (2015). To convert from the original SFR measurements of Livermore et al. (2015) we assume that a clump's lifetime is 100 Myr, and that the measured SFR is sustained for this entire time. The large red, purple and blue filled circles show the level of beam crowding we would require to agree with the average CANDELS clump in a galaxy of comparable mass.

suggest that beam crowding likely plays a role in the measurement of large clump masses in these smaller galaxies. Alternatively, clump mergers may play a role in building larger objects. Tamburello et al. (2015) also find that clump-clump mergers are required to build the largest objects. If clumps are long-lived, late-stage accretion can also build clump masses. On the higher disk mass end there are other ongoing effects that we do not discuss nor attempt to capture here. However, our results suggest that the largest observed clump masses likely result from the crowding or clustering of smaller objects into larger observational beams.

3.8 Summary & Conclusions

In this work, we have introduced a new method for studying the formation of clumps, or bound structures, in galactic disks. We seed clump formation events in initially stable isothermal disks, without star formation or feedback. We design these conditions to be purposefully simple and thus offer maximum control. Our clump mass spectra are not impacted by feedback recipe choices, providing a complementary approach to other recent work that employs a variety of feedback assumptions.

By seeding turbulent clump formation events, we are able to study the exact conditions under which different clump masses form. In general, we find that our largest clump masses can be over an order of magnitude smaller than the Toomre mass. Our results suggest smaller initial masses for clumps than reported in some observational studies. This is consistent with the idea that those studies have large beams that encompass many bound objects. We stress that when making this comparison, the clump observational mass may be different than the initial mass: just because an object is observed to be massive, does not mean it formed at that mass through gravitational fragmentation.

Our method provides a new way to approach the problem of studying clump formation in simulations; it offers a new way to compare to observations. The method can be completely tailored to specific galaxies. The only requirement is that the rotation curve and surface density distribution for the galaxy are known. Our method provides a promising new way to study the formation of these clumps in specific galaxies without the biases introduced by including different feedback methods.

Acknowledgements

The authors thank Chelsea Sharon and Ralph Pudritz for helpful discussions. SMB acknowledges support from the Vanier Canada Graduate Scholarship Program. JW and HMPC acknowledge support from NSERC. This research made use of astrodendro, a Python package to compute dendrograms of Astronomical data[2]. This research made use of Astropy, a community-developed core Python package for Astronomy (Astropy Collaboration, 2018)[3]. Computations were performed on the GPC supercomputer at the SciNet HPC Consortium. SciNet is funded by: the Canada Foundation for Innovation under the auspices of Compute Canada; the Government of Ontario; Ontario Research Fund - Research Excellence; and the University of Toronto.

[2]https://dendrograms.readthedocs.io/en/stable/
[3]http://www.astropy.org

Bibliography

Agertz O., Teyssier R., Moore B., 2009, MNRAS397, L64

Agertz O., Romeo A. B., Grisdale K., 2015, MNRAS, 449, 2156

Aravena M., et al., 2010, ApJ, 718, 177

Bate, M. R. and Burkert, A., 1997, MNRAS, 288, 1060

Behrendt M., Burkert A., Schartmann M., 2016, ApJ, 819, L2

Bigiel F., Leroy A., Walter F., Brinks E., de Blok W. J. G., Madore B., Thornley M. D., 2008, AJ, 136, 2846

Binney J., Tremaine S., 2008, Galactic Dynamics: Second Edition. Princeton University Press

Bournaud F., et al., 2014, ApJ,780, 57

Cacciato M., Dekel A., Genel S., 2012, MNRAS, 421, 818

Cava A., Schaerer D., Richard J., Pérez-González P. G., Dessauges-Zavadsky M., Mayer L., Tamburello V., 2018, Nature Astronomy, 2, 76

Colombo D., et al., 2014, ApJ, 784, 3

Colombo D., Rosolowsky E., Ginsburg A., Duarte-Cabral A., Hughes A., 2015, MNRAS454, 2067

Daddi E., et al., 2010, ApJ, 713, 686

Dekel A., Sari R., Ceverino D., 2009, ApJ703, 785

Dessauges-Zavadsky M., Adamo A., 2018, MNRAS,

Dessauges-Zavadsky M., Schaerer D., Cava A., Mayer L., Tamburello V., 2017, ApJ, 836, L22

Elmegreen D. M., Elmegreen B. G., Ravindranath S., Coe D. A., 2007, ApJ, 658, 763

Fall S. M., Chandar R., 2012, ApJ, 752, 96

Fiacconi D., Mayer L., Madau P., Lupi A., Dotti M., Haardt F., 2017, MNRAS, 467, 4080

Fisher D. B., et al., 2017, MNRAS, 464, 491

Förster Schreiber N. M., et al., 2009, ApJ, 706, 1364

Fukui Y., Kawamura A., 2010, ARA&A, 48, 547

Genzel R., et al., 2011, ApJ, 733, 101

Goldreich P., Lynden-Bell D., 1965a, MNRAS130, 97

Goldreich P., Lynden-Bell D., 1965b, MNRAS, 130, 125

Guo Y., et al., 2015, ApJ, 800, 39

Guo Y., et al., 2018, ApJ, 853, 108

Hodge J. A., Carilli C. L., Walter F., de Blok W. J. G., Riechers D., Daddi E., Lentati L., 2012, ApJ, 760, 11

Hopkins, P. F., 2012, MNRAS, 423, 2016

Hopkins P. F., Kereš D., Murray N., Quataert E., Hernquist L., 2012, MNRAS, 427, 968

Inoue S., Dekel A., Mandelker N., Ceverino D., Bournaud F., Primack J., 2016, MNRAS, 456, 2052

Inutsuka S.-i., Miyama S. M., 1997, ApJ, 480, 681

Jog C. J., 1992, ApJ, 390, 378

Jog C. J., Solomon P. M., 1984a, ApJ, 276, 114

Jog C. J., Solomon P. M., 1984b, ApJ, 276, 127

Johnson T. L., et al., 2017a, ApJ, 843, 78

Johnson T. L., et al., 2017b, ApJ, 843, L21

Kratter, K. M. and Matzner, C. D. and Krumholz, M. R., 2008, ApJ, 681, 375

Kratter, K. M. and Matzner, C. D., 2006, MNRAS, 373, 1563

Kritsuk A. G., Norman M. L., Padoan P., Wagner R., 2007, ApJ, 665, 416

Kritsuk A. G., Lee C. T., Norman M. L., 2013, MNRAS, 436, 3247

Kruijssen J. M. D., 2012, MNRAS, 426, 3008

Krumholz M. R., Dekel A., 2010, MNRAS, 406, 112

Lada C. J., Lombardi M., Alves J. F., 2010, ApJ, 724, 687

Larson R. B., 1981, MNRAS, 194, 809

Livermore R. C., et al., 2015, MNRAS, 450, 1812

Mandelker N., Dekel A., Ceverino D., Tweed D., Moody C. E., Primack J., 2014, MNRAS, 443, 3675

Mandelker N., Dekel A., Ceverino D., DeGraf C., Guo Y., Primack J., 2017, MNRAS, 464, 635

McKee C. F., Ostriker E. C., 2007, ARA&A, 45, 565

Morokuma-Matsui K., Baba J., 2015, MNRAS, 454, 3792

Murray N., Quataert E., Thompson T. A., 2010, ApJ, 709, 191

Myers P. C., 1983, ApJ, 270, 105

Oklopčić A., Hopkins P. F., Feldmann R., Kereš D., Faucher-Giguère C.-A., Murray N., 2017, MNRAS, 465, 952

Price D. J., Federrath C., 2010, MNRAS, 406, 1659

Reina-Campos M., Kruijssen J. M. D., 2017, MNRAS, 469, 1282

Rigby J. R., et al., 2017, ApJ, 843, 79

Robertson B. E., Kravtsov A. V., 2008, ApJ, 680, 1083

Romeo A. B., Wiegert J., 2011, MNRAS, 416, 1191

Romeo A. B., Burkert A., Agertz O., 2010, MNRAS, 407, 1223

Rosolowsky E. W., Pineda J. E., Kauffmann J., Goodman A. A., 2008, ApJ, 679, 1338

Shibuya T., Ouchi M., Kubo M., Harikane Y., 2016, ApJ, 821, 72

Solomon P. M., Rivolo A. R., Barrett J., Yahil A., 1987, ApJ, 319, 730

Swinbank A. M., et al., 2010, Nature, 464, 733

Swinbank A. M., et al., 2011, ApJ, 742, 11

Tacconi L. J., et al., 2010, Nature, 463, 781

Tacconi L. J., et al., 2013, ApJ, 768, 74

Tamburello V., Mayer L., Shen S., Wadsley J., 2015, MNRAS

Tamburello V., Rahmati A., Mayer L., Cava A., Dessauges-Zavadsky M., Schaerer D., 2017, MNRAS

Toomre A., 1964, ApJ, 139, 1217

Truelove J. K., Klein R. I., McKee C. F., Holliman II J. H., Howell L. H., Greenough J. A., 1997, ApJ, 489, L179

Wadsley J. W., Stadel J., Quinn T., 2004, New A

Wadsley J. W., Keller B. W., Quinn T. R., 2017, MNRAS, 471, 2357

Ward R. L., Wadsley J., Sills A., Petitclerc N., 2012, ApJ, 756, 119

White H. A., et al., 2017, ApJ, 846, 35

Wilson C. D., Harris W. E., Longden R., Scoville N. Z., 2006, ApJ, 641, 763

Wisnioski E., et al., 2015, ApJ, 799, 209

Chapter 4

The anatomy of a star-forming galaxy II: the role of FUV heating and pressure in regulating star formation

S. M. Benincasa, J. W. Wadsley, H. M. P. Couchman, A. R. Pettitt, J. Grond, B. W. Keller and R. M. Woods

This article has been prepared for submission to The Monthly Notices of the Royal Astronomical Society.

Abstract

FUV radiation is the dominant source of heating in the cold neutral ISM. This suggests that it should be an important source of feedback in galaxy simulations, in partnership with supernovae. We present the first study of a full galaxy simulated with self-consistent FUV heating. This FUV heating is implemented using the radiative transfer algorithm TREVR, in the simulation code GASOLINE. We find that on its own, FUV heating cannot regulate star formation in galaxies. However, in combination with superbubble feedback, it is able to preserve spiral structure while regulating star formation. In order to quantify the impacts of choosing these different types of feedback, we use multiple diagnostics to quantify the state of the ISM and star formation in the galaxy.

4.1 Introduction

In galaxy evolution, the Interstellar Medium (ISM) and star formation are intimately linked. This behaviour emerges in a number of empirical relations. The Kennicutt-Schmidt relation connects the star formation rate surface density with the total gas surface density, $\dot{\Sigma}_* \sim \Sigma_g^N$, where $N \sim 1.4$ (Kennicutt, 1998). The star forming main sequence similarly shows that there is a tight correlation between the galactic star formation rate and the stellar mass of a galaxy (Brinchmann et al., 2004; Daddi et al., 2007; Noeske et al., 2007). These relations manifest themselves both on the full galaxy scale and the resolved local scale: the kpc-scale for the star-forming main sequence (Hsieh et al., 2017) and the sub-kpc scale for the Kennicutt-Schmidt relation (Bigiel et al., 2008).

The original Kennicutt-Schmidt relation probed galaxies with typical surface densities $\Sigma_g \gtrsim 10\,\mathrm{M}_\odot/\mathrm{pc}^2$ (Kennicutt, 1998). However, as we have added more data to this relation, on different scales or at lower surface densities, the picture has become more complicated. With the addition of this data we see two interesting behaviours emerge.

First, there is a break in the power-law at low surface densities; below surface densities of $\Sigma_g \lesssim 10$ $\mathrm{M}_\odot/\mathrm{pc}^2$ the relation steepens significantly, so that for a specific Σ_g there can be a range of $\dot{\Sigma}_*$ spanning several orders of magnitude. This is similar in nature to the cutoff of star formation observed for galaxy edges; there is a cutoff of the galactic SFR well before the end of the extended HI disk (e.g. Martin & Kennicutt, 2001).

The dominant physics regulating star formation changes as we consider different regimes in surface density. At high surface densities, $\Sigma_g \gtrsim 100$ $\mathrm{M}_\odot/\mathrm{pc}^2$, the combination of supernovae and radiation pressure are the main physics regulating star formation (Ostriker & Shetty, 2011; Shetty & Ostriker, 2012). Between $10 \lesssim \Sigma_g \lesssim 100\,\mathrm{M}_\odot/\mathrm{pc}^2$, we expect combinations of superovae feedback and stellar UV heating to play a large role in regulating the star formation rate (Ostriker et al., 2010; Kim et al., 2011). At lower surface densities, where the star formation rate is necessarily lower, the physical arguments are different. It has been suggested that the key ingredient for star formation is the presence of two thermal phases in the ISM (Elmegreen & Parravano, 1994). It may be the absence of a long-lived cold phase in the outer regions of disks that causes such a low star formation rate (Schaye, 2004).

The second new behaviour that emerges from the Kennicutt-Schmidt relation is the scatter from the original power-law; in some regions there is scatter of almost 2 dex. This intrinsic scatter is not due to measurement error, it is real and meaningful. There is, however, little scatter when we consider only data points from specific galaxies; single galaxies occupy tight regions in the $\dot{\Sigma}_* - \Sigma_g$ plane (e.g. Bigiel et al., 2008; Ostriker et al., 2010). Taken together, this suggests that there are additional parameters controlling this relation (e.g. Krumholz et al., 2012; Saintonge et al., 2017).

The Silk-Elmegreen law is a popular re-parameterization of the Kennicutt-Schmidt relation, where the orbital time is taken into account with the gas surface density (Silk, 1997; Elmegreen, 1997). Alternatively, a similar approach is to take the free-fall time of the gas into account (Krumholz et al., 2012; Salim et al., 2015). Leroy et al. (2008) did extensive work studying the relations between different ISM properties, including the molecular gas fraction, the orbital time, the Toomre Q stability and the pressure among others. While the authors were unable to identify a clear driver changing the star formation efficiency, this work suggests that unresolved ISM physics play an important role in the conversion from average ISM, to

GMCs to stars.

The total pressure has also been considered as an additional parameter. The total galactic pressure is a key quantity connecting to the interaction of star formation and the ISM (Ostriker et al., 2010; Blitz & Rosolowsky, 2004). The model of Ostriker et al. (2010) attributes new star formation to the need to balance the pressure required due to the gravity of the gas, stellar and dark matter components, and the pressure support, provided by pressure, heating/cooling, etc... In this model the stellar gravity plays a large role in setting the pressure requirement which translates directly into parameterizations of the form $\dot{\Sigma}_* \propto \Sigma_*^N \Sigma_g$; stars are likely to form where stars have already formed in the past. Reworking the Kennicutt-Schmidt relation to incorporate the stellar surface density, such that $\dot{\Sigma}_* \propto \Sigma_*^N \Sigma_g$, the scatter can be significantly tightened (Shi et al., 2018).

There is a connection between pressure, star formation and dense gas fraction that has been observationally established (Wong & Blitz, 2002; Blitz & Rosolowsky, 2004, 2006; Gallagher et al., 2018). This relation has also been studied analytically and through numerical simulations (Ostriker et al., 2010; Ostriker & Shetty, 2011; Kim & Ostriker, 2015; Benincasa et al., 2016). The transition from atomic to molecular gas may be a rate-limiting step and, in connection with the total pressure, influences the star formation rate (e.g. Herrera-Camus et al., 2017). This can be looked at as a consequence of the transition between different ISM phases. A consequence of this transition is that the efficiency of star formation changes. If we consider the Kennicutt-Schmidt law for the molecular gas surface density instead of the total gas surface density the slope becomes linear (Bigiel et al., 2008).

The ISM is multiphase in nature (Wolfire et al., 2003; Cox, 2005; Kritsuk & Norman, 2002). Models like those of Ostriker et al. (2010) assume that gas predominantly lives in either a warm diffuse phase, or a cold dense phase. In this model star formation is linked to the amount of cold gas. However, this is a simplified picture. In reality, there are not two clear phases in the ISM, but rather there is substantial gas living at intermediate temperatures. The timescale for the ISM to separate into two distinct phases is long compared to the timescales on which feedback and turbulence operate. This means that the picture is not as straightforward as one would hope. Firstly, there is never a clean separation present between phases. Secondly, the model of Ostriker et al. (2010) does accurately account for the role of turbulence in this process.

Simulations are a good place to study how star formation is regulated over time. Studies that target the regulation of star-formation often harness cosmological galaxy simulations (e.g. Hopkins et al., 2014). It has been shown that the galactic scale height is an important quantity in the cycle of regulation; if the scale-height is not resolved, the processes regulating star formation cannot be fully resolved (Benincasa et al., 2016; Kim et al., 2013). Specifically, this problem manifests itself as incorrect measurements of the pressure. This can be a problem, even at the scale of cosmological zoom-in simulations.

On the opposite end of the size-scale, studies that target the structure of the ISM often harness stratified box simulations (e.g. Walch et al., 2015). While stratified boxes offer higher resolution, they lack the full galactic context. Unless shearing boxes are used, the full impact of galactic shear as a key source of both turbulence and structure is not accounted for. Galaxies have significant populations of weakly bound and unbound GMCs; there is molecular gas that is not forming stars at high rates (Ward et al., 2016). The galactic shear may be key to to maintaining gas in this state without requiring excessive feedback (McNally et al., 2009). This physics is missed by stratified boxes. Further, the linear box geometry introduces strong geometric biases that hamper the modelling of feedback; it has been shown that the mass-loading rate scales with the chosen box height (Martizzi et al., 2016). A correct wind solution is not possible in the linear geometry (Consolmagno & Schaefer, 1994). This leads to physically incorrect wind behaviour and bursty, unstable ISM characteristics.

In between these two commonly used approaches lie isolated galaxy simulations. These are an ideal place to study the structure of the ISM and star formation; they offer both high resolution and the full galactic context. There is a strong body of work studying the ISM in numerical simulations using isolated galaxies. Most studies focus on the formation and evolution of GMCs, as they are the intermediary step between diffuse gas and star formation (e.g. Tasker & Tan, 2009; Benincasa et al., 2013; Pan et al., 2015; Rey-Raposo et al., 2017; Duarte-Cabral & Dobbs, 2017; Dobbs et al., 2018). Other studies focus on the stability of gas, and searching for signatures that suggest star formation (e.g. Nguyen et al., 2018; Agertz & Kravtsov, 2015; Grisdale et al., 2018; Benincasa et al., 2016). However, as a simulation approach, isolated galaxies are still generally under-appreciated and under-explored.

In galaxy simulations, feedback process are the simulator's main method of controlling the availability of star-forming gas. Feedback is invoked as necessary to regulate star formation with a strong historical reliance on supernova feedback. We know that these processes work to regulate the global star formation rate or reproduce the Kennicutt-Schmidt relation. However, even simplistic feedback can achieve regulation with free parameters; methods can be calibrated to produce the desired star formation rate. In that sense, one could argue that regulation alone does not tell us much about the state of simulated galaxies.

At the resolutions currently accessible, feedback models are subgrid by necessity (e.g. Agertz et al., 2013; Hopkins et al., 2013, 2018b; Keller et al., 2014).

Further, most feedback or ISM models are developed for eventual use in cosmological simulations (e.g. Springel & Hernquist, 2003). At the resolutions typically employed in cosmological simulations these methods fulfill their purpose and regulate the galactic star formation rate. However, many such methods struggle to retain the correct baryon content in galaxies, with either too much or too little ISM. In this sense, we are throwing the baby out with the bathwater; real galaxies are able to have regulated star formation without the complete destruction of the ISM.

Efficient supernova feedback destroys cold dense gas, or evacuates it from the disk entirely in outflows. Further, the accounting of energy and the thermodynamic state of the gas in some of these methods, particularly those that employ cooling shut-offs is incorrect. While this effectively regulates star formation, it removes our ability to truly study the ISM-star formation connection in galaxy simulations. This means there is a limited amount we can expect to learn about dense-gas cycling or GMC formation as it occurs in nature, on the full galaxy scale.

Designing feedback methods for use at the resolutions of isolated galaxies is difficult. As mentioned above, the high resolution causes the consequences of some sub-grid algorithms to manifest themselves and makes these methods resolution-dependent. Hopkins et al. (2014) and Hopkins et al. (2018a) state that their resolution is high enough to avoid these consequences. This can also be avoided by implementing sub-grid turbulence in the star formation recipe (Semenov et al., 2016). The superbubble feedback method of Keller et al. (2014) has been shown to converge as resolution is changed. This methods gives us a new opportunity to study the ISM in isolated galaxies with the inclusion of strong feedback.

In different phases of the ISM different heating mechanisms dominate. The interstellar radiation field (ISRF) dominates heating for gas below 10^4 K, at densities greater than 0.1 cm^{-3} (Tielens, 2005). This means that for warm and cold neutral gas FUV heating is the dominant heating process. This was a key assumption in Ostriker et al. (2010) and this was the first work to bring FUV heating in galaxies forward as a process to regulate star formation. Additionally, if we consider the energy budget of a typical stellar cluster, FUV radiation provides nearly two orders of magnitude more energy than supernovae or stellar winds (Starburst99, Leitherer et al., 1999). The long mean free path of FUV radiation means that it behaves differently in the ISM to other types of feedback. Whereas gas that has been heated by supernovae can leave the disk in an outflow, FUV heated gas remains in the ISM.

For all of these reasons, combining both supernovae feedback and FUV heating provides simulations with a new dimension to explore. However, feedback that involves FUV heating is not commonly employed. If radiative transfer is not available, FUV radiation can be included as a background heating rate or tied to the larger cooling code (e.g. Kim et al., 2011; Benincasa et al., 2016; Hu et al., 2017). In this sense, though, it is not self-consistent, unless it is tied to the star formation rate as in Kim et al. (2011). The inclusion of self-consistent FUV heating is the best way to quantify its role in regulating star formation.

In this work, we use radiative transfer to implement self-consistent FUV heating in our simulations. For the first time, we explore the impact of this FUV heating in combination with supernova feedback on the ISM in isolated galaxies. The remainder of the work is laid out as follows. In section 4.2, we describe our chosen galaxy model, a modification of the isolated disk test cases used in the AGORA comparison project. We then contrast different combinations of feedback choices and their roles in setting different galaxy and ISM properties in section 4.4. Finally, in section 4.5 we consider the impact of FUV heating on the star-forming ISM and search for signatures of this in the GMC population.

4.2 Galaxy Model

We use an isolated galaxy to explore the effectiveness of FUV heating in combination with supernovae feedback. For our isolated galaxy, we use a modified version of the initial conditions from the AGORA High-resolution Galaxy Simulations Comparison Project (Kim et al., 2014, 2016). The galaxy has a live stellar disk and bulge, as well as a live dark matter halo. The dark matter halo has an NFW density profile (Navarro et al., 1997). The halo has $M_{200} = 1.074 \times 10^{12}$ $M_\odot$ and a halo concentration parameter, $c = 10$. The stellar disk is modelled with an exponential density profile and has total mass of 3.438×10^{10} $M_\odot$. The stellar bulge has a total mass of 4.927×10^9 $M_\odot$ and follows a Hernquist profile (Hernquist, 1990).

We begin with the lowest resolution initial condition in the set, but then split each particle 64 times to increase the resolution. The dark matter halo has 6.4 million particles, each of mass 1.956×10^5 $M_\odot$. The stellar disk and bulge combined have 7.2 million particles, each of mass 5360 $M_\odot$. The gas disk is composed of 6.4 million particles, each of mass 1342 $M_\odot$. We employ a gravitational softening length of 80 pc.

It is advantageous to have a community IC available for use. Many studies outside of the AGORA comparison project have already used this IC for science (e.g. Agertz & Kravtsov, 2015; Grisdale et al., 2017, 2018; Semenov et al., 2017, 2018). A community IC saves considerable time in the development stage. As well, it makes comparison between different numerical studies addressing the same astrophysical problem much easier for the reader. That being said, community ICs can come with disadvantages. In particular, this galaxy has a significantly higher surface density than values typically measured for the Milky Way, which it is meant to model (e.g. Nakanishi & Sofue, 2016). However, as discussed in the following sections, this is still in the typical range for normal spiral galaxies.

The AGORA IC shares many similar characteristics with NGC5055, the sunflower galaxy. In Figure 4.1 we plot a comparison of the gas and stellar surface density in our simulations to those of NGC 5055. The total gas surface density is a combination of THINGS HI (Walter et al., 2008) and H_2 as measured by HERACLES CO (Leroy et al., 2009). The stellar surface density is from the GALEX nearby galaxy survey as reported in Leroy et al. (2008). Both of these simulated quantities show good agreement to the observational data, within 10 kpc. For the stellar surface density, there is a systematic difference; the observed stellar surface density is $\sim 30\%$ higher than in our galaxy. These radial distributions, especially

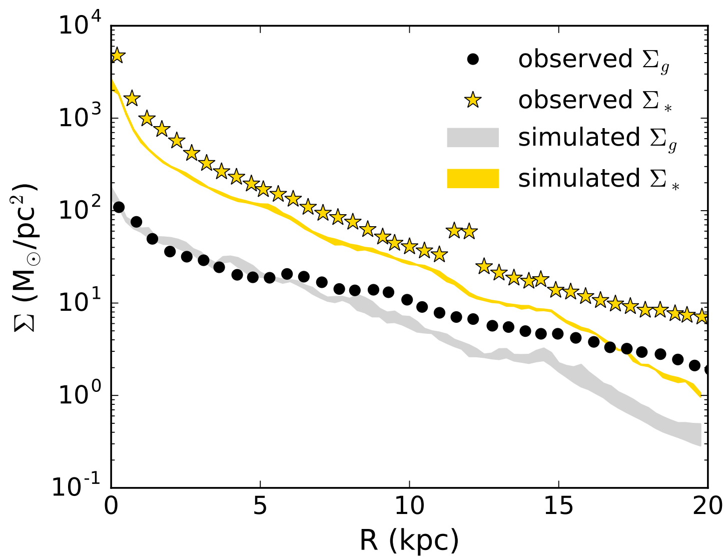

Figure 4.1: A comparison of surface density profiles
A comparison of our simulated galaxy surface density to the gas surface density of the sunflower galaxy, NGC5055. The grey bar shows the range of simulated Σ_g and the yellow bar the range of simulated Σ_*, measured after 200 Myr of evolution. The filled circles show the total gas surface density, Σ_{HI+H_2} as reported in Bigiel et al. (2008). The filled stars show the total stellar surface density as reported in Leroy et al. (2008). Our galaxies show good agreement with NGC 5055, within 30%, until the outer regions of the disk (R $\gtrsim 10$ kpc).

the stellar distribution, are potentially important quantities in determining the outcomes of galaxy scaling relations (Ostriker et al., 2010).

4.3 Methods

We simulate a suite of galaxy disks to study star formation in the context of the full galactic environment. We use the modern SPH code GASOLINE (Wadsley et al., 2004, 2017). As demonstrated in Wadsley et al. (2017), modern SPH, as employed in GASOLINE, performs particularly well for supersonic, turbulent gas such as that present in disk galaxies. The simulations employ star formation, feedback and metal cooling following the standard prescriptions presented in MUGS2 (Keller et al., 2015). These models have been successful in producing realistic disk galaxies, including stellar content over cosmic time, in cosmological zoom-in simulations (Keller et al., 2016). A new component in this work is the inclusion of radiative transfer to implement self-consistent FUV radiation from young stars throughout the entire disk.

4.3.1 Radiative Transfer

We employ the radiative transfer algorithm TREVR as detailed in Grond et al. (in prep.) and Woods (2015). TREVR is a novel, tree-based algorithm for computing radiation fields. The algorithm is flexible and computationally inexpensive when compared to other common radiative transfer approaches. In this study, we use TREVR to compute the FUV flux emitted by young stellar particles estimated using Starburst99 (Leitherer et al., 1999). The radiation field is modelled as a single FUV band with an opacity of 300 cm^2/g. This is the first time this has been done on-the-fly in a full galaxy disk simulation.

Table 4.1: List of simulation details

name	superbubble	FUV	E_{SN} (ergs)	n_{SF} (cm^{-3})
FB50	✓	✗	5×10^{50}	100
FUVFB50	✓	✓	5×10^{50}	100
FB10	✓	✗	10^{50}	100
FUVFB10	✓	✓	10^{50}	100
FUV*	✗	✓	none	100

4.3.2 Feedback

We employ the superbubble feedback method as detailed in Keller et al. (2014). As previously discussed, many feedback algorithms are developed for implementation on the cosmological scale. This can cause problems when these methods are then scaled down to use in isolated galaxies, where the resolution can be higher. Prior work has included many parameters to tune the strengths of winds, decay times or efficiencies. One of the many advantages of the superbubble method is that it requires no tuneable parameters. In this work, as in Benincasa et al. (2016) we are interested in how varying feedback parameters, i.e. the level of support, changes the ISM. For this reason, we use two different feedback strengths, 50% and 10% of the fiducial value, or 5×10^{50} ergs and 10^{50} ergs respectively. The feedback strength gives the amount of energy a superbubble event will inject into the ISM. For comparison, in MUGS2 (Keller et al., 2015) a feedback energy of 5×10^{50} ergs was used.

In cosmological zoom-in simulations, the structure of the ISM is not a primary concern as long as the overall star formation rate is correct. Early runs indicated that the strong supernovae feedback was highly destructive to the ISM in a manner that suggested too much of the kinetic energy was being deposited there. These issues have long been a concern for galaxy simulations where the hydrodynamic impact of feedback has been deliberately limited in the ISM (e.g. Springel

& Hernquist, 2003). The lower SN energy run is intended to simulate a scenario where a higher fraction of the SN feedback vents directly to the hot halo. As noted in section 4.5.1, we have evidence to support this choice is well motivated. As noted above, we regard these simulations as exploratory, covering the range of possibilities.

4.3.3 Star Formation

We use a common star formation prescription, where stars form following a Schmidt law:

$$\frac{\mathrm{d}\rho_*}{\mathrm{d}t} = c_* \frac{\rho_g}{t_{dyn}}, \tag{4.1}$$

where ρ_* is the density of new stars formed, ρ_g is the density of eligible gas, $t_{dyn} = 1/\sqrt{4\pi G\rho_g}$ is the dynamical time and c_* is the chosen efficiency. Gas is considered eligible for star formation if it lies above a set density threshold, lies below a maximum temperature and belongs to a converging flow. This is a typical star formation method (e.g. Katz, 1992). The temperature we now use compares the total effective temperature of gas particles, not just their thermal component. This ensures that feedback is able to locally limit star formation. Further, particles that are currently in a two phase state cannot form stars. We assume that these particles, near recent star formation events, are analogous to unbound GMCs.

4.4 Results

4.4.1 Galaxy Properties

We begin by considering the basic properties of the galaxies in our suite (setups detailed in table 4.1). As a first diagnostic, we can consider the visual appearance

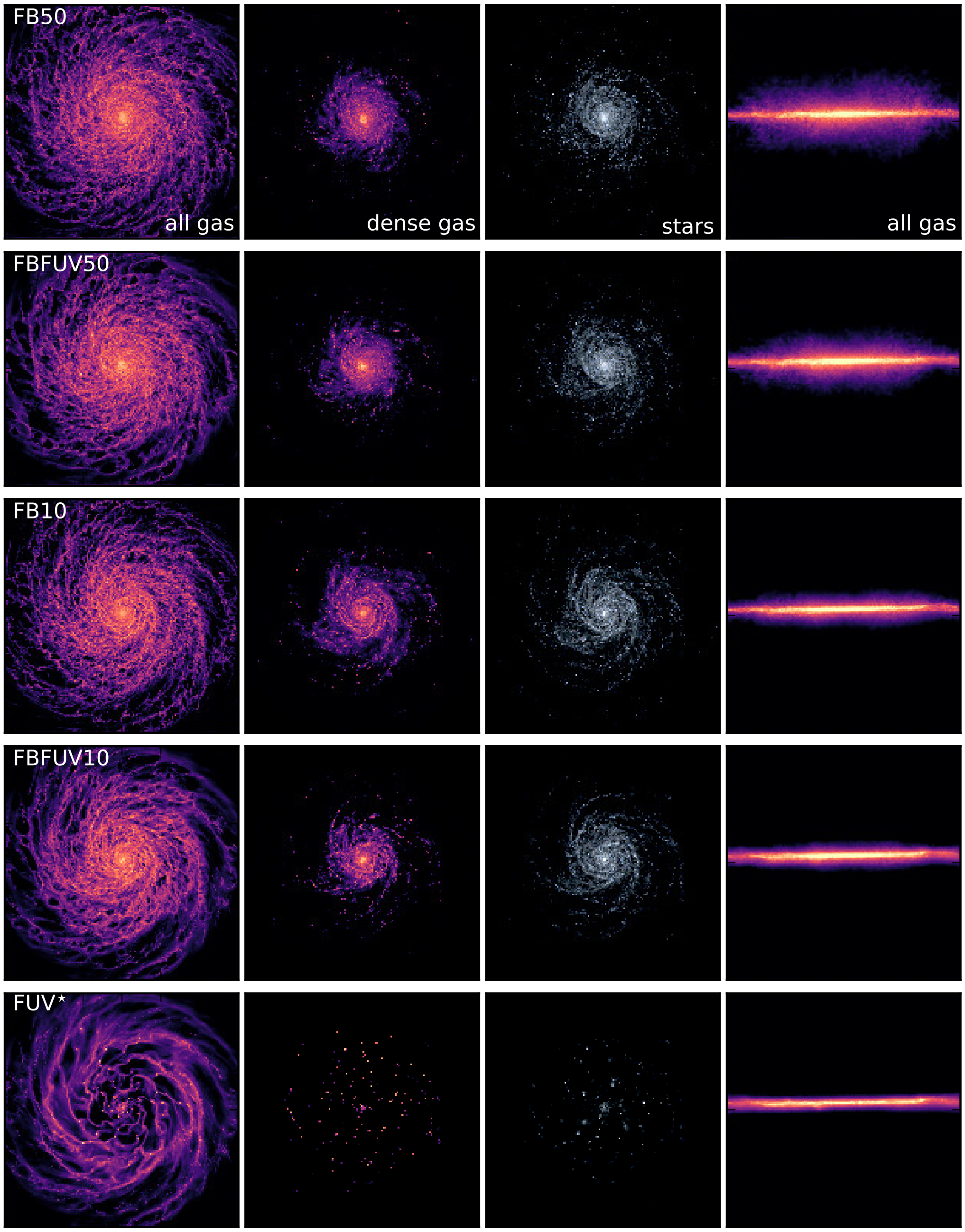

Figure 4.2: Surface density maps of the galaxies in our sample
These surface density maps are taken from snapshots at 200 Myr of evolution and the maps are 30 kpc across in both dimensions. *Left:* Total gas surface density. *Middle-Left:* Dense gas surface density. *Middle-Right:* Young stellar luminosity map; here young stars have formed less than 100 Myr in the past. *Right:* Side-on total gas surface density. In the gas surface density columns, the colour-scale runs from 1 $M_\odot/pc^2$ (black) to 500 $M_\odot/pc^2$.

of the galaxies. Figure 4.2 shows face-on and side-on images for different quantities of interest. The left-most panel shows the total gas surface density of the disk. The second panel shows the gas surface density of the disk when considering only gas above 100 cm^{-3}. The third panel shows a synthetic stellar map. To simulate FUV observations we show only stars that have formed in the last 100 Myr (Salim et al., 2007; Murphy et al., 2011; Kennicutt & Evans, 2012). The left-most panel shows a side-on gas surface density for the disk, a visual representation of the scale-height.

In the left-most panel of Figure 4.2, the total gas surface densities are plotted for each of the galaxies after 200 Myr. Each of the galaxies develops some type of flocculent spiral structure. However, this spiral structure is more apparent when the superbubble feedback energy is decreased, in cases FB10 and FUVFB10. The inclusion of FUV heating also appears to boost the presence of the spiral structure; the case FUVFB10 has the most apparent spiral structure. Already, just from a visual standpoint, it seems that FUV heating alone is not sufficient. The case FUV$\star$ shows a large degree of fragmentation.

In the second panel of Figure 4.2 the surface density of dense gas is shown; we consider gas to be dense once it has exceed 100 cm^{-3}, which is the typical density of GMCs. Again, the case with only FUV heating appears to be over-fragmented. If we focus on just the four cases that contain FUV heating and superbubble feedback there are subtle differences which track the differences in the total gas surface density. When the feedback energy is high, FB50 and FUVFB50, the structure is very flocculent and there appears to be almost no spiral structure in the dense gas. When this energy is lowered, FB10 and FBVU10, the dense gas organizes along the spiral features. The addition of FUV heating on top of superbubble feedback in this case appears to eliminate some of the diffuse structure in the outer portions of the galaxy. This is most prevalent when comparing FB10 and

FUVFB10.

The third panel of Figure 4.2 shows synthetic stellar maps for each of the galaxies. To simulate stellar emission as traced by FUV radiation, we show only stars that have formed in the last 100 Myr (Salim et al., 2007; Murphy et al., 2011; Kennicutt & Evans, 2012). In general the recent star formation aligns well with the positions of dense gas. Again, FUV$\star$ does not have the expected structure; it displays no spiral structure and contains a dense stellar nugget at its core. We now consider the remaining four cases, where we see similar trends to those seen for the gas. Again, the spiral arms are most apparent in the two cases with lower feedback energy. With the addition of FUV heating on top of this the star formation becomes even more concentrated to the spiral features (see case FUVFB10). For all four of these cases, the star formation falls off rapidly in the outer regions of the disk even though there is still significant total gas in these outer regions. This truncation is a point we will return to in later sections.

Lastly, the fourth panel of Figure 4.2 shows the side-on surface density. The galaxies with superbubble feedback alone have larger scale heights. As expected, decreasing the strength of the superbubble feedback decreases the apparent scale height. Interestingly, adding FUV heating on top of the superbubble feedback decreases the apparent scale height.

We can see visual cues suggesting how the star formation is distributed or regulated in Figure 4.2. The global star formation rate for each of the galaxies is plotted in Figure 4.3. This figure shows concrete evidence for what is suggested in Figure 4.2, FUV heating alone cannot regulate star formation. When FUV heating is the only source of feedback, the star formation rate only begins to decrease as the galaxy consumes fuel. The cases with both FUV heating and superbubble feedback do show regulated star formation. Each of these cases does show an early burst

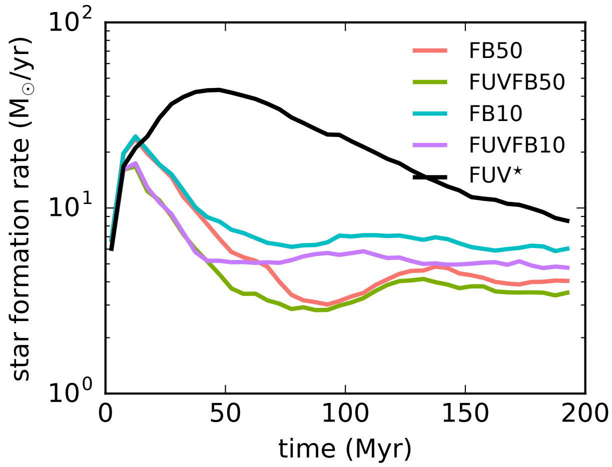

Figure 4.3: The global star formation in the simulated suite
The global star formation rate in each of our galaxies. In all of the galaxies that include both superbubble feedback and FUV heating, there are only small changes in the star formation rate. However, when the only form of feedback is FUV heating, there is a dramatic increase in the amount of star formation. This galaxy can only decrease its star formation rate by consuming a significant amount of the star-forming fuel.

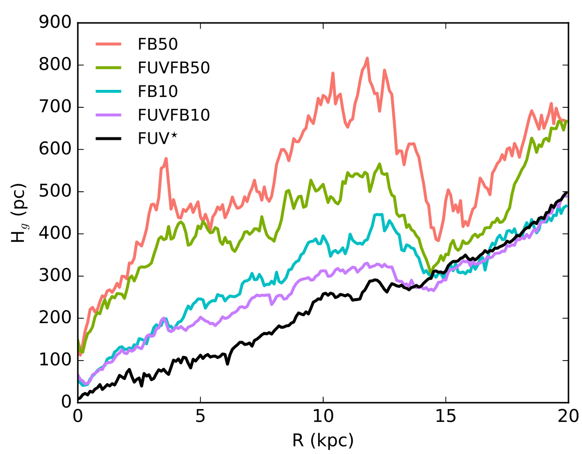

Figure 4.4: The gas scale height in the simulated suite
The gas scale height in each of the galaxies. The addition of superbubble feedback creates galaxies with the largest scale heights.

in star formation, however, the rates quickly turn over after 50 Myr. As expected, the cases that have higher feedback energy have lower star formation rates. Further, adding FUV heating on top of superbubble feedback results in only a small decrease to the star formation rate; less than a factor of two.

The gas scale height for each of the galaxies is plotted in Figure 4.4. These scale heights are as expected from visual inspection of the side on projections shown in right-most panel of Figure 4.2. The cases that have the lowest star formation rates have the highest scale heights. Further, of these two cases, having FUV heating causes a decrease in the scale height, even though it cases a decrease in the star formation rate as the role for superbubble is decreased. Referring back to Figure 4.3, the simulations with 50% feedback energy, the highest in the suite, have the lowest star formation rates. Conversely, these runs also have the highest scale heights. This is because the superbubble feedback energy is responsible for inflating the disk and causing outflow.

The last thing we consider in this section is the FUV intensity in each of the simulations that employ FUV heating. This FUV intensity, as well as the gas and star formation rate surface density, is plotted in Figure 4.5. In these plots the green line shows the gas surface density, the orange line shows the star formation rate surface density, and the black line shows the FUV intensity felt by the gas. Firstly, the truncation of the star-forming disk is clearly visible here, even in the disk with only FUV heating. This truncation occurs in the same region as observed in Figure 4.2. Secondly, in the cases that include supernovae feedback, we can see that the FUV intensity does not share the same slope as the star formation rate, it is shallower. In the inner regions of the galaxy we expect the FUV intensity to track recent star formation. However, since the mean free path of the FUV radiation is long, $\sim$1 kpc, radiation from the inner regions of the galaxy can easily diffuse

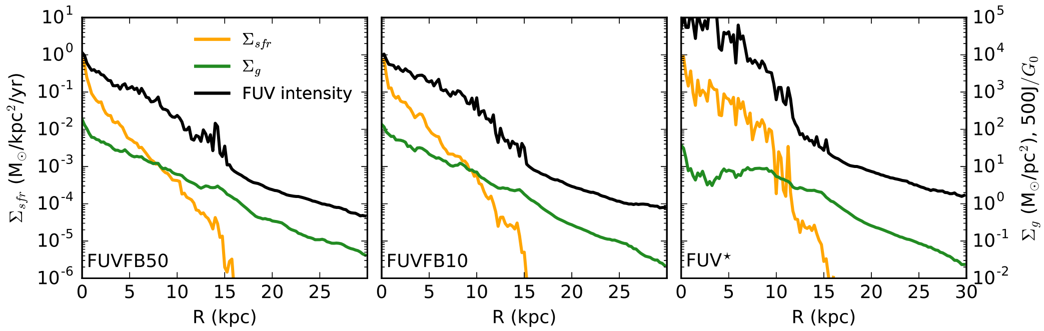

Figure 4.5: The simulated FUV intensity
The gas surface density, star formation rate surface density and FUV intensity for three of our simulations. As the star formation rate is increased, so is the FUV intensity felt by the gas.

outward. This leads to a boosted intensity in the outer edges of the galaxy, thus changing the slope as observed.

4.4.2 The Role of Pressure

Pressure is inherently connected to the evolution of star-forming disk galaxies. Pressure facilitates the regulation of star formation and it is connected to the dense gas fraction (Blitz & Rosolowsky, 2004, 2006; Ostriker et al., 2010). Galaxy simulations are an ideal tool to study the role of pressure in the cycle of star formation. Following the approach Benincasa et al. (2016) we explore the pressure balance in our galaxy disks in this section.

The star formation rate in a galaxy is set by the balance between the pressure required and the pressure support. The level of pressure required is set by the gravity of the disk:

$$\begin{aligned} \mathrm{P_R} &= \mathrm{P}_{dm} + \mathrm{P}_g + \mathrm{P}_* \\ &= \frac{1}{2}\Omega^2\Sigma_g \mathrm{H}_g + \frac{1}{2}\pi G \Sigma_{\mathrm{g}}^2 + \pi G \Sigma_g \Sigma_* \left(\frac{\mathrm{H}_g}{\mathrm{H}_g + \mathrm{H}_*}\right) \end{aligned} \tag{4.2}$$

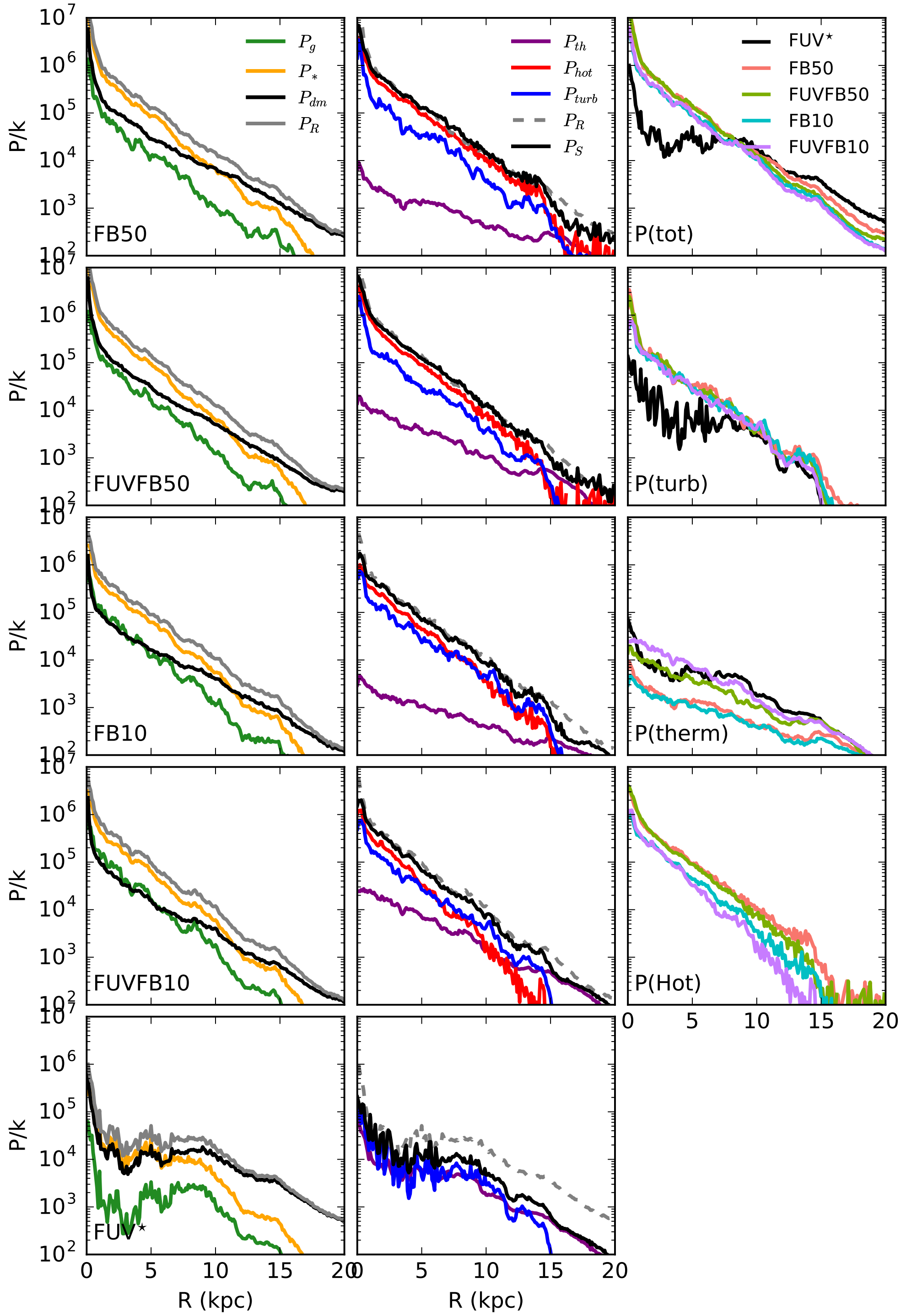

Figure 4.6: Comparing the different relevant pressure terms in each of the galaxies.

where Ω is the shear rate, Σ_g is the gas surface density, H_g is the gas scale height, Σ_* is the stellar surface density and H_* is the stellar scale height. A discussion of the detailed assumptions that have gone into deriving these terms can be found in Benincasa et al. (2016).

The pressure support we measure in the disk is calculated by:

$$\begin{aligned} \mathrm{P_S} &= \mathrm{P}_{th} + \mathrm{P}_{hot} + \mathrm{P}_{turb} \\ &= \frac{\Sigma_\mathrm{g}}{2\,H_g}\left(\frac{2}{3}u_\mathrm{th} + \frac{2}{3}u_\mathrm{fb} + v_z^2\right)_{z=0}. \end{aligned} \tag{4.3}$$

This is the mid-plane support and so all these quantities take on their mid-plane values. The mid-plane density, $\rho_{\mathrm{g},0}$, is well approximated by the gas surface density divided by twice the gas scale height, H_g. In this work, thermal pressure originates from FUV radiation and the dissipation of gas motions. In eqn. 4.3, the hot gas pressure we refer to originates from the superbubble heating.

In Figure 4.6, we plot all of these quantities for the simulations in the suite. The terms that go into calculating the pressure required, eqn 4.2, are plotted on the left and the pressure support, eqn 4.3, in the middle panel. In the right panel of Figure 4.6 we plot a selection of these quantities such that they can be compared between the simulations. In this case we plot the total pressure, the feedback pressure, P_{FB}, and the thermal pressure, P_{th}.

We first consider the pressure required from the gravity of the gas, stars and dark matter. In the left column of Figure 4.6 the only quantity that changes appreciably is the pressure required from the gravity of the gas, P_g. As the feedback energy is decreased, moving downward in the left column of Figure 4.6, P_g increases. This change happens in a relative sense; it is due to a decrease in the scale height rather than a change in the gas surface density. This happens because as the feedback energy is decreased, the gas begins to contribute more and more to the dynamics of the galactic disk; the case FUV$\star$ shows an extreme case of this situation. The agreement between P_S and P_R becomes noisier as the relative importance of P_g increases. We can say that as gas plays a larger role in the dynamics of the galaxy, it becomes more and more difficult to make predictions about pressure balance.

This behaviour can be seen in the galaxies in Benincasa et al. (2016). Those galaxies were evolved in static potentials, thus they had no live old stellar or dark matter component. The dynamics of the galaxy, and the pressure, were heavily influenced by the gas. In that study, the only way to see dynamical pressure balance was to average the quantities over 100 Myr. In this study, however, the stellar disk and dark matter halo provide the main gravitational requirement and it is much easier to observe pressure balance.

Next we consider the pressure support, plotted in the middle panel of Figure 4.6. In this case we can investigate the role of different types of feedback. The addition of the FUV heating through radiative transfer means that this heating can be self-consistent. Rather than a global or radial implementation, it can actually occur as a result of recent star formation. This means that when we add FUV heating, the level of thermal pressure actually increases (see case FUVFB50 and FUVFB10 in Figure 4.6). Each of the different simulations in the suite have a similar amount of turbulent pressure and only small variations in the hot gas pressure.

This comparison can be made more quantitatively in the final column of Figure 4.6. There are only small differences in the total pressure for the different galaxies. In these galaxies, the total pressure required is dominated by the old stellar disk in the inner regions and the dark matter component in the outer regions. We do not expect the total pressure to change appreciably when we change the feedback. This changes when we consider the case with only FUV heating though. As discussed earlier, the gas plays a much larger role in this case, especially in the inner regions of the galaxy. Thus, we start to see variations from the expected total pressure.

The turbulent pressure, similar to the total pressure, shows little change between the four main galaxies (those with both FUV heating and superbubble feedback). Interestingly, even without the stirring provided by the superbubble feedback, FUV$\star$ still shows a comparable amount of turbulent support to the others. The level of thermal pressure depends on the presence of FUV heating and the star formation rate. When no FUV heating is used, thermal pressure originates from the background heating in the disk. The level of thermal pressure is the same for cases FB50 and FB10. The cases with FUV heating have more thermal pressure, and of these cases, the cases with higher star formation rates have proportionately higher thermal pressure. There is similar reasoning when we consider the feedback pressure; cases with higher feedback energy have higher feedback pressure.

In the pressure balance model, the star formation rate is directly controlled by the amount of pressure support. In this way, the star formation rate should increase when there is a need to produce more pressure support and maintain dynamic pressure equilibrium. We can reconcile this with our results by first considering the two galaxies with only superbubble feedback, FB50 and FB10.

When the superbubble feedback energy is increased, the star formation rate conversely decreases. We can understand this change by considering the pressure. The two galaxies are otherwise the same: they have the same dark matter halo, old stellar population and gas disk distribution. Looking at Figure 4.3 we can see that initially the star formation rates are the same. However, once the new generations of stars begin to undergo supernovae, the galaxy with the higher feedback energy produces more thermal pressure in the form of P_{fb}. To maintain the pressure balance, this means that the star formation rate must decrease.

This picture is slightly different when we consider the case with FUV heating and no superbubble feedback, FUV*. This is the only galaxy where we do not see pressure equilibrium. This disagreement is established early and the imbalance is already in place after 50 Myr. The FUV heating by itself is unable to regulate the star formation rate. This results in a very high level of gas consumption, and the fragmentation of the remaining gas into dense knots. This significantly alters the distribution of gas throughout the disk. The galaxy has formed too many stars, which results in an imbalance. However, the way to correct this imbalance would be to use feedback to provide more pressure support. In this case, the feedback is not effective, the pressure equilibrium appears to be destroyed. However, the scaleheight for this galaxy, shown in Figure 4.4 is smaller than all of the other galaxies: less than 100 pc in the inner regions of the disk. At this scaleheight, we are approaching the resolution limit set by the gravitational softening. Thus, this pressure disagreement requires further investigation.

4.4.3 The properties of the simulated ISM

Following the discussion of pressure in section 4.4.2 we are interested in how the inclusion of FUV heating impacts the structure of the ISM. To quantify the nature of the ISM we begin by looking at how the mass in the ISM is divided into different phases. We make divisions for these ISM phases as follows. Hot gas is any gas above 10^5 K and this gas has most likely been heated by superbubble feedback. Warm gas is any gas between 10^5 K and 2000 K. Cold gas is any gas below 2000 K. FUV is the dominant heating mechanism for any gas that has not been heated

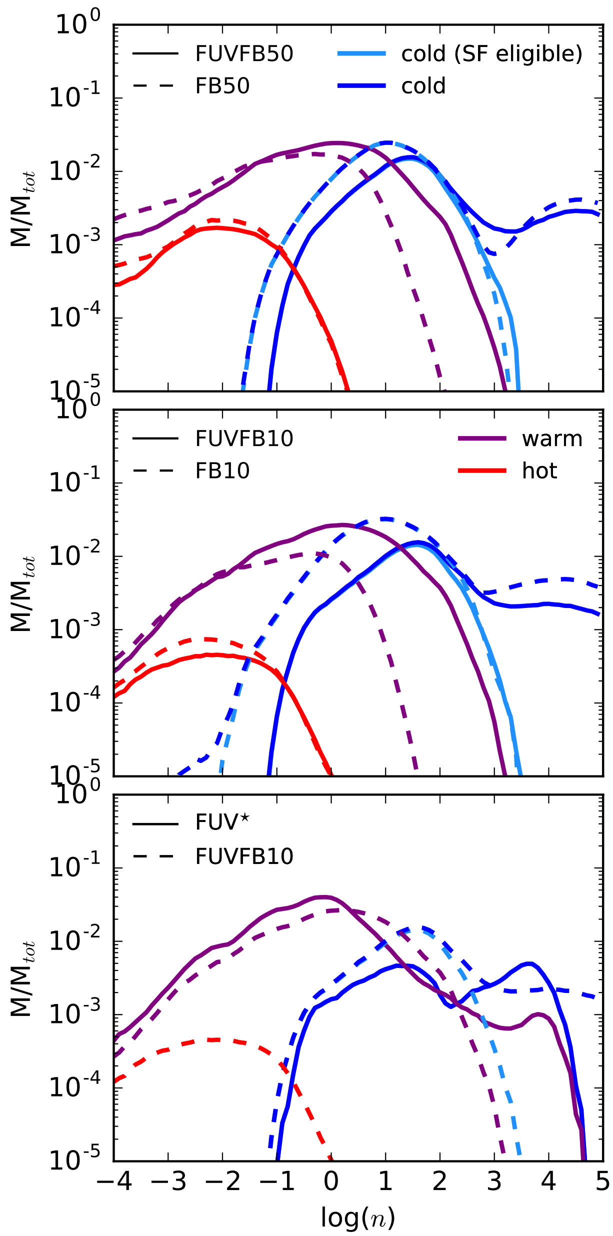

Figure 4.7: The distribution of the ISM phases in our simulated galaxies Histograms of the mass in density bins for each of the simulations. For comparison of the different ISM phases we separate the gas into three temperatures phases. Cold gas is any gas below 2000 K, warm gas is any gas between 2000 and 10^5 K and hot gas is any gas above 10^5 K.

by feedback. We add an additional category, cold gas which is eligible for star formation. This is any gas below 2000 K which has not been heated by superbubble feedback. This gas forms stars if its density exceeds 100 cm^{-3}.

The first type of histogram we consider is binned by density, as shown in Figure 4.7. The panels are separated by the strength of the superbubble feedback energy and in the bottom plot we compare FUV heating only to a simulation with FUV heating and weak superbubble feedback. The first noticeable difference is in the amount of warm gas: the inclusion of radiative transfer appreciably changes the distribution of warm gas. The peak of the warm gas distribution remains at $n \sim 0.3$ cm^{-3} in all cases. This agrees with the predicted average density of the warm neutral phase of the ISM of ~ 0.5 cm^{-3} (Tielens, 2005). However, when FUV heating is added on top of superbubble feedback there is more warm gas at higher densities. This can be quantified by looking at the maximum density of the warm phase gas in each case. Considering the top two plots, adding FUV heating increases the maximum density of the warm phase gas by 1-2 orders of magnitude.

While the FUV heating does significantly change the distribution of warm gas, this is not the case for the distribution of cold gas. There is a decrease in the amount of cold diffuse gas when the FUV heating is added (see cases FUVFB50 and FUVFB10). However, if we consider the gas labelled as cold and eligible for star formation, there is negligible difference. *This is an important distinction; FUV heating impacts the phase out of which star-forming gas will condense. This is in contrast to supernovae feedback, which directly impacts the phase of gas that is already eligible for star formation.*

Next we consider the radial distribution of each phase throughout the galaxy in Figure 4.8. In this configuration, the differences between cases are more subtle. Again, when FUV heating is added on top of superbubble feedback the fraction

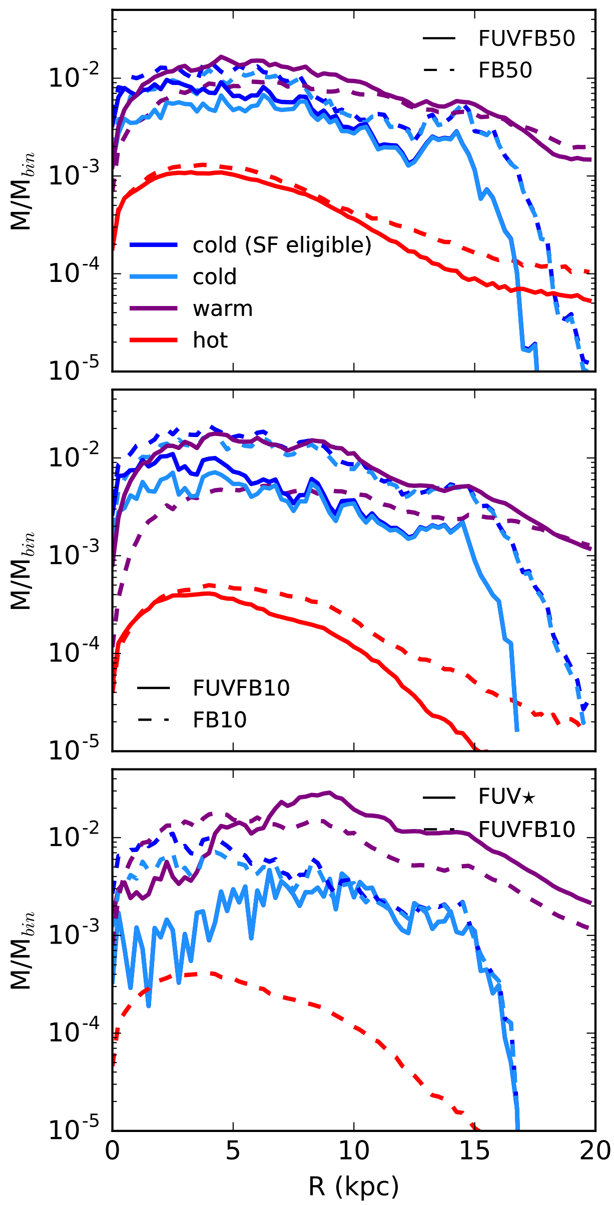

Figure 4.8: The radial phase distribution in our simulated galaxies Histograms of the mass in different phases as a function of radius. The temperature phase divisions are made as in Figure 4.7.

of warm gas significantly increases. This increase is most visible when comparing FUVFB10 and FB10, in the middle plot. Also, we can again see that the FUV heating moves gas from the cold phase into the warm phase.

However, again, if we look at the case with only FUV heating the picture is different. Here there is no hot gas produced, and there is an order of magnitude less cold gas than in the other cases. When FUV heating is the only feedback, the only way for star formation to be regulated is for cold gas to be consumed. This is clear in the deficit of cold gas in Figure 4.8.

The radial histograms reinforce that there are three phases of the ISM present at each galactic radius. This is the case until between 10 - 15 kpc, where the cold phase begins to disappear. In this region of the outer disk the gas is mainly found in the warm phase. Referring back to Figures 4.2 and 4.5, this coincides with the edge of the star-forming disk. As mentioned before, this is interesting given that there is still a significant gas surface density present. This transition to a dominant warm phase is thought to be the reason for the truncation of star formation (Elmegreen & Parravano, 1994; Schaye, 2004).

The radial histograms suggest that FUV is able to heat gas effectively in the outer regions of the galaxy. In Figure 4.8, in the regions outside 15 kpc in all three panels, the FUV heating is able to create warm gas. The FUV heating is actually able to truncate the star-forming disk earlier than the superbubble feedback. This suggests that it is possible to explain the truncation of star formation without the presence of supernovae feedback. This is particularly reinforced by the bottom panel, comparing a case with FUV heating and superbubble feedback, to a case with superbubble feedback only. In these two cases there is exactly the same amount of cold gas in the outer disk.

There is a minimum thermal pressure required to maintain a two-phase ISM, where the phases in question are warm and cold (Field et al., 1969). This state is regulated by the thermal balance between heating and cooling in the ISM (Wolfire et al., 1995, 2003). Wolfire et al. (2003) calculated this minimum pressure for the Milky Way. In Figure 4.9 these minimum pressures are plotted to compare to the thermal pressures in our simulated galaxies. For the simulations, we take the thermal pressure to be a combination of the hot gas pressure ($P_{\rm hot}$) and what we call the thermal pressure. The simulated thermal pressure does start to dip below this minimum pressure between 10 - 15 kpc. This coincides with where we see the cold phase begin to disappear.

There are many assumptions that go into this minimum pressure calculation. Most importantly, this only holds in regions where the thermal pressure is the dominant source of support. In our galaxies, because of the effectiveness of the superbubble feedback, thermal pressure in some form dominates at almost all radii. However, further out in the disk, the two contributions become comparable. To make a definitive statement about this pressure requirement, more investigation is needed. In the Milky Way, for instance, the pressure requires that there be some amount of cold neutral medium present out to $\sim$18 kpc.

4.5 The star-forming ISM

The Kennicutt-Schmidt relation is an empirical relation used to characterize the star-forming ISM in galaxies. In Figure 4.10 we plot the Kennicutt-Schmidt relation for the simulated galaxies, compare to a selection of observational data. The data for NGC 5055 as presented in Bigiel et al. (2008) and Leroy et al. (2008) is plotted as the black crosses. The contours in Figure 4.10 show locally measured data from different surveys. The coloured contour shows the space occupied by the galaxies

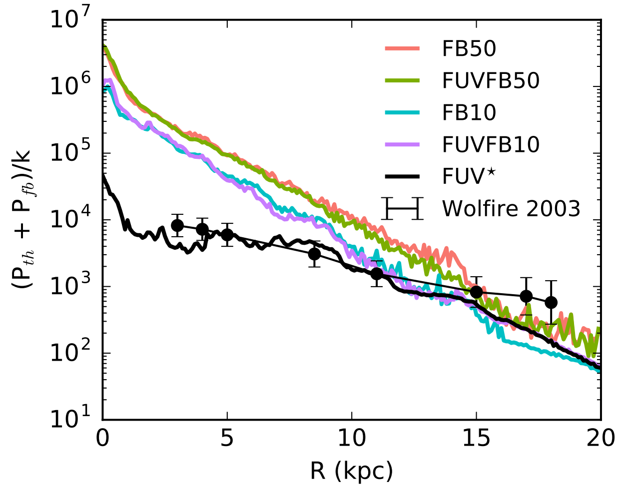

Figure 4.9: Thermal pressure in the ISM
The total thermal pressure in our simulations compared with the minimum pressure required to maintain a two-phase medium as calculated for the Milky Way in Wolfire et al. (2003). Most of our simulations remain above this line until $\sim 10-15$ kpc, the point at which star formation truncates as seen in Figures 4.2 and 4.5.

reported in Bigiel et al. (2008); these measurements are taken at 750 pc scales. In the top row we compare to the entire sample, whereas in the bottom row we compare specifically to NGC 5055. The small circles show local measurements of M51 as reported in Kennicutt et al. (2007); these measurements are taken on 300 pc scales. The simulated galaxies are plotted as the different open symbols. These measurements are taken in 500 pc radial annuli, to agree with the resolution of the radial measurements reported in Leroy et al. (2008). For the star formation rate surface density we consider only the stars that have formed in the last 100 Myr. Additionally we take only measurements outside a galactic radius of 2.5 kpc.

Our data agree with the observational trend. We find that the types of feedback chosen cause subtle changes in the positioning of data on this diagram. This only holds if FUV heating is not the only form of feedback chosen. The relation for the case FUV$\star$ further shows that FUV heating along cannot regulate the star for-

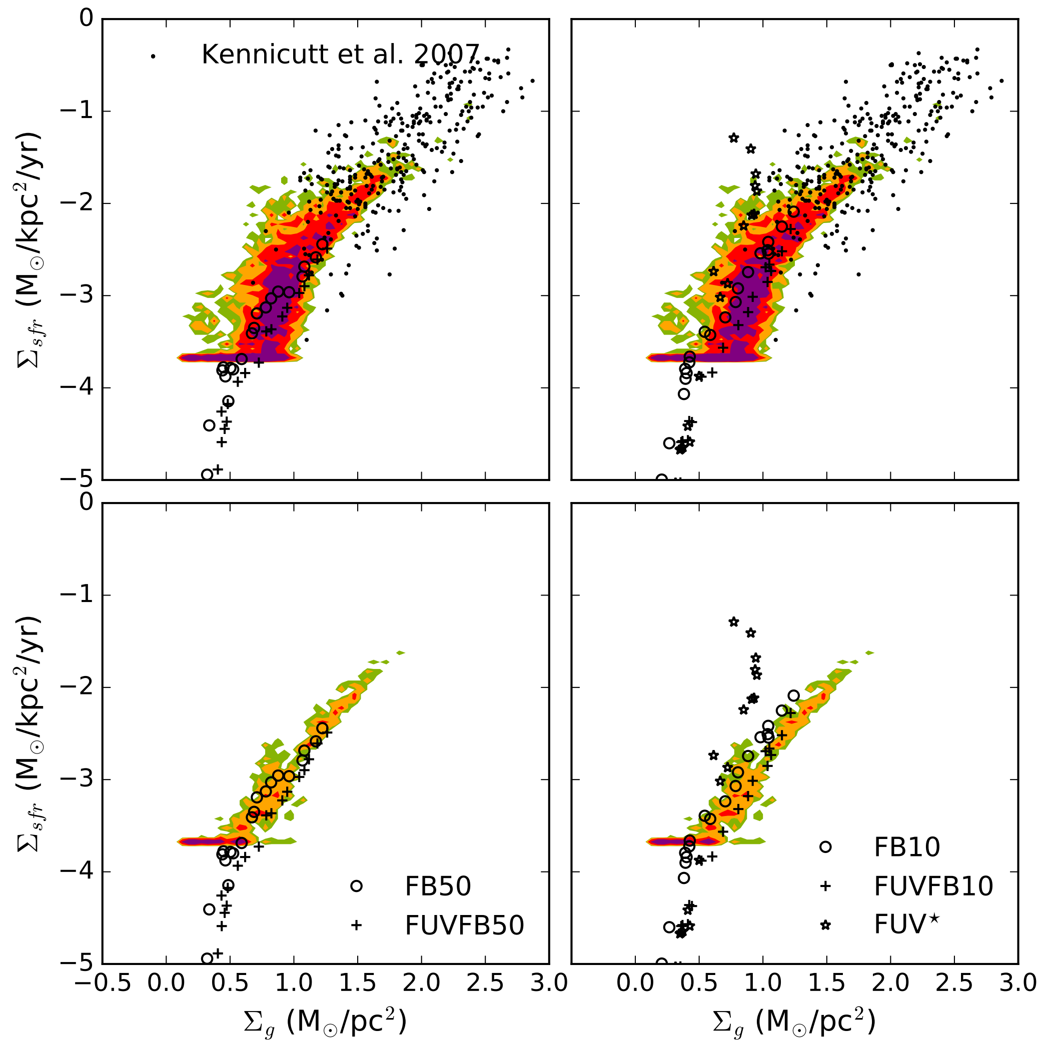

Figure 4.10: The Kennicutt-Schmidt relation in simulated and observed galaxies The Kennicutt-Schmidt relation for our simulated galaxies compared to observational samples. The black symbols show the five galaxies in our suite. For our data we plot only values for radii outside 2.5 kpc. In the top row the coloured contours show the space occupied by local measurements for all the THINGS sample; in the bottom row the contours show the space occupied by NGC 5055 (Bigiel et al., 2008). The dots in the top row show the local measurements in M51 from Kennicutt et al. (2007).

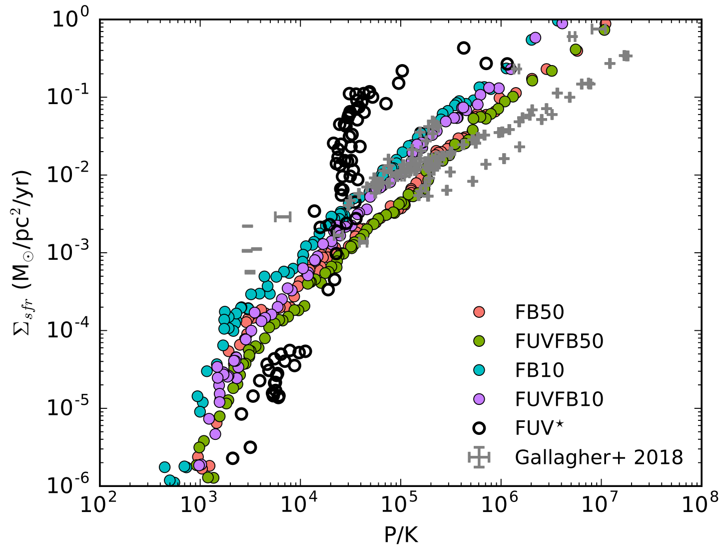

Figure 4.11: The relation between Σ_{sfr} and the pressure
A comparison of the pressure and Σ_{sfr} in our simulated galaxies to the recent observational sample of Gallagher et al. (2018).

mation rate. The relation between Σ_g and Σ_{sfr} is nearly vertical, such that pieces of the galaxy at the same Σ_g can have star formation rates that vary by an order of magnitude. This is in contrast to the assumptions of Ostriker et al. (2010) who assume that FUV is the critical regulator of star formation in the ISM.

We now move on to contrast the cases that have both types of feedback. As noted above, the differences here are subtle. It appears that the galaxies with only superbubble feedback provide the better fit. However, there are two caveats to consider before taking this agreement at face value. To discuss the first, we must go back to the radial distributions of Σ_g and Σ_* as presented in Figure 4.1. In these plots there is a 30% disagreement between the stellar surface density of NGC5055 and that of our simulated galaxies. The slopes are the same, but the NGC 5055 has a systematically higher Σ_* at each radius. There is an established connection between the stellar surface density and the pressure.

Referring back to Figure 4.6 and eqn 4.2, a higher stellar surface density implies a galaxy should have a higher total pressure. This is important because there is a connection between the total pressure and the star formation rate. This relation is demonstrated in Figure 4.11, which plots Σ_{sfr} as a function of the pressure. The galaxies in the suite with both FUV heating and superbubble feedback are plotted as the filled circles. The grey crosses denote the measurements of Gallagher et al. (2018) for nearby galaxies. There are debates as to what the expected slope of this relation should be, but there exists an overall relation; as the pressure is increased, the star formation rate should increase. This suggests that our galaxy, which has a lower Σ_* than NGC5055, would have a lower pressure and thus a lower star formation rate. This makes it less clear which galaxy actually provides the more realistic scenario in Figure 4.10.

The second caveat comes about if we inspect the slopes of the relations in Figure 4.10 more closely. In general, our galaxies have slopes that are steeper than the predicted relation. However, this is more complicated if we look to lower surface densities. In this regime the slope appears consistent. It should be noted that there can be systematic biases introduced in the way that pressure is calculated in observational studies; assumptions about the scale height and velocity dispersion must be made. This could lead to systematic offests.

Regardless of this, we posit that FUV heating is most important in the outer regions of disk galaxies. This can be reinforced by considering our galaxy with only FUV heating, FUV$\star$. This galaxy is a failed case in many ways. However, if we look to the Kennicutt-Schmidt relation, at the lower surface densities in the outer regions of the disk, the galaxy agrees with the expected relation. Again, this point requires further investigation. However, based on these first results, it appears that simulated galaxies require supernovae feedback for the inner disk and FUV heating

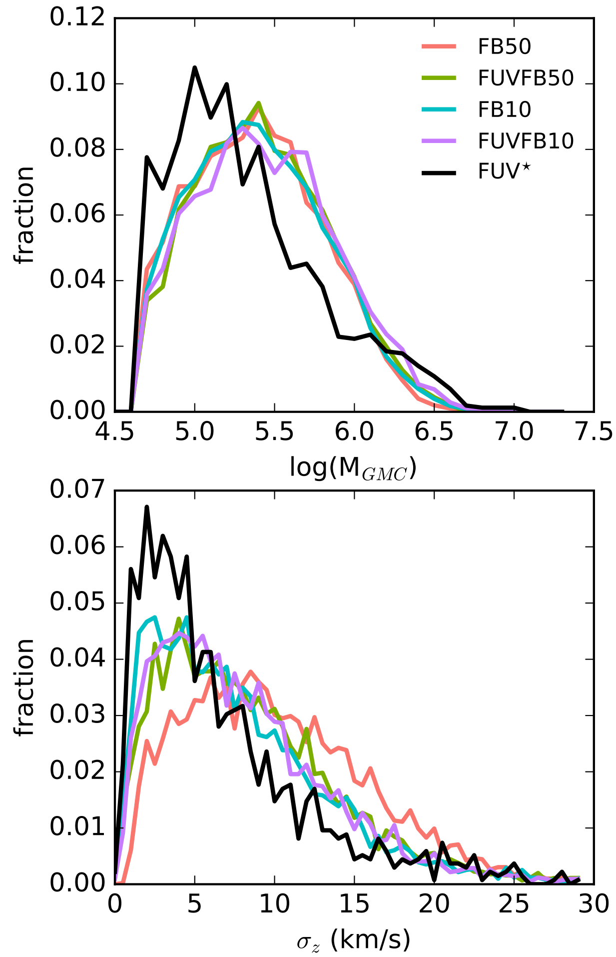

Figure 4.12: The GMC mass and velocity dispersion distributions for the galaxies in our simulated suite.

for the outer disk.

4.5.1 GMC properties

In reality, stars form in GMCs. In this final section, we consider the properties of GMCs in our galaxies to see if there is a significant difference from the introduction of FUV heating. We use the tool astrodendro to identify GMCs in our simulated galaxies. Astrodendro is an observational tool that uses dendrograms to identify structures in the gas. This method relies on few free parameters to identify structures; the minimum pixel number, the minimum surface density to be part of the tree, and the minimum division between levels in the tree. We did experiment with different choices for these parameters, but find good convergence regardless. In the end, we require only that clouds are composed of gas above $10\ \mathrm{M_{\odot}/pc^2}$ and that clouds are composed of a minimum of two pixels.

We consider two cloud properties in this work, the mass and the velocity dispersion, σ_z. These distributions can be seen in Figure 4.12. We could not find a detailed analysis of the molecular gas or GMCs in NGC 5055. In lieu of this, we compare to other nearby star-forming spiral galaxies. We focus our efforts on the nearby galaxy samples of Hughes et al. (2013), Colombo et al. (2014), Sun et al. (2018) and the Milky Way sample of Roman-Duval et al. (2010). Colombo et al. (2014) detail the results of the PAWS study of M51. Hughes et al. (2013) also feature this data of M31, in contrast with M33 and the Milky Way. Sun et al. (2018) detail the molecular clouds in 11 galaxies from the PHANGS-ALMA sample.

Our cloud velocity dispersions agree very well with the cloud sample of Hughes et al. (2013) and the molecular gas analysis of Sun et al. (2018). All the cases, excluding FB50, also agree with the Milky Way sample of Roman-Duval et al. (2010). In general, our high feedback only case produces too many clouds with high velocity dispersions. Our mass distributions peak at $\sim 3 \times 10^5\ \mathrm{M_{\odot}}$. This is an order of magnitude higher than the mean cloud mass found in the Milky Way (Roman-Duval et al., 2010). However, this median is in agreement with many extragalactic studies, for example M51 (Colombo et al., 2014).

When comparing the masses of of GMCs in different simulations, there is very little difference between the cases that have both types of feedback. This suggests that supernova feedback plays the larger role in setting the masses of GMCs.

This seems also to be the case for the velocity dispersion. The only significant difference is in the distribution with only strong superbubble feedback. However, a KS test cannot distinguish these as originating from separate distributions.

It is interesting that even in the case without strong superbubble feedback, FUV*, the GMC mass distribution still has a reasonable peak value for both the velocity dispersion and mass distributions. This suggests that FUV heating does play an important role in setting GMC properties and regulating the structure of dense gas.

4.6 Summary & Conclusions

For the first time we have simulated a full galaxy using a self-consistent treatment for FUV heating, implemented through radiative transfer. We have used these galaxies to explore the role that FUV plays when used in combination with supernovae feedback. We have found that FUV heating on its own is not sufficient to regulate star formation. In this case, really the only way for the galaxy to regulate its star formation rate is to consume all of the available fuel. This is in contrast to the Ostriker et al. (2010) picture, which assumes FUV heating dominates regulation.

The galaxy with only FUV heating has a considerable amount of turbulent support, showing that generating this turbulence does not require supernovae. This supports the findings of McNally et al. (2009) who suggest that shear and gravitational torques between dense structures in the ISM are sufficient to generate turbulence. This suggests that FUV is a good candidate for regulating star formation in the outer regions of galaxies, where it may be the culprit that sets the truncation radius of the star-forming disk.

In combination with the superbubble feedback, we see that the addition of

FUV heating has subtle but important impacts on the ISM. The inclusion of FUV heating leads to more defined spiral structure (see Figure 4.2). Further, it is able to help in regulating the star formation rate. We can see this when looking at the distribution of gas among the hot, warm and cold phases of the ISM. FUV heating is able to move gas out of the cold diffuse phase into the warm phase.

Our study of the star-forming ISM presents interesting insight into the use of empirical diagnostics to study the effectiveness of different feedback methods. As in Benincasa et al. (2016), we find that no one star formation or ISM diagnostic on its own can tell the whole story. The Kennicutt-Schmidt relation in Figure 4.10 provides an illustration of this point. If we study the lower panel of this figure, which features a direct comparison to NGC 5055, all of the galaxies that were able to regulate their star formation provide a convincing match. We know from our other diagnostics that they have different properties though: different star formation rates, different scale heights, different ISMs. This is a situation where we should be doing more careful comparisons of galaxies. Our galaxy is a passable proxy for NGC 5055 but there are differences in the profiles of both gas and stars, as well as the rotation curve. In order to address this better, we should use galaxies that are designed specifically to match observed galaxies. This will be a target of future work.

Bibliography

Agertz O., Kravtsov A. V., Leitner S. N., Gnedin N. Y., 2013, ApJ, 770, 25

Agertz O., Romeo A. B., Grisdale K., 2015, MNRAS, 449, 2156

Benincasa S. M., Tasker E. J., Pudritz R. E., Wadsley J., 2013, ApJ, 776, 23

Benincasa S. M., Wadsley J., Couchman H. M. P., Keller B. W., 2016, MNRAS, 462, 3053

Bigiel F., Leroy A., Walter F., Brinks E., de Blok W. J. G., Madore B., Thornley M. D., 2008, AJ, 136, 2846

Blitz L., Rosolowsky E., 2004, ApJ, 612, L29

Blitz L., Rosolowsky E., 2006, ApJ, 650, 933

Brinchmann J., Charlot S., White S. D. M., Tremonti C., Kauffmann G., Heckman T., Brinkmann J., 2004, MNRAS, 351, 1151

Colombo D., et al., 2014, ApJ, 784, 3

Consolmagno, G. and Schaefer, M., 1994, Worlds Apart: A Textbook in Planetary Sciences

Cox, D. P., 2005, ARA&A, 43, 337

Daddi, E. and Dickinson, M. and Morrison, G. and Chary, R. and Cimatti, A. and Elbaz, D. and Frayer, D. and Renzini, A. and Pope, A. and Alexander, D. M. and Bauer, F. E. and Giavalisco, M. and Huynh, M. and Kurk, J. and Mignoli, M., 2007, ApJ, 670, 156

Dobbs C. L., Pettitt A. R., Corbelli E., Pringle J. E., 2018, MNRAS, 478, 3793

Duarte-Cabral A., Dobbs C. L., 2017, MNRAS, 470, 4261

Elmegreen, B. G., 1997, Revista Mexicana de Astronomia y Astrofisica Conference Series, 6, 165

Elmegreen, B. G. and Parravano, A., 1994, ApJ, 435, L121

Field, G. B. and Goldsmith, D. W. and Habing, H. J., 1969, ApJ, 155, L149

Gallagher M. J., et al., 2018, ApJ, 858, 90

Grisdale K., Agertz O., Romeo A. B., Renaud F., Read J. I., 2017, MNRAS, 466, 1093

Grisdale K., Agertz O., Renaud F., Romeo A. B., 2018, MNRAS,

Hernquist L., 1990, ApJ, 356, 359

Herrera-Camus R., et al., 2017, ApJ, 835, 201

Hopkins P. F., Narayanan D., Murray N., 2013, MNRAS, 432, 2647

Hopkins P. F., Kereš D., Oñorbe J., Faucher-Giguère C.-A., Quataert E., Murray N., Bullock J. S., 2014, MNRAS, 445, 581

Hopkins P. F., et al., 2018a, MNRAS,

Hopkins P. F., et al., 2018b, MNRAS, 477, 1578

Hsieh B. C., et al., 2017, ApJ, 851, L24

Hu C.-Y., Naab T., Glover S. C. O., Walch S., Clark P. C., 2017, MNRAS, 471, 2151

Hughes A., et al., 2013, ApJ, 779, 46

Katz, N., 1992, ApJ, 391, 502

Keller, B. W. and Wadsley, J. and Couchman, H. M. P., 2016, MNRAS, 463, 1431

Keller, B. W. and Wadsley, J. and Couchman, H. M. P., 2015, MNRAS, 453, 3499

Keller B. W., Wadsley J., Benincasa S. M., Couchman H. M. P., 2014, MNRAS, 442, 3013

Kennicutt Jr. R. C., 1998, ApJ, 498, 541

Kennicutt R. C., Evans N. J., 2012, ARA&A, 50, 531

Kennicutt Jr. R. C., et al., 2007, ApJ, 671, 333

Kim C.-G., Ostriker E. C., 2015, ApJ, 815, 67

Kim C.-G., Ostriker E. C., Kim W.-T., 2013, ApJ, 776, 1

Kim, C.-G. and Kim, W.-T. and Ostriker, E. C., 2011, ApJ, 743, 25

Kim J.-h., et al., 2014, ApJS, 210, 14

Kim J.-h., et al., 2016, ApJ, 833, 202

Kritsuk, A. G. and Norman, M. L., 2002, ApJ, 569, L127

Krumholz M. R., Dekel A., McKee C. F., 2012, ApJ, 745, 69

Leitherer C., et al., 1999, ApJS, 123, 3

Leroy, A. K. and Walter, F. and Bigiel, F. and Usero, A. and Weiss, A. and Brinks, E. and de Blok, W. J. G. and Kennicutt, R. C. and Schuster, K.-F. and Kramer, C. and Wiesemeyer, H. W. and Roussel, H., 2009, ApJ, 137, 4670

Leroy A. K., Walter F., Brinks E., Bigiel F., de Blok W. J. G., Madore B., Thornley M. D., 2008, AJ, 136, 2782

Martin, C. L. and Kennicutt, Jr., R. C., 2001, ApJ, 555, 301

Martizzi D., Fielding D., Faucher-Giguère C.-A., Quataert E., 2016, MNRAS, 459, 2311

McNally C. P., Wadsley J., Couchman H. M. P., 2009, ApJ, 697, L162

Murphy E. J., et al., 2011, ApJ, 737, 67

Nakanishi H., Sofue Y., 2016, PASJ, 68, 5

Navarro J. F., Frenk C. S., White S. D. M., 1997, ApJ, 490, 493

Nguyen N. K., Pettitt A. R., Tasker E. J., Okamoto T., 2018, MNRAS, 475, 27

Noeske, K. G. and Weiner, B. J. and Faber, S. M. and Papovich, C. and Koo, D. C. and Somerville, R. S. and Bundy, K. and Conselice, C. J. and Newman, J. A. and Schiminovich, D. and Le Floc'h, E. and Coil, A. L. and Rieke, G. H. and Lotz, J. M. and Primack, J. R. and Barmby, P. and Cooper, M. C. and Davis, M. and Ellis, R. S. and Fazio, G. G. and Guhathakurta, P. and Huang, J. and Kassin,

S. A. and Martin, D. C. and Phillips, A. C. and Rich, R. M. and Small, T. A. and Willmer, C. N. A. and Wilson, G., 2007, ApJ, 660, L43

Ostriker E. C., Shetty R., 2011, ApJ, 731, 41

Ostriker E. C., McKee C. F., Leroy A. K., 2010, ApJ, 721, 975

Pan H.-A., Fujimoto Y., Tasker E. J., Rosolowsky E., Colombo D., Benincasa S. M., Wadsley J., 2015, MNRAS, 453, 3082

Rey-Raposo R., Dobbs C., Agertz O., Alig C., 2017, MNRAS, 464, 3536

Roman-Duval J., Jackson J. M., Heyer M., Rathborne J., Simon R., 2010, ApJ, 723, 492

Saintonge A., et al., 2017, ApJS, 233, 22

Salim, D. M. and Federrath, C. and Kewley, L. J., 2015, ApJ, 806, L36

Salim S., et al., 2007, ApJS, 173, 267

Schaye J., 2004, ApJ, 609, 667

Semenov V. A., Kravtsov A. V., Gnedin N. Y., 2016, ApJ, 826, 200

Semenov V. A., Kravtsov A. V., Gnedin N. Y., 2017, ApJ, 845, 133

Semenov V. A., Kravtsov A. V., Gnedin N. Y., 2018, ApJ, 861, 4

Shetty, R. and Ostriker, E. C., 2012, ApJ, 754, 2

Shi, Y. and Yan, L. and Armus, L. and Gu, Q. and Helou, G. and Qiu, K. and Gwyn, S. and Stierwalt, S. and Fang, M. and Chen, Y. and Zhou, L. and Wu, J. and Zheng, X. and Zhang, Z.-Y. and Gao, Y. and Wang, J., 2018, ApJ, 853, 149

Silk, J., 1997, ApJ, 481, 703

Springel V., Hernquist L., 2003, MNRAS, 339, 289

Sun J., et al., 2018, ApJ, 860, 172

Tasker E. J., Tan J. C., 2009, ApJ, 700, 358

Tielens A. G. G. M., 2005, The Physics and Chemistry of the Interstellar Medium

Wadsley J. W., Stadel J., Quinn T., 2004, New A, 9, 137

Wadsley J. W., Keller B. W., Quinn T. R., 2017, MNRAS, 471, 2357

Walch S., et al., 2015, MNRAS, 454, 238

Ward R. L., Benincasa S. M., Wadsley J., Sills A., Couchman H. M. P., 2016, MNRAS, 455, 920

Wolfire M. G., McKee C. F., Hollenbach D., Tielens A. G. G. M., 2003, ApJ, 587, 278

Wolfire, M. G. and Hollenbach, D. and McKee, C. F. and Tielens, A. G. G. M. and Bakes, E. L. O., 1995, ApJ, 443, 152

Wong T., Blitz L., 2002, ApJ, 569, 157

Woods R., 2015, PhD thesis, McMaster University

Chapter 5

Summary & Future Work

The common thread throughout the three preceding chapters has been a focus on star formation that includes the galactic context. The common goal throughout was to undertake a more quantitative study of star formation in isolated galaxy simulations than typically seen in the literature. Further, we have tried to bring in key physics and physical considerations that have been lacking in prior work. As discussed in the introduction, there is a drive to simulate and understand galaxies ab initio. However, we are not at a point where the results are reliable analogues of present-day disk galaxies in most respects. Instead, we have tried to make targeted strides in understanding the nature of galaxies as we see them today, without following galaxy formation from beginning to end.

Generally, there is a list of deeper questions that have shaped the work in this thesis. This work began with the question of what sets the star formation rate, not in individual molecular clouds but across the galactic disk. Since we must make parameter choices this manifested itself as a question of what consequences this has in simulations. We attempted to understand the key processes in terms of where numerical parameters and sub-grid choices matter and where they do not. For example, when you look on larger scales different considerations begin to dominate, such as hydrostatic balance of the galaxy disk rather than the properties of any one molecular cloud. As we continued forward in this study, additional questions presented themselves. For instance, what are the expectations for structures in disks and do we really understand their theoretical origins? Further, are we using the best methods to attack certain problems, or are we relying on common approaches in circumstances where they do not illuminate the problem? For example, ab initio simulations are more expensive and thus limit resolution. This may prevent us from gaining key insights. A specific example is our inability to understand the role of the galactic scale height in regulating star formation if we do not resolve it.

Our chosen method in this thesis has been to consider these problems through the lens of isolated galaxy simulations. Even though the CMB has given us very detailed information about the initial conditions in the Universe, our ability as simulators to take those initial conditions and create convincing analogues of disk galaxies today is still quite limited. On the other hand, observations of disk galaxies are superb and only getting better. Isolated galaxies are under-utilized in this sense as they are less expensive than cosmological zooms and can be tailored to match present galaxies better. In addition, they provide a controlled experimental environment to explore the roles of different physical processes and assumptions.

In Chapter 2 we explored what controls the star formation rate in galaxies. We extended this question to include an exploration of the connection between sub-grid star formation and feedback parameters, and the resulting star formation rates in galaxy simulations. It is has previously been documented that the scaling between star formation or feedback parameters and the star formation rate is sub-linear (e.g. Agertz & Kravtsov, 2015; Hopkins et al., 2011). What was not known, was the physics driving this behaviour.

The galactic pressure is known to play a large role in setting the star formation rate (Ostriker et al., 2010). In Chapter 2 we were able to confirm the role of pressure equilibrium in setting the star formation rate. A main goal of Chapter 2 was to identify which aspects of the smaller scale physics of star formation impact the larger scales in galaxy simulations. We identified the pressure as the quantity driving these parameter relations. Specifically, it is the scale height in the galaxy that causes this sub-linear coupling between parameters and the star formation rate as it rapidly adjusts to changes in feedback. This has important implications for simulators. If the goal of a simulation is to study the regulation of star formation, then resolving vertical structure is critical.

An additional outcome is that roughly matching star formation rates alone does not imply other aspects of a simulated galaxy are correct. A given rate can be achieved in multiple ways with different numerical choices and different physical outcomes, such as the properties of the ISM. This last point would be explored further in Chapter 4.

In Chapter 3 we developed a new approach to studying the formation of star clusters and other baryonic condensations in disk galaxies. There exists a persistent dichotomy in the measured masses of stellar clumps, both in simulations and observations, in the current literature. In simulations, this manifests itself as a debate over the formation masses of high-redshift star clusters. Previously both isolated and cosmological galaxy simulations, with different methods for star formation and feedback, have been used to study this problem. Rather than continue to attempt a similar approach, we have developed a new method to study the formation of these bound objects. We avoid having to choose a feedback method by seeding turbulent clump formation events ourselves and evolving them in quiet isothermal disks at high resolution. The high resolution is important to forestall criticisms such as failing to resolve important scales such as the Jeans' length or unstable disk wavelengths.

We were able to compare these clump masses to observational results and find that, particularly in lower mass galaxies, beam crowding may explain the high clump masses observed. This has previously been suggested by other studies (e.g. Tamburello et al., 2017). When comparing to the Toomre mass, a popular approach, we find that our masses are lower. This suggests that the Toomre mass should be treated as an absolute maximum, rather than typical mass. This study has shown that we have not previously had a complete framework to describe bound structure formation. Previously, as a community, we have relied on linear stability theory that is strictly only appropriate for thin disks and for tightly wound (local) or axisymmetric perturbations. Observations clearly demonstrate that high redshift galaxies, in particular, are gas rich, highly unstable and far from axisymmetric.

In Chapter 4, we continued our exploration of the regulation of star formation from Chapter 2. However, in this case we were able to add new physics to our simulations: radiative transfer. In this chapter we used radiative transfer to model FUV heating in a way that is self-consistent with recent star formation. This was strongly motivated by a claim from Ostriker et al. (2010) that FUV could regulate star formation in local disk galaxies without a direct role for supernovae feedback. This is the first study of its kind on the full galactic scale; other similar studies employ a background FUV heating term (e.g. Kim et al., 2013; Benincasa et al., 2016; Hu et al., 2017). Additionally, these galaxies included a live old stellar population and dark matter halo, in contrast to the simulations in Chapter 2 which were done in a static potential. We find that the presence of a heavy stellar disk makes our pressure equilibrium argument even stronger; this was a key part of the argument of Ostriker et al. (2010). When gas is not driving the dynamics of the disk, pressure equilibrium is more static. This removed the need to consider the time-averaged state of the disk.

However, contrary to Ostriker et al. (2010), we have found that FUV heating in and of itself is not sufficient to regulate star formation in the galaxies we test. The Ostriker et al. (2010) model is incomplete as it does not contain a self-consistent treatment for turbulence. We find that, in combination with superbubble feedback, FUV heating changes the state of the ISM. When FUV is combined with a decreased superbubble energy, we are able to regulate star formation without destroying spiral structure. Generally, strong supernovae feedback can struggle to maintain this type of structure. This result is intriguing for what it implies for feedback. Over the past 10 years, cosmological galaxy simulators have been advocating for extremely strong feedback without considering its impact on the ISM. These conflicting requirements should allow us to tightly constrain the forms of feedback that can be consistent with the observed ISM in galaxies as well as the SMHM relation over cosmic time. We find that a key function of the FUV heating is to move gas from the cold diffuse phase and into the warm diffuse phase.

A key theme in all of this work is that we have favoured the use of purposefully simple set-ups. This has been done to gain an understanding of star formation and the physics in the ISM without the complication of the interaction of complex feedback recipes. We have also kept the physics simple, to avoid ambiguities as to the origins of our results. In many respects, we have been successful in this goal. We have shown that the link between pressure and star formation carries through into numerical simulations, and that these simulations are in dynamic pressure balance. We have been able to constrain the mass spectrum of bound star-forming regions, in a way that has not been done before. A key result to take away is that this has been done without the cosmological context. Our simulations were comparatively inexpensive and fast and yet we were able to gain good insight on star formation. It is not clear if spending similar amounts of computer effort on zoom-ins would give similar insight.

5.1 Future Work

This thesis has attempted, and hopefully succeeded, in making strides in understanding star formation in the galactic context. Considering the work in the previous chapters, there are a few specific fruitful directions that emerge:

- What is the cause of the intrinsic scatter in the Kennicutt-Schmidt relation?
- What is the full role of pressure in galaxies? Can it be better tied to properties beyond the star formation rate?
- Are there any physics we are missing in our simulations that could play a key role or hinder comparison to observations?
- Are we doing a good enough job modelling galaxies in detail?

In the following section we detail a few of these avenues that would be good for future work.

The inclusion of radiative transfer in our simulations is a huge step forward. Not only does radiative transfer enable the use of self-consistent FUV heating, it offers the opportunity to perform better synthetic observations. Including more chemistry networks in simulations allows for the formation of molecules that are used as observational tracers. With radiative transfer and this additional chemistry, we could track the formation of molecular hydrogen and even CO. Implementing this additional chemistry is an interesting next step. With the radiative transfer, we can then generate mock observations tailored to specific wavebands and instruments.

Magnetic fields are potentially important to star formation (e.g. Körtgen et al., 2018). They have been shown to play a role in the formation and maintenance of spiral arms, and the formation of spurs on these arms (e.g. Kim & Ostriker, 2006; Dobbs et al., 2016). However, magnetic fields have been notoriously difficult to implement into SPH codes, until recently (Tricco & Price, 2013). Magnetohydrodynamics are currently being implemented in GASOLINE. This provides us with a new avenue to study star formation in spiral arms and spurs, as there is still no consistent picture describing how star formation is triggered here (e.g. Schinnerer et al., 2017)

In general, our work has shown that there is an important place for isolated galaxy simulations in studies of star formation and the ISM. So much focus is put on cosmological zoom-ins, as they offer the cosmological context. However, one could argue, that in terms of star formation they cannot give us the type of detailed information that we need. Our work has shown that resolving the vertical structure is key to studying star formation. Further, isolated galaxies can be used to do targeted studies of galaxies. Thus, we can use them to model specific galaxies and provide a targeted comparison to observations. This is something that cannot be done with cosmological zoom-ins, but is something that we need to make progress. Exploring the Kennicutt-Schmidt relation requires these targeted studies.

Chapter 4 shows us what open questions remain. This is particularly illustrated by the Kennicutt-Schmidt relation. Of the galaxies in Chapter 4 that show regulated star formation, all of these agree with the Kennicutt-Schmidt relation for the sunflower galaxy; they are just slightly offset from each other. However, our match to the sunflower galaxy is not perfect to begin with. How then are we to execute a truly meaningful comparison? It is in situations like this where we often find ourselves, in isolated galaxies but especially in cosmological zoom-ins. In cases like this, it is easy to convince yourself that the right answer is the one that is most convenient. Studies like this are particularly timely as large high resolutions surveys like PHANGS become available.

An obvious direction for future work then, is to make a more detailed attempt at modelling specific galaxies. This will allow us to make more direct connections with large surveys like THINGS and HERACLES. It is in galaxies like this where we stand a chance at discovering the additional parameters controlling the Kennicutt-Schmidt relation. If we are able to do this in simple isolated systems, we can then be confident that we can correctly extend to more complicated environments. This could be extended to more puzzling isolated systems, like M74, or complex interacting systems.

Further, this study could be extended to dwarf galaxies. These low surface brightness systems provide us with an interesting opportunity to study the faint end of the Kennicutt-Schmidt relation. These systems could give us more insight into the processes that truncate star formation. As discussed in previous sections, the truncation of star formation in the outer, low surface density edges of galaxies remains poorly understood. These environments provide a good place to study systems that are HI dominated, but still have star formation.

In two of the chapters in this thesis we have explored the role of pressure in star formation. However, we would ideally like to better understand the role of pressure in not just star formation but in setting quantities like the star formation efficiency. As observations are getting better and better, the role of pressure has been of great interest in ISM studies (e.g. Herrera-Camus et al., 2017; Gallagher et al., 2018). Isolated galaxies provide the perfect place to study this role, and this should be possible in the simulation setups we already have. For instance, there is a relation between the gas velocity dispersion and the depletion time or star formation rate in the ISM (e.g. Krumholz et al., 2018, and references therein). This relation cannot be explained by current models targeting the regulation of star formation.

The star formation rate is set at a certain level because a galaxy strives to maintain vertical hydrostatic balance. If we look on sub-kpc scales in our simulations, we can find regions that are out of balance. These regions can be identified as either just leaving or just approaching equilibrium. This departure or approach should manifest itself as a change in the scale height, which carries with it a velocity signature. This line of sight velocity is a directly comparable observable, which means we can provide insight for observational studies of galaxies. This can be tied to the depletion time in these regions, and thus, be directly compared to the relation described above. It may be that the different tracks seen in this relation correspond to galaxies either departing from or approaching hydrostatic balance.

Generally, a good way forward for most of these ideas is to push for closer collaboration between simulators and observers. There has been work showing that there is a timing offset between different observables: star formation tracers track different evolutionary phases from gas tracers (Kruijssen et al., 2014, 2018). This becomes a problem as the spatial scales of extragalactic observations decrease, and there is less averaging in a single beam. This is an excellent place for simulators to partner with observers and do targeted studies of galaxies. Simulations may be able to reveal observational signatures to help clarify this uncertainty.

Our work in Chapter 3 has also been developed with such a partnership in mind. All that our method requires is knowledge of the rotation speed and gas surface density of a galaxy. If this data is provided, we can estimate the initial clump masses in specific galaxies. Setups like this could be particularly fruitful for comparing to high resolution studies, like HST-DYNAMO (Fisher et al., 2017).

Bibliography

Agertz O., Kravtsov A. V., 2015, ApJ, 804, 18

Benincasa S. M., Wadsley J., Couchman H. M. P., Keller B. W., 2016, MNRAS, 462, 3053

Dobbs, C. L. and Price, D. J. and Pettitt, A. R. and Bate, M. R. and Tricco, T. S., 2016, MNRAS, 461, 4482

Fisher, D. B. and Glazebrook, K. and Damjanov, I. and Abraham, R. G. and Obreschkow, D. and Wisnioski, E. and Bassett, R. and Green, A. and McGregor, P., 2017, MNRAS, 464, 491

Gallagher M. J., et al., 2018, ApJ, 858, 90

Herrera-Camus R., et al., 2017, ApJ, 835, 201

Hopkins, P. F. and Quataert, E. and Murray, N., 2011, MNRAS, 417, 950

Hu C.-Y., Naab T., Glover S. C. O., Walch S., Clark P. C., 2017, MNRAS, 471, 2151

Kim C.-G., Ostriker E. C., Kim W.-T., 2013, ApJ, 776, 1

Kim, W.-T. and Ostriker, E. C., 2006, ApJ, 646, 213

Körtgen, B. and Banerjee, R. and Pudritz, R. E. and Schmidt, W., 2018, MNRAS, 479, L40

Kruijssen, J. M. D. and Schruba, A. and Hygate, A. P. S. and Hu, C.-Y. and Haydon, D. T. and Longmore, S. N., 2018, MNRAS, 479, 1866

Kruijssen, J. M. D. and Longmore, S. N., 2014, MNRAS, 439, 3239

Krumholz, M. R. and Burkhart, B. and Forbes, J. C. and Crocker, R. M., 2018, MNRAS, 477, 2716

Ostriker E. C., McKee C. F., Leroy A. K., 2010, ApJ, 721, 975

Tamburello V., Rahmati A., Mayer L., Cava A., Dessauges-Zavadsky M., Schaerer D., 2017, MNRAS

Tricco, T. S. and Price, D. J., 2013, MNRAS, 436, 2810

Schinnerer, E. and Meidt, S. E. and Colombo, D. and Chandar, R. and Dobbs, C. L. and García-Burillo, S. and Hughes, A. and Leroy, A. K. and Pety, J. and Querejeta, M. and Kramer, C. and Schuster, K. F., 2017, ApJ, 836, 62